UNIVERSITY OF CALIFORNIA, SAN DIEGO

TUNING SURFACE CHEMISTRY AND NANOSTRUCTURE IN POROUS SILICON FOR MOLECULAR SEPARATION, DETECTION, AND DELIVERY

A dissertation submitted in partial satisfaction of the requirements for the degree Doctor of Philosophy

in

Materials Science and Engineering

by

Chia-Chen Wu

Committee in charge:

Professor Michael J. Sailor, Chair
Professor Raffi V. Aroian
Professor Donald J. Sirbuly
Professor Andrea R. Tao
Professor Liangfang Zhang

2013

The dissertation of Chia-Chen Wu is approved, and it is acceptable in quality and form for publication on microfilm and electronically:

Chair

University of California, San Diego

2013

DEDICATION

To my family

TABLE OF CONTENTS

LIST OF FIGURES

LIST OF TABLES

ACKNOWLEDGEMENTS

First I'd like to express my sincere gratitude to Professor Sailor, you are my number one role model as a passionate scientist and an enthusiastic educator. Thank you for all the guidance, patience, encouragement (good girl!) and support throughout my thesis study.

Thanks to my committee members who offered their precious time and advices for my thesis: Prof. Raffi Aroian, Prof. Andrea Tao, Prof. Liangfang Zhang, and Prof. Donald Sirbuly.

Thanks to all members of the Sailor group for all the helpful discussions and more importantly the moral support. It was great to work with people like you and I enjoyed pep talks with you guys: Sara, Michelle, Liz, Jen, Ji-Ho, Shawn, Emily, Anne, Adrian, Danny, Joel, Kat, Maggie, Zhangtao, Jayoung, Heidi, Shalini, Kim, Andrea, Jessica, Vinh, Rhiannon, Vivian, Serena, and Alyssa. Special thanks to Sara, my mentor to help me started in Sailor lab from the very beginning. And Michelle, my coffee carts buddy and teammate of stinky tofu, for all the random talks that entertained me and kept me sane by playing the counter part ☺

To the awesome postdocs in the lab, Dr. Jennifer Andrew, Dr. Matt Kinsella, Dr. Timothy Kelly, Dr. Wei Jin, Dr. Alejandra Nieto-Pena, Dr. Nicole Fry, Dr. Emily Anglin, and Dr. Jinmyoung Joo, thank you for the valuable suggestions and secret tips to survive grad schools.

I'm fortunate to collaborate with knowledgeable scientists in other fields of study. Prof. Lin Chao, Dr. Camilla Rang, Prof. Raffi Aroian, Dr. Yan Hu, Melanie

Miller for filling me in biology information and how to handle bacteria and worms. Dr. Jay Snyder and James Ha for showing me engineering concepts.

It was pleasure to meet up and collaborate with international scholars: Prof. Gordon Miskelly for inspiring discussions, Dr. Frédérique Cunin for offering research experience in France, and Dr, Nobuhiro Yagi for home style miso soup. And all other visiting students who show me cross-culture experiences: Emilie, Stéphanie, Beniamino, Kyu Shik, Michela, Linda, Matrix, and FengXia.

To my gang of Taiwanese friends, Pai, Mengchun, Yen-Wei, Wen-Hsuan, Yu and all others, thank you for being there whenever I need you and share worries of uncertainty towards life but still fight hard. I am very lucky to know each of you and ready for pep talk any time I dialed.

To my family—thank you for the constant support from the very beginning before I even stepped out of Taiwan. Those daily international calls started with "good morning, good afternoon and good night" throughout past 6 years have been the strongest support to my journey abroad. Last but not least, I would like to thank Weng for his support and understanding my pursuit of dreams.

Chapters two, three, four, and appendix A and B are, in part or in full, reprints of the following publications:

- **Wu, C.**; Chen, M. Y.; Sailor, M. J. "Differential Adsorption of Small Molecules in Spatially Functionalized Porous Silicon Nanostructures", *Langmuir*, 2013, DOI: 10.1021/la402261v

- **Wu, C.**; Sailor, M. J. "Selective Functionalization of the Internal and the External Surfaces of Mesoporous Silicon by Liquid Masking", *ACS Nano,* 2013, 7, 3158-3167

- **Wu, C.**; Hu, Y.; Miller, M.; Aroian, R.; Sailor, M. J. "Interaction of Porous Si Particles with Biological Surfaces of Nematodes" *Manuscript in preparation*

- **Wu, C.**; Alvarez, S.; Rang, C.; Chao, L; Sailor, M. J. "Label-free Optical Detection of Bacteria on a 1-D Photonic Crystal of Porous Silicon", *Proceeding of the SPIE*, 2009, 71670Z

- **Wu, C.**; Chan, D. Y.; Snyder, J. L.; Sailor, M. J. "Carbon/Silicon Composites Rugate Filter-based Sensor as an End-of-service life Indicator" *Manuscript in preparation*

The author of this dissertation was one of the primary authors or co-author on all publications.

VITA

EDUCATION

2013	Ph.D., Materials Science and Engineering, University of California, San Diego
2008	M.S., Materials Science and Engineering, University of California, San Diego
2007	B.S., Materials Science and Engineering, National Tsing-Hua University (R.O.C.)

PUBLICATIONS

Wu, C.; Chan, D. Y.; Snyder, J. L.; Sailor, M. J. "Carbon/Silicon Composites Rugate Filter-based Sensor as an End-of-service life Indicator" *Manuscript in preparation*

Wu, C.; Hu, Y.; Miller, M.; Aroian, R.; Sailor, M. J. "Interaction of Porous Si Particles with Biological Surfaces of Nematodes" *Manuscript in preparation*

Chen, M. Y.; Diep, V.; **Wu, C.**; Secret, E.; Cunin, F.; Andrew, J.; Sailor, M. J. "Multistage Insulin Release using Double-Layer Mesoporous Silica Structures" *Manuscript in preparation*

Chan, D. Y.; Garcia Sega, A.; **Wu, C.**; Sailor, M. J. "Palladium/porous silica Composite Films for the Detection of Hydrogen Gas" *Manuscript in preparation*

Wu, C.; Chen, M. Y.; Sailor, M. J. "Differential Adsorption of Small Molecules in Spatially Functionalized Porous Silicon Nanostructures", *Langmuir*, 2013, DOI: 10.1021/la402261v

Wu, C.; Sailor, M. J. "Selective Functionalization of the Internal and the External Surfaces of Mesoporous Silicon by Liquid Masking", *ACS Nano,* 2013, 7, 3158-3167

Churaman, W. A.; Becker, C. R.; Morris, C. J.; Currano, L. J; **Wu, C.**; Sailor, M. J. "Packaging Nanoporous Energetic Silicon for On-chip MEMS Applications", *IWLPC (Wafer-Level Packaging) Conference Proceedings,* 10/03/2011

Wu, C.; Alvarez, S.; Rang, C.; Chao, L; Sailor, M. J. "Label-free Optical Detection of Bacteria on a 1-D Photonic Crystal of Porous Silicon", *Proceeding of the SPIE*, 2009, 71670Z

ABSTRACT OF THE DISSERTATION

TUNING SURFACE CHEMISTRY AND NANOSTRUCTURE IN POROUS SILICON FOR MOLECULAR SEPARATION, SENSING, AND DELIVERY

by

Chia-Chen Wu

Doctor of Philosophy in Materials Science and Engineering
University of California, San Diego, 2013

Professor Michael J. Sailor, Chair

Mesoporous materials with engineered surface properties are of interest for molecular separations, catalysis, drug delivery, and chemical sensing. One of the longstanding chemical challenges in the engineering of nanomaterials is to control the placement of different chemistries in spatially distinct regions on a nanoscale object. This thesis focuses on discovering and understanding processes to prepare such spatially differentiated chemistries on porous silicon. For the porous silicon system, the ability to prepare pores of average diameter anywhere from 1 to 200 nm allows the harnessing of surface tension and capillary forces to promote or obstruct the infiltration of reagent for selective modification.

The first process investigated involves placing different chemistries on the pore walls by means of microdroplet patterning. In this method, a chemical resist is drop-coated on a porous silicon sample to mask distinct regions across the plane of the chip for subsequent chemical modification. Two chemistries, silicon oxide and silicon-methyl, are demonstrated here. The differential partitioning of test molecules on the resulting hydrophilic/hydrophobic film is achieved by simultaneous optical reflectance measurement of both regions, where the reflectance spectrum contains a convolution of the Fabry-Pérot interference spectrum for both types of surface chemistries.

A second approach to engineer porous Si nanostructures that is investigated uses a hydrophobic organic liquid as a chemical resist; it is infiltrated into the pores to mask the interior of the porous silicon film, while the exterior surface and the pore mouths of the film are subjected to an aqueous chemical reaction with HF and subsequent chemical modification by thermal hydrosilylation. When chemically modified with a hydrophobic dodecyl species, the resulting film has a hydrophilic interior and a hydrophobic outer surface. The ability of these core-shell porous nanostructures to admit and release small molecules is assessed and exploited.

The last portion of the thesis focuses on an evaluation of chemically modified porous silicon particles as oral drug delivery material, with an emphasis on the ability of the interior of the porous silicon nanostructure to protect physiologically unstable drugs. Partially oxidized porous silicon particles show no toxicity to nematodes at particle concentration up to 1 mg/mL in culture media. *In vitro* experiments show the particles protect anthelmintic protein-based drug Cry5B from hydrolytic degradation in simulated gastric fluid, and the bioactivity against nematodes is maintained. However,

much reduced bioactivity of the therapeutic particles is observed *in vivo* on hookworm-infected hamsters. The lack of effectiveness in treating the disease *in vivo* is attributed to the short residence time of the particles in the gut of the animals.

CHAPTER ONE

INTRODUCTION TO SURFACE MODIFICATION IN POROUS SILICON FOR ANALYTICAL AND BIOMEDICAL APPLICATIONS

1.1 Introduction and Motivation

Porous silicon (porous Si) was first discovered in the mid 1950s by Arthur Uhlir at Bell Laboratories while attempting to electrochemically machine silicon wafers for microelectronic circuits fabrication.[1] Porous Si did not gain much interest until its photoluminescence was observed in the 1990s.[2, 3] Since then, extensive efforts have been put to understand the mechanism of pore formation, chemical functionalities, and optical properties with this material. Many chemical and biological applications have been reported using porous Si-based platforms including detection of volatile organic compounds (VOCs),[4, 5] toxins,[6] explosives,[7] proteins,[8] oligonucleotides,[9], enzyme activity[10] and drug delivery.[11, 12]

Porous Si, prepared from the electrochemical etching of single crystals of n− or p−type silicon, is a versatile material with high surface area (around several hundreds m^2/cm^3),[13] tunable pore dimensions,[14] ease of surface chemistry functionalization,[15] and unique optical properties[16] that has been attributed to applications such as separation, sensing, and drug delivery. Surface modification on porous Si plays two pivotal roles to potential applications: (1) to passive surface for stability and to achieve zero baseline drift in chemical sensing within appropriate time scale; (2) to incorporate chemical/biochemical functionalities at the interfaces and exercise molecular−surface interactions for selective and enhanced binding efficiency between target molecules and the surface.

Recent advances in the design of porous Si-based interferometric biosensors and desorption ionization mass spectroscopy developed with porous Si have highlighted the

need for selective surface modification that can meet the needs of a given application.[17, 18] Particular interests include the patterning of surface chemistries, control of spatially resolved chemistry distribution to enable molecular separation and differentiation within porous materials will be reviewed. Secondly, common methods for chemical characterization on materials surfaces will also be addressed. These analyses are essential for verifying the success of intended surface modification strategies and for reliable interpretation of molecular−surface interactions.

1.2 Preparation of Porous Silicon

Porous Si can be prepared from electrochemical etching of crystalline Si wafers in aqueous hydrofluoric acid (HF) solution under a two-electrode configuration.[19] A schematic of a two-electrode cell for etching silicon, with relevant half-reactions, is shown in Figure 1.1. In the case of porous Si formation, the silicon electrode is the anode in which being oxidized and usually is referred as the "working electrode." In the presence of fluoride ions, oxidized Si is removed from the surface as either SiF_4 or SiF_6^{2-} (Figure 1.2). The cathode used in the etching cell is platinum, referred to as the counter-electrode, in which the reduction of protons to H_2 occurs.

Electrochemical reactions in the silicon system containing HF can be represented by four-electron and two-electron processes (Equation 1.1 and 1.2, respectively):

$$Si + 4h^+ + 6F^- \rightarrow SiF_6^{2-} \qquad (1.1)$$

$$Si + 2h^+ + 2H^- + 6F^- \rightarrow SiF_6^{2-} + H_2 \qquad (1.2)$$

The four-electron electrochemical oxidation of silicon represented by Equation 1.1 is

the predominant reaction when the fluoride ions are unable to reach the surface to remove the Si, referred to as electropolishing, and no porous Si formed. The two-electron process represented by Equation 1.2 predominates at lower applied potential and is the main half-reaction responsible for porous Si formation. In the electrolysis of water, hydrogen gas is observed to form at the cathode (platinum wire in this case).

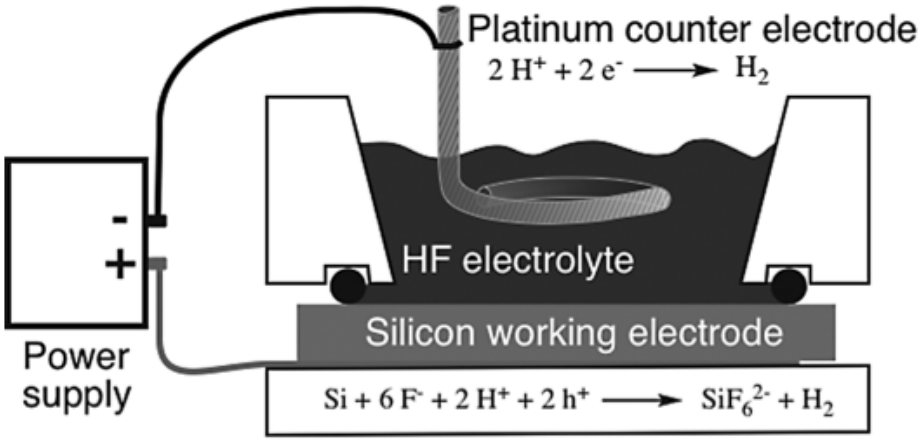

Figure 1.1 Schematic of a two-electrode electrochemical cell used to make porous Si. Silicon is the working electrode. The working electrode is an anode in this case, because the oxidation reaction occurs at its surface. The cathode counter-electrode is typically platinum. The main oxidation and reduction half-reactions occurring during the formation of porous Si are given. (Reprint from reference[19])

(a)

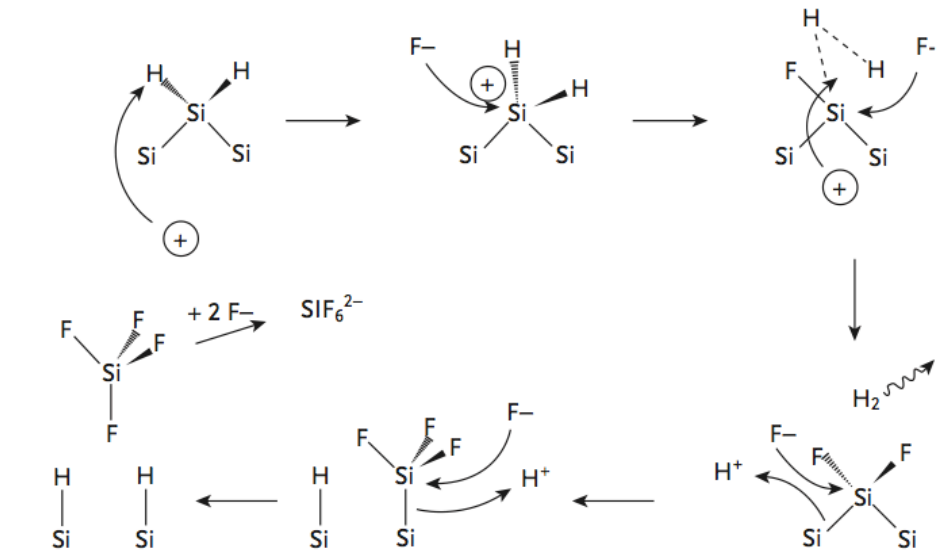

(b)

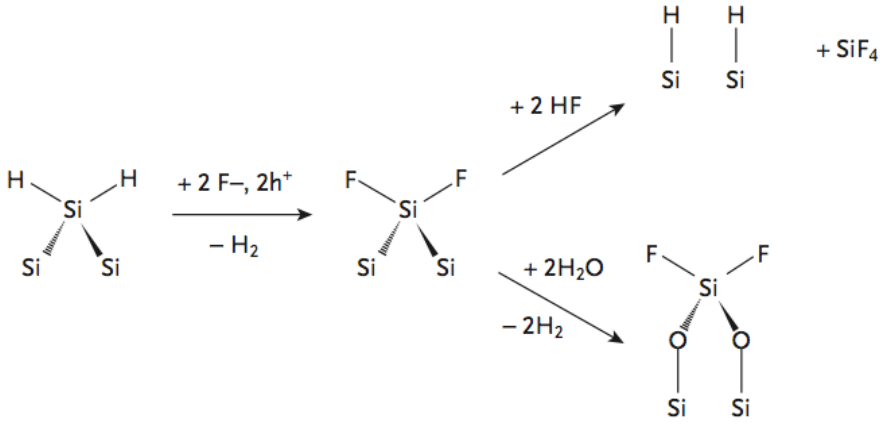

Figure 1.2 Mechanism of electrochemical dissolution reactions. (a) Simplified mechanism for electrochemical etching of silicon in fluoride-containing solution. (b) The effect of fluoride concentration: the upper branch depicts oxidation of silicon when excess HF is present and the lower branch indicates water attacks as insufficient HF supplied, resulting in an formation of insulating oxide. (Adapted from reference[3, 14])

1.2.1 Tunable Pore Dimension

The International Union of Pure and Applied Chemistry (IUPAC) has classified pores according to their diameters (d):[20]

(i) pores with diameters exceeding 50 nm are called *macropores* ($d > 50$ nm);

(ii) pores with diameters below 2 nm are called *micropores* ($d < 2$ nm);

(iii) pores of intermediate diameters are called *mesopores* ($2 \text{ nm} < d < 50 \text{ nm}$)

Pore size and porosity generated from electrochemical etching in Si wafers can be controlled by the electrolyte solution concentration, applied current density, n− or p−type wafer, and dopant levels. Pore size controlled by current density is a convenient approach to fabricate desired nanostructure with flexible control in x−y plane[21, 22] and in the z−direction[23] of the Si wafer. Figure 1.3 shows the porous Si morphology prepared from the anodic etching. Generally, small pores are favorable for detection of gas molecules where capillary condensation can be utilize to enhance the sensibility while large pores are favorable when adsorption of biomolecules such as protein is intended.

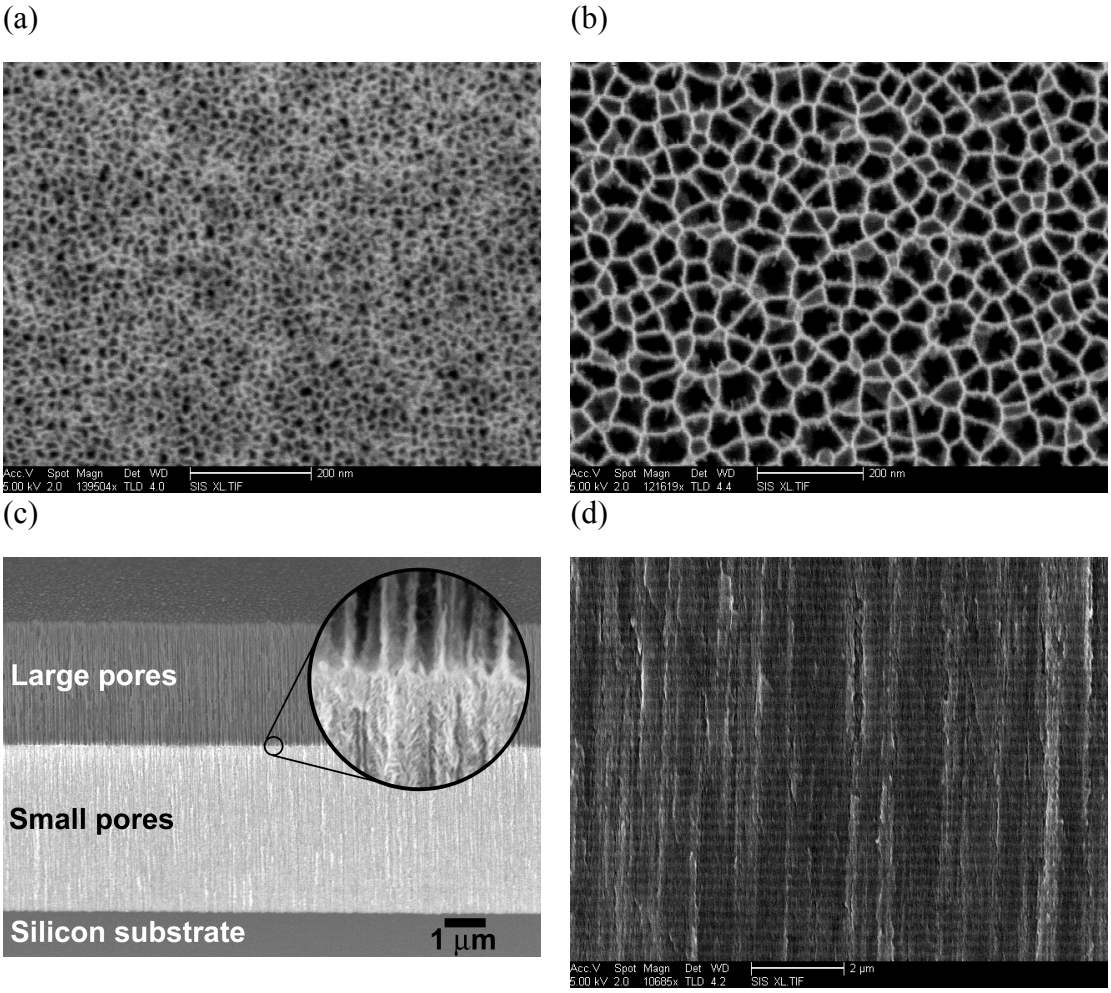

Figure 1.3 Scanning electron micrograph of porous Si thin films. (a) Top view micrograph of porous Si etched in 3:1 HF:ethanol etchant solution with current density of 75 mA/cm^2. (b) Top view image of porous Si etched in 1:1 HF:ethanol electrolyte with the same current density and similar wafer resistivity in (a). (c) Cross-section of porous Si thin film containing a built-in size exclusion with large pores fabricated on top of a small pores by changing the current density. (d) Cross-section image etched with sinusoidally modulated current density. (image (c) reprints from reference[24])

1.2.2 Optical Properties

Various structures can be electrochemically machined into silicon wafers, resulting in various structures including Fabry-Pérot layers,[8] multilayers,[25] rugate filters,[26] and microcavities.[27] Unique optical spectra arise from the physical properties of the porous layer. Porous Si behaves as a dielectric material with an effective refractive index, *n*, that is directly dependent on its porosity and chemical composition. Change of averaged refractive index associated with change of chemical composition or infiltration of molecules results in the change of optical spectrum. Monitoring such changes in optical spectrum provides an effective and nondestructive means for materials characterization and sensing applications.

Fabry-Pérot interference fringes corresponding to constructive and destructive interference from light reflected at the air/porous Si and porous Si/crystalline Si interfaces. The peak maximum for each of the spectral fringes follows the Fabry-Pérot interference relationship represented by Equation 1.3 in normal incidence:

$$m\lambda = 2nL \qquad (1.3)$$

where *m* is the spectral order of the fringes at wavelength λ, *n* is the average refractive index of the porous layer and the its contents, and *L* is the physical thickness of the film. Reflective interferometric Fourier transform spectroscopy (RIFTS)[28] applies the fast Fourier transform (FFT) to the reflective spectrum, yielding a 2*nL* (from Equation 1.3) values that is commonly referred as effective optical thickness in a particular porous Si sensor. Molecular or solvent infiltration can be easily tracked by monitoring the optical

spectrum change, resulting in the change of average refractive index as infiltration event occurs.

Porous Si rugate filters are generated by applying a sinusoidal varying current density during the etching procedure. The resulting layer possesses varying porosity, as well as refractive index, in the direction that is perpendicular to the plane of the filter. Light reflected from the rugate filter allows only specific wavelengths to pass through the structure and therefore displays a reflectivity peak in optical spectrum. Porous Si rugate filters behave as 1-D photonic crystal with tunable peak position have been widely used for sensing of various chemical agents and biomolecules.[6, 29] Appendix A and B of this dissertation will demonstrate use of this optical property for sensing applications.

1.3 Surface Chemistry in Porous Silicon

The native surface of freshly etched porous Si is hydride-terminated. However, the hydride-terminated surface is thermodynamically unstable due to its propensity to oxidize in air and water, limiting its usage for the long-term sensing application. Routes to passivate the surface for higher stability generally fall into two classes: one is to link a reagent to the Si surface via Si−O bonds; the other one is to use Si−C bonds.

1.3.1 Formation of Si−O bonds

Formation of silicon oxide (SiO_2) species is commonly used to stabilize the silicon surface.[15] Surface oxide has served admirably well as the main electronic

passivation route for silicon-based devices since 1960s due to its stability and ease of synthesis. However, its insulating property may be a problem if direct electronic connection is required. Thermal oxidation in an oxygen atmosphere at high temperature generates very stable surface.[30] A thin oxide layer can be formed on the surface with mild temperature while complete oxidation can be achieved at higher temperature (typically > 750 °C). Oxidation reagents such as dimethyl sulfoxide (DMSO) have also been proposed to oxidize hydride-terminated surfaces.[31] The oxidative treatment of porous Si can also be achieved through application of a stream of ozone, resulting in a silicon oxide surface with a high percentage of terminal silanol functionality that is readily to linked to various silanol functional groups.[8] The oxide surface is negatively charged in a solution with pH > 2. This property has offered an opportunity to study electrostatic interactions between the pore walls and the analytes in porous Si. Understanding molecular behavior in such restricted environment provides insight to enhance protein loading [32] and charge effect on biomolecule diffusion in nanopores.[33] These oxidized surfaces were found to susceptible to nucleophilic attack, and readily dissolve in aqueous media.[34] The dissolution of oxidized porous Si in media may have limited its long-term stability in sensing applications but this property has been found to be favorable for drug delivery in which biodegradable and biocompatible are keys for synthetic drug delivery vehicles. In addition to biodegradability, thermal oxidized porous Si microparticles were found to serve as inert carriers for the long-term release of the anthracycline drug daunorubicin. Without prior oxidation, porous Si undergoes an undesirable side reaction with this redox active drug.[35]

1.3.2 Formation of Si−C bonds

The formation of Si−C bonds to graft organic functional groups is another approach to modify porous Si surface by nucleophilic attacking the unstable Si−H bonds from exposed nanocrystalline material. Thermal,[36] radical mediated,[37] and UV photolytic[38, 39] alkene hydrosilylation is known to occur on flat Si (100) and Si(111) hydride surfaces. The electrochemical reduction of organoiodides or bromides at porous Si has been shown to lead to attachment of the organic groups to the porous silicon via Si−C bonds.[40, 41] Carbonization of porous Si by thermal decomposition of acetylene[42] and poly(furfuryl alcohol)[43] are other approaches to place carbon species on porous Si surfaces.

Chidsey et al. first recognized the lower electronegativity of carbon relative to oxygen translates to greater kinetic stability of Si−C grafted species on silicon surfaces.[37] Monolayer based on Si−C bonds may provide additional functionalities since the vast resources of organic and organometallic chemistry can be accessed, providing both stability and feasibility to control over the interfacial characteristics.[44] Table 1.1 summarizes surface chemistries that are commonly used to stabilize porous silicon surfaces.

Table 1.1 Examples of different surface chemistries for porous silicon samples.

Process	Chemical Reaction	Surface Species	Contact Angle(°)
Freshly etched		Si–H	102 ± 3
Ozone oxidation	Si–H + O_3 →	Si–O–Si, Si–OH	11 ± 1
Thermal oxidation (600 °C, 90 min)	Si–H + O_2 →	Si-O-Si	20 ± 1
Hydrosilation with 1-dodecene	Si–H + CH_2=$CH_2(CH_2)_9CH_3$ →	Si–$(CH_2)_{11}CH_3$	119 ± 2
Thermal acetylation (485 °C, 30 min)	Si–H + H–C≡C–H →	"Si–C"	80 ± 3

(Adapted from Reference[45])

1.4 Strategies for Differential Surface Functionalization in Porous Materials

While earlier work concentrated on developing high coverage chemical species on porous Si to either passivate or to graft functional species, 2-D surfaces with micro-topological and nano-topological features or surface comprising gradients of chemical compositions[46] have gained much interest recently. The distinct chemical regions with micro-topological features allows for high-throughput screening study such as cell-based microarrays in response to various stimuli. The gradient in chemical compositions on surface enables control of cell spreading or protein concentration in a smooth fashion. Table 1.2 lists few techniques used for surface patterning to create spatially distinctive chemical distribution. Photolithography is the most popular technique to prepare high-precision and high-resolution pattern. Techniques for creating spatially resolved chemical distribution in porous materials utilizing the porous nature will be addressed in this section. Chapter 2 and chapter 3 in this thesis will address approaches to achieved selective modification on porous Si thin films.

Table 1.2 Overview of surface patterning techniques for spatially controlled chemical species distribution in thin films.

Technique	Advantages	Disadvantages	Procedure Requirement
Photolithography	•Sub-micron resolution	•Require rigorous laboratory procedures •Clean environment required	•Deposition of a photoresist layer •Subsequent UV irradiation using a photomask
Microcontact printing (soft lithography)	•Micron resolution •Lower cost and relative experimental ease	•Limited number of molecules and substrates that can be used	•Use of a photolithography or replica molding for the formation of a patterned stamp, which is then used to transfer thiolated SAMs onto gold or silanes onto glass
Contact and non-contact printing	•Micron resolution •Quick and simple pattern formation	•No mechanism for spatial confinement •Patterned shape limited to pin (contact printing) •Uneven adsorption of biomolecules on each spot	•Spotting of biomolecules onto localized addressable regions

(Adapted from reference[47])

1.4.1 Photolithography on Porous Thin Films

Microfabrication to pattern parts of a thin film on a substrate using photolithography is well established and extensively used in the semiconductor industry to prepare spatially-resolved chemical compositions that protect or allow subsequent chemical processes for preparing delicate nanostructures. This process involves light to transfer a geometric pattern from a photomask to a light-sensitive chemical photoresist on a substrate. A series of chemical treatments that either engrave the exposed area, or enable deposition of a new material to form a designed pattern. A spatially addressable parallel chemical synthesis that yields a highly diverse set of chemical composition can be achieved using solid-phase chemistry, photolabile protecting groups, and photolithography.[48]

Lithographic fabrication of micron-dimension porous Si structures exhibiting optical interferences and visible luminescence with polycontrast images is demonstrated by varying the light intensity that translated into a variation in etching rates at the Si electrode.[49] As-prepared porous Si thin films possess mainly hydride species on the substrate. This lithographic patterning can be translated to other photochemical reaction such as UV-light mediate hydrosilylation on porous Si as a postsynthetic modification to graft organic functionalities. Stewart et al. demonstrated a photopatterned hydrosilylation on porous Si where a photomask is applied to protect part of the region from reaction and allow for attachment of alkene species onto exposed area via Si–C bonds in spatially well-resolved domains.[50]

1.4.2 Layering Surface Functionalization in Porous Thin Films

Dressing differential chemistries in layers of porous thin films have been demonstrated in both anodic etched porous silicon and anodic aluminum oxide membranes. Link et al. has demonstrated preparation of Janus-like porous Si microparticles that are capable to spontaneously assemble, orient, and sense their local environment.[51] These microparticles are prepared by electrochemically etching two discrete porous multilayered dielectric mirrors into Si, with one on top of each other. The first mirror is chemically modified by hydrosilylation with dodecene followed by anodization of the second layer, and later modified by mild thermal oxidation. The films are subsequently lift-off from the substrate and fractured by sonication. These chemically asymmetric particles can spontaneously align at an organic liquid−water interface, with the hydrophobic side oriented toward the organic phase and the hydrophilic side toward the water. This strategy of anodization etching and chemical modification in tandem to generate layered porous structures with distinct chemical functionalization has also been realized on anodic aluminum oxide (AAO) membranes with double- or triple-layered nanostructures.[52, 53] With careful control in the thickness of top layer, a preferential modification of "external" surface from the "internal" surface can be prepared.

1.4.3 Chemical Gradient on Porous Thin Films

Chemical gradients prepared on flat or porous surface have advantages over distinct region where the molecular−surface interaction can be controlled in a smooth transition. Strategies to apply the chemical gradient include photochemical, chemical hydrosilylation, and electrochemical modification to create chemical composition gradients across porous silicon.

Guan et al. demonstrated a wavelength-tuned irradiation approach to prepare a depth-resolved chemical modification of porous Si.[54] This method utilizes the limitation of penetration depth of UV light in UV-assisted hydrosilylation to preferentially decorate alkyl functional groups at the top surface of mesoporous silicon thin film. A white light with greater penetration depth was later used to functionalize the pore surface in further depth on a porous thin film.

Another example to prepare chemical gradient in porous Si is demonstrated by vertically orienting the sample in the initiator contianing a concentration gradient, leads to a gradient in chemical species after hydrosilylation reaction.[46]

Employment of asymmetric placement of the cathode generates a porosity gradient in porous Si thin film by creating a current density gradient across the surface.[21] Electrochemical reduction of organoiodides or bromides on porous Si with such current density gradient can be used to generate of a pore wall modification gradients across the thin porous Si layer. Figure 1.4 shows the diagram of asymmetric placement of cathode and chemical gradient prepared as described.

(A)

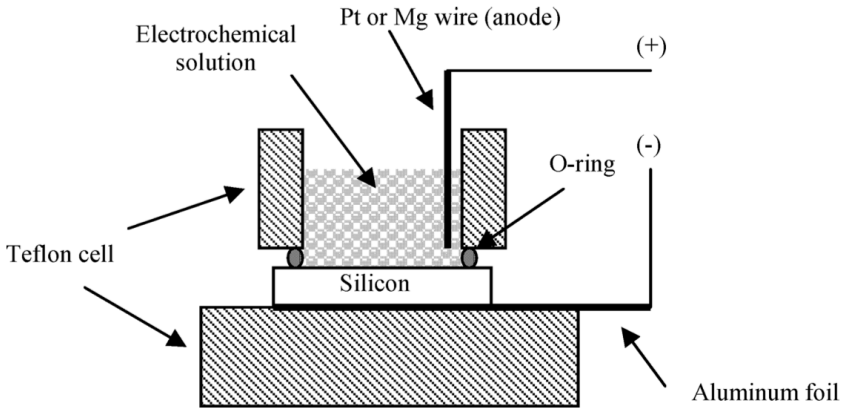

(B)

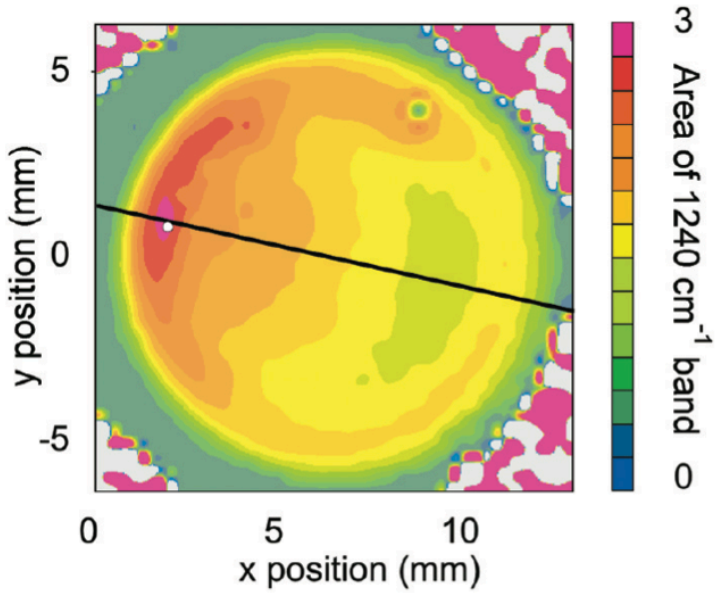

Figure 1.4 Chemical gradient in porous silicon prepared by asymmetrical electrochemical reaction. (A) Diagram of the cell used for the asymmetrical modification (ref 18, 23 in Thompson, Langmuir 2010). (B) Transmission FTIR microscope map showing changes in the peak area intensity of the C–O stretching mode (at ~1240 cm^{-1}) across a porous silicon sample with a gradient of pentyl acetate groups and then end-capped with methyl groups (o, counter electrode position; cathodic current density of 1-5 mA/cm^2 for 45 s). (Reprint from reference[46]).

1.4.4 Differential Modification Utilize Surface Tension and Size Exclusion in Porous Materials

Porous materials with tunable pore dimension have been used widely in molecular separation based on size exclusion.[21, 24, 55] This physiological property can also be employed in placing functional groups on the exterior surface of porous materials and create differential chemical species distribution from the interior surface.

Gartmann et al. performed postsynthetic functionalization on arrays of silica nanochanneles (ASNCs) and spherical particles of the SBA-15 type systems with three different silane functional groups and observed selective functionalization over the external surface based on steric hindrance.[56] Furthermore, the mobility of functional groups with which they diffuse into the porous matrix can also be controlled by polarity of solvent. The more polar solvents (ethanol and acetone) are expected to penetrate further compared to less polar solvents (toluene and THF) and result in more uniform functionalization. Alternatively, surface functionalization of the inner surface with hydrophobic species allows additional control in solvent mobility, allowing differential placement of functional groups on the exterior surface than the interior surfaces. The hydrophobic property of the interior surface of the porous Si thin film was used to prevent infiltration of water containing reactive species; only the exterior surface of the porous film was subjected to chemical medication.[57] This approach is of particular interest in porous materials where the combination of surface tension and capillary force can either prevent or promote the ingress of solution species inside the porous matrix. This process has potential to be employed for selective modification of porous particles,

which can not be achieved by lithography methods where strict orientation of surface to stimuli is required.

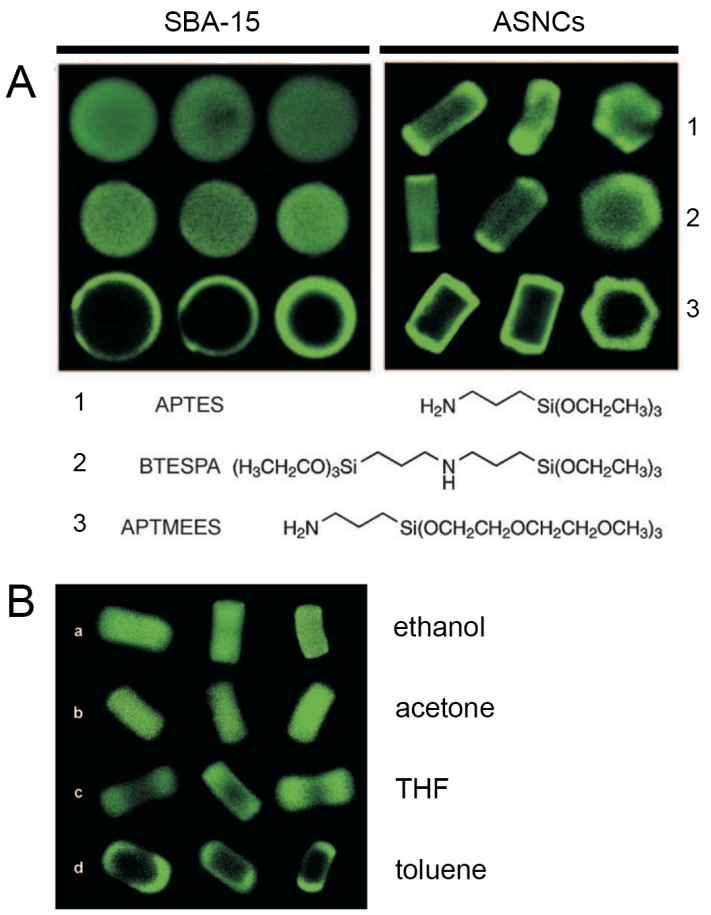

Figure 1.5 CLSM images of functionalized mesoporous silica. (A) Images (after FITC labeling) of SBA-15 and ASCNs functionalized with APTES, BTESPA, or APTMEES. Three particles are shown for each silane/silica combination. (B) Images of calcined ASNCs after functionalization with APTMEES in ethanol (a), acetone (b), THF (c), toluene (d), and subsequent FITC labeling. (Reprints from reference[56]).

1.5 Methods for Surface Chemistry Analysis

Successful selective chemical functionalization requires careful characterization and verification prior interpretation of performance. Spectroscopic surface analytical techniques, infrared (IR) spectroscopy, X-ray photoelectron spectroscopy (XPS), and time-of-flight secondary ion mass spectroscopy (ToF-SIMS) have been applied to the characterization of chemical species present at the surfaces.[58] The XPS and ToF-SIMS are attractive for surface analysis because they can provide compositional information in depth profile with few nanometer resolution. Other techniques, such as scanning electron microscopy (SEM) with EDX, have also been used for elemental analysis on determining the distribution of elemental profiling in additional to topographic information. Techniques that have been used extensively for the surface topography and chemical surface characterization in porous materials are listed in Table 1.3.

Table 1.3 Analysis methods for the surface topography and chemical characterization of surfaces. (Adapted from reference [59])

Method	Sampling Depth (Spatial Resolution)	Information Obtained	Disadvantages
Surface Topogrpahy			
Scanning electron microscopy (SEM)	Atomic to few microns	Topography	Limited chemical information.
Atomic force microscopy (AFM)	Atomic to 20 μm	Topography, coverage	Artefacts, contamination. Limited chemical information.
Confocal laser scanning microscopy (CLSM) [56]	Few microns	Fluorescent probes distribution	Fluorescent probe conjugation required for imaging.
Chemical Characteriazation			
SEM coupled with energy-dispersive (EDX) analyzer	Few microns	Topography, elemental analysis	Limited to elemental information.
Infrared spectroscopy (IR) equipped with microscope[46]	1- 5 μm (400 μm)	Chemical	Dry state. Sensitivity varies depend on chemical bonds. Environment sensitive.
Raman spectroscopy	1–5 μm	Chemical	Sensitivity varies depend on chemical bonds. Environment sensitive.
Time-of-flight secondary ion mass spectroscopy (ToF-SIMS)	< 5 nm (500 Å)	Chemical; molecular fragments provide structure information	Dry state, vacuum, very sensitive to contamination
X-ray photoelectron spectroscopy (XPS)	2-10 nm (5 μm)	Elemental, chemical	Dry state, vacuum. Mainly elemental information
Contact Angle	1 nm	Surface energy	Dry state
Ellipsometry	300 nm	Adsorption kinetics	Model-based. Refractive indices required for all layer

1.6 Outlook for Micropatterned in Porous Materials

The tunable pore dimension, ease of surface functionalization and unique optical properties have rendered porous Si an attractive material for chemical/biomolecule sensing and drug delivery. Design of appropriate surface chemistry for specific drug payloads is key to provide compatibility with payload and targeted tissue. Moreover, sustained drug delivery can be achieved with suitable surface functionalization. To achieve higher sensitivity, selectivity, and stability in porous Si-based sensor platforms, extensive research have been input to characterize effect of surface functionalization on relevant applications. Besides the uniform modification of porous Si throughout the whole surface area, differential modifications that address chemical distinct species on the porous matrix may open new possibilities to improve performance of porous matrix in existing applications.

High-throughput screening and analysis of complex gas mixtures or biomolecules require the development of new sensors with inherent information density.[46] Patterned microarrays with well-characterized composition, in distinct regions or gradient fashion, across a sensor surface are promising to perform the complicated tasks. In order to fulfill such needs, differential surface modification on porous materials provides a promising approach in which higher density can be enclosed in the system. Future direction in differential placement of chemical species in spatially-resolved domains on porous materials to target applications is not limited by aforementioned strategies but to provide insight for designing more effective routes for functionalization in porous materials.

This section lists applications utilizing diverse chemical compositions on flat surface. Including distinct chemical functionalities on porous materials may lead to more application in which the capability of separation, filtration, inherent sensing can all be built on the same platform. In addition, development of methods for high-throughput data analysis by used of imaging tools or microscopes and integrated image analysis software would aid on analytical interpretation.

1.6.1 Molecular Sensor Arrays

Recent advances in the design of porous Si-based interferometric biosensors to detect a variety of biomolecular complex, including oligonecleotides,[9, 17, 60] antibody-antigen interactions,[29] enzyme-substrate interactions,[24, 61] and virus-host interactions.[62] It is desirable to fabricate porous Si-based microarrays each with specific recognition elements that would allow real-time monitoring of molecular interactions. Functional surface chemistries controlling the attachment of biomolecules have enabled fundamental study to rapidly uncover the functions of genes and to identify and analysis of gene products in parallel.[63] Advanced manipulation of biomolecules with the ability to adsorb, desorb, bind or prevent adsorption of biomolecules in localized regions, combined with the ability to switch between these processes on demand or upon activation by specific stimuli is highly desirable to understand fundamental molecular-surface interactions.[47]

1.6.2 Drug Delivery Vehicles

Porous Si micro- and nanoparticles have gained a lot of interests for drug delivery in past decade given its high surface area, large pore volume, tailored surface chemistry for biocompatibility with varies cell lines and tissues, and biodegrade properties. Deliverable molecules includes small molecules to larger proteins have been demonstrated with porous Si-based delivery systems.[32, 64-66] The molecular-surface interactions provide ways to tailor the release profiles. A burst release is commonly observed when a hydrophilic small molecule was loaded into the mesoporous matrix and released into the biological relevant media. Sustained release of small molecules remains a great challenge in the drug delivery application. Strategies to achieve the sustained release include grafting porous surface with organic functional groups to controlled adsorption and desorption of drug payloads.

An ideal drug delivery carrier would be capable to present functional group at the outer surfaces to enable regulating the cellular uptake[67] or to provide targeting ability.[68] The inner surface should be compatible with drug payload that payload retain its functionality after released off the matrix; the inner surface should also provide high affinity towards the drug payloads for enhanced loading capacity. These are common challenges faced in designing nanoparticle for drug delivery. Successful differential modification in porous matrix may be key to meet the challenges.

CHAPTER TWO

DIFFERENTIAL ADSORPTION OF SMALL MOLECULES IN SPATIALLY FUNCTIONALIZED POROUS SILICON NANOSTRUCTURES

2.1 Abstract

An experimental approach to rapidly quantify the relative affinity of a small molecule analyte for two different surfaces is described. The method uses optical measurement of high surface area porous Si thin films that contain two spatially distinct surface chemistries. The chemistries are placed on the walls of the ~10 nm-diameter pores of the porous Si film by means of microdroplet patterning, where a chemical resist is drop-coated on the porous Si sample to define distinct regions across the plane of the chip. In this work the two chemistries consist of a hydrophilic silicon oxide surface and a hydrophobic methyl-terminated silicon surface. Detection is achieved by simultaneous optical reflectance measurement of both regions, where the reflectance spectrum contains a convolution of the Fabry-Pérot interference spectrum of both the oxide and the methyl-grafted layers. The differential partitioning of a test analyte (2-acetoxybenzoic acid or diphenyl ether) from aqueous solution is determined from the Fourier transform of the optical interference spectrum. The approach is rapid, nondestructive, and it can be performed on a small sample volume as a means to quantify the partition behavior of small molecules.

2.2 Introduction

Surface chemistry has a strong influence on the binding and transport of molecules in the restricted environment of a mesoporous material. Studies on the transport of molecules inside pores functionalized with various chemically grafted or self-assembled species have shown that electrostatic interactions, hydrogen bonding,

and van der Waals forces can affect adsorption and transport, and these parameters are highly dependent on pH and ionic strength.[29, 33, 69-73] The restricted environment of a nanopore can dramatically enhance the effect of surface chemistry, especially when the dimensions of the pore approach the dimensions of the molecule being transported.[69, 74, 75] In this context, the advantage of mesoporous materials is twofold: first, they provide a means to enhance molecular separations; and second, they can reduce the volume of sample needed for molecular sensing.[76, 77] For electrically neutral molecules, van der Waals and hydrogen bonding forces are the important factors influencing transport in mesoporous systems. For example, Au nanotube membranes functionalized with hydrophobic alkanethiols, or porous Si films containing grafted alkanes show selective transport of hydrophobic molecules.[73, 78] The separation efficiency of a mesoporous membrane is often determined by ex-situ chromatographic, mass spectral, UV–Vis[79, 80] or fluorescence spectroscopic[55] methods, although *in situ* electrochemical or optical probes are of particular interest for miniaturization of mesopore systems.

Recently, improvements in the fidelity of analyte detection have been demonstrated by simultaneous detection of two distinct regions of chemically modified mesoporous Si thin films.[81-84] These experiments focused on gas phase analytes, and detection was achieved by acquisition and deconvolution of the optical spectra originating from chemically distinct regions of the optical sensor. By selective illumination[81] or positioning[82-84] of the detection regions, differential information is obtained that can allow the sensor to correct for zero point drift or interfering analytes.

In this chapter, we explore an in situ method to determine the partitioning of an analyte between a hydrophobic domain and a hydrophilic domain in a mesoporous silicon nanostructure. The two small but physically separated thin film domains are generated using a two-step patterning procedure previously developed in our group called microdroplet patterning.[85] This generates a hydrophobic region, containing surface-grafted methyl groups, adjacent to a hydrophilic region consisting of a thermally oxidized porous Si layer. The thermal oxidation[86, 87] and electrochemical grafting of methyl species[41] were previously reported to provide a higher surface coverage of chemical bonds throughout the porous Si thin film and therefore better stability. The resulting structure can be interrogated using an optical probe focused on a spot that overlaps the two regions. The thin film interference spectrum contains information on the composition of both films, which can be deconvoluted by Fourier transform. We show that the method allows quantification of the relative partitioning of a test molecule between the two domains.

2.3 Experimental Methods

2.3.1 Materials

2-acetoxybenzoic acid (USP grade), diphenyl ether (ReagentPlus, 99%), lithium iodide (beads, 99%), toluene (anhydrous, 99.8%), glacial acetic acid (USP grade) and polystyrene (analytical standard, for GPC, molecular weight 10 kDa) were obtained from Sigma-Aldrich Chemicals. 48% aqueous hydrofluoric acid (ACS grade) and acetonitrile (certified ACS, ≥99.5%) were obtained from Fisher Scientific.

Iodomethane (99%) was purchased from Acros Organics. Absolute ethanol (200 proof) was obtained from Rossville Gold Shield Chemicals. Boron-doped single-crystalline p-type Si wafers (0.8-1.1 mW-cm resistivity, polished on the (100) face, 500-550 mm thick) were obtained from Siltronix, Inc.

2.3.2 Preparation of Porous Silicon

Porous silicon samples 1.2 cm in diameter were prepared by anodic electrochemical etch of pieces of the silicon wafer in an electrolyte consisting of 3:1 (v:v) aqueous 48% HF:ethanol at a constant current density of 75 mA/cm^2 for 5 min, using a 16 mm diameter Pt gauze (100 mesh) as the counter electrode. (CAUTION: HF is highly toxic and contact with skin should be avoided.) The freshly etched porous Si thin films were thoroughly rinsed with ethanol and dried under a stream of nitrogen.

2.3.3 Spatially Resolved Electrochemical Grafting of Methyl Groups

The as-etched porous Si samples were thermally oxidized in a tube furnace (Lindberg/Blue M) in air at 600 °C for 30 min. A portion of the oxidized sample was then protected with a polystyrene mask by placing a drop of 8 microliters of a toluene solution containing 13% by mass polystyrene (molecular weight 10 kDa) slightly off from the center of the chip. The polystyrene solution spread over a small portion of the chip, leaving the rest of the film uncoated. The sample was subsequently heated for 10 min at 90 °C to dry the solvent and facilitate polymer infiltration. The resulting polystyrene layer covered approximately half of the partially oxidized porous Si film,

and complete infiltration of the polymer was confirmed by optical reflectance spectroscopy. The sample was then dipped in 1:1 (v/v) HF: ethanol solution to dissolve the thin oxide layer from the unprotected region of the porous Si film and generate Si-H bonds on the exposed inner pore surfaces. The sample was then subjected to electrochemical methylation as previously described, using an electrochemical cell fitted with a transparent glass cap and valves to allow anaerobic processing.[19] The electrolyte consisted of 0.2 M iodomethane and 0.2 M anhydrous LiI in acetonitrile, which was freeze-pump-thaw degassed three times to remove traces of oxygen prior to use. The electrolyte was transferred into the anaerobic electrochemical cell via syringe, and the apparatus was placed under a nitrogen atmosphere. A cathodic current of 5.4 mA/cm2 was applied for 120 s with a tungsten halogen lamp (EiKO type ELH, 120V 300W) illumination (300 mW/cm2). The glass cap was then removed and the sample was rinsed three times each with glacial acetic acid, acetonitrile, ethanol, and then dried in a stream of nitrogen. The polystyrene mask was then removed by soaking the sample in toluene for 30 min and rinsing the sample with 3 separate aliquots of toluene, followed by ethanol and drying under a stream of nitrogen.

2.3.4 Material Characterization

2.3.4.1 Scanning Electron Microscopy

An FEI XL30 ultra-high resolution scanning electron microscope (SEM) operating at an accelerating voltage of 5 kV was used to obtain plan–view and

cross−sectional images of the samples. Samples were not coated with metal or carbon prior to imaging, and low beam currents were used to avoid sample charging artifacts.

2.3.4.2 Infrared Spectroscopy

The pore wall modifications were characterized using attenuated total reflectance (ATR) Fourier transform infrared (FTIR) spectroscopy. Spectra were acquired on a Thermo Scientific Nicolet 6700 FTIR spectrometer with a Smart iTR sampling accessory. Spectra were acquired in the range 600-4000 cm-1 with a resolution of 4 cm-1 and 128 scans were averaged per spectrum.

2.3.4.3 Water Contact Angle Measurements

Water contact angle measurements were obtained by imaging a 5 mL water droplet on horizontal porous Si samples using a Canon XSi digital camera with 100 mm macro lens. The contact angle was determined using the ImageJ image analysis software (NIH). Each reported contact angle represents the average of triplicate measurements on three separate chips.

2.3.5 Optical Reflectance Spectroscopy and Spectral Analysis

Reflectance spectra were collected using an Ocean Optics S2000 CCD spectrometer fitted with a bifurcated fiber optic cable. An unpolarized tungsten light source (Ocean Optics LS-1) was focused at the boundary of two distinct chemistry regions on the porous Si chip, with a spot size of approximately 1 mm2. Optical spectra

were processed using algorithms described previously.[19] Refractive indices for solvents were measured using a Refracto 30GS refractometer (Mettler Toledo).

2.3.6 Chemical Partition Experiments

The focal point of the optical probe was placed at the boundary between the hydrophilic and the hydrophobic region of the chip, enabling simultaneous interrogation of both surface types. Analyte transport experiments were carried out by introducing 5, 10 and 20 mg/mL of 2-acetoxybenzoic acid or diphenyl ether in solutions containing 80% methanol and 20% aqueous 50 mM citrate buffer (by volume) in a flow cell (flow rate of 0.7 mL/min). The high concentration of methanol was used to avoid precipitation of diphenyl ether, which has a low solubility in water. For consistency, all analyte solutions used this same 80:20 methanol:water matrix. Sample volumes of 3 mL were used to ensure that steady state analyte partitioning between the two chemically distinct regions was achieved. The pH of the citrate buffer was adjusted to 3.48 for the 2-acetoxybenzoic acid (pKa = 3.48) solution, and 3.67 for the diphenyl ether solution. For each experiment, a series of optical spectra were acquired every 8 s. Each of these spectra were themselves an average of 30 sequential 30 ms spectral acquisitions.

2.4 Results and Discussion

2.4.1 Synthesis and Characterization of Spatially Functionalized Porous Si Films

Figure 2.1 summarizes the synthetic procedure used to prepare the porous Si samples. A silicon wafer was first electrochemically anodized in an HF-containing electrolyte to generate a porous layer with average pore size (determined by SEM analysis, Figure 2.2a) of 9.4 ± 1.3 nm and thickness of 13.8 ± 0.2 μm (Figure 2.2e). Average porosity at this stage was 48% (determined using the spectroscopic liquid infiltration method, or SLIM[19]). The sample was then oxidized at 600 °C, which placed a thin oxide layer on the surface of the porous Si skeleton. The average pore size at this stage decreased slightly to 9.2 ± 1.5 nm (Figure 2.2b), and the average porosity decreased to 44%, consistent with the volume expansion expected upon conversion of Si to SiO_2. A portion of the oxidized film was then masked with polystyrene by addition of a drop of a toluene solution of polystyrene, which spread to cover half of the surface. We have previously shown that this "microdroplet patterning" method infiltrates the porous nanostructure and protects it from chemical attack.[85] Exposure of the entire sample to aqueous ethanolic HF caused the selective removal of oxide in the region of the film that was not protected by the polystyrene mask. The surface of the silicon skeleton remaining after oxide removal was hydrogen terminated.[88] Methyl species were then grafted to this reactive Si–H surface by electrochemical reduction of CH_3I following the published procedure,[19] which generated what we refer to in this paper as the hydrophobic domain. Removal of oxide and attachment of $Si–CH_3$ species

resulted in increased average pore size (to 12.6 ± 1.7 nm, Figure 2.2c) and increased average porosity (to 70%) in this region of the film. The polystyrene mask was then removed by dissolution in toluene, which resulted in the two-domain (hydrophobic/hydrophilic) porous sensor structure used in this work (Figure 2.2d).

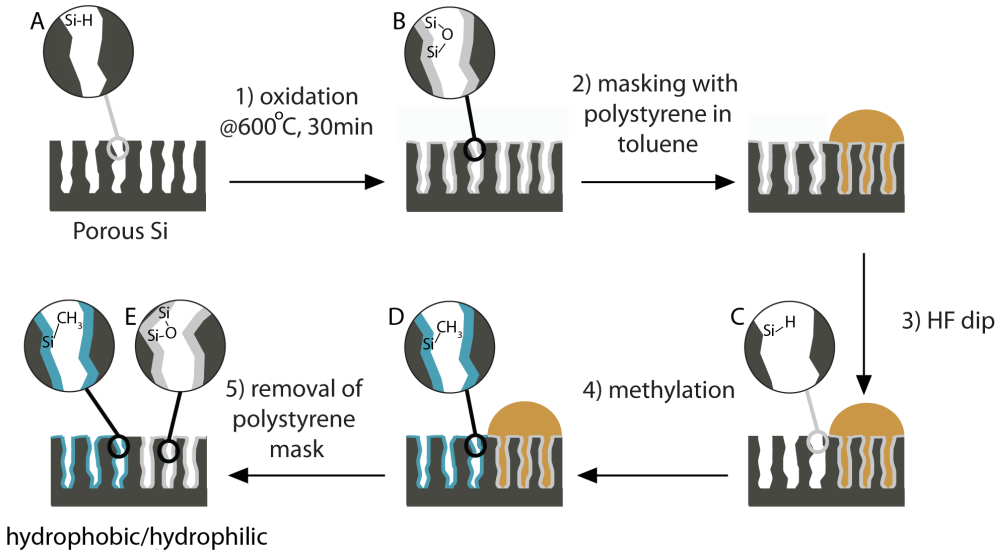

Figure 2.1 Schematic showing the preparation of surface-functionalized porous Si samples containing spatially separated hydrophobic and hydrophilic domains. (1) Freshly etched porous Si is thermally oxidized at 600 °C in ambient air for 30 min; (2) polystyrene is infiltrated in a small portion of the porous layer by drop-coating; (3) the unprotected portion of the porous Si surface is exposed to ethanolic HF solution to remove oxide and generate reactive Si–H species; (4) methyl species are grafted to the hydride-terminated portion of the surface by electrochemical methylation to generate the hydrophobic domain; (5) the protective polystyrene mask is removed to expose the hydrophilic silicon oxide domain.

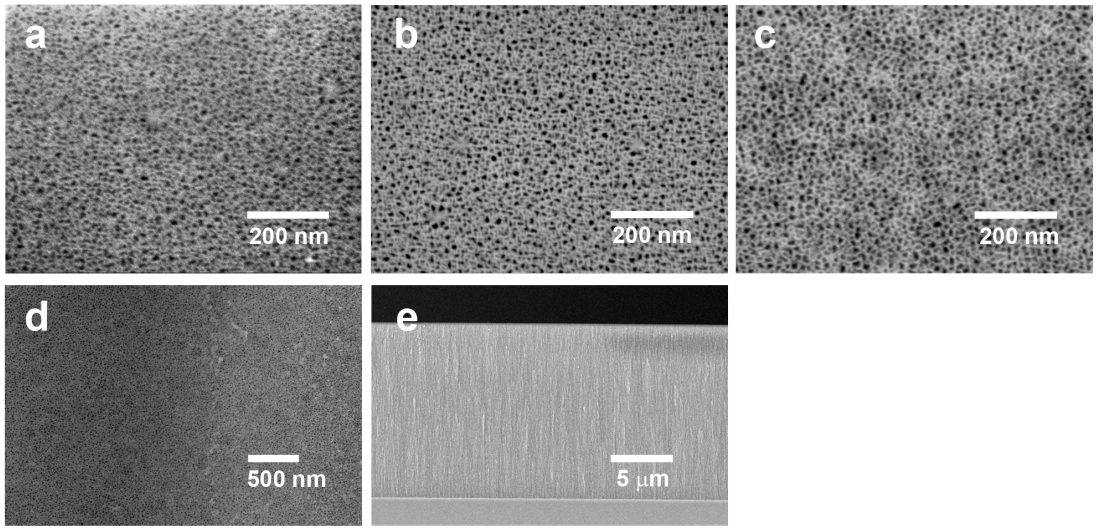

Figure 2.2 Electron microscope images of chemically modified porous Si samples. (a) Plan–view SEM image obtained from freshly etched porous Si film (Figure 2.1, step A); (b) plan-view image of the partially oxidized porous Si film (Figure 2.1, step B); (c) plan-view image of the methylated porous Si film (Figure 2.1, step D); (d) plan-view image obtained from the boundary between the two chemically distinct surfaces of the differentially modified porous Si film: the methyl-terminated surface is on the left and the oxide surface is on the right; (e) cross-sectional SEM image of the freshly etched porous Si film, showing the pore texture and the thickness of the porous layer.

Attenuated total reflectance Fourier-transform infrared ATR-FTIR spectrum of the freshly etched porous Si film (Figure 2.3A) displays bands characteristic of surface hydride species:[19] bands at 2109 and 2085 cm^{-1} associated with ν_{SiH2} and ν_{SiH} stretching modes, respectively, a band at 906 cm^{-1} assigned to the δ_{SiH2} scissor mode, and a band at 623 cm^{-1} for the δ_{SiHx} deformation mode. After furnace oxidation, a strong Si–O–Si stretching band appeared in the FTIR spectrum at 1020 cm^{-1} confirming the formation of silicon oxide. The region of the film that was subjected to electrochemical methylation displayed bands in the FTIR spectrum characteristic of the $Si–CH_3$ rocking mode at 762 cm^{-1}, along with weak C–H stretching bands (2973 and 2898 cm^{-1}), and C–H deformation bands (1403 and 1252 cm^{-1}). Vibrational bands associated with the polystyrene mask (aromatic C–H stretch at 3025 cm^{-1} and aromatic ring modes at 1600, 1492, and 1452 cm^{-1} were observed in the expected region of the masked sample (Figure 2.4), but they were absent from the spectrum of the sample after it had been rinsed with toluene (Figure 2.1, step E).

The interfacial free energy of each surface was quantified by water contact angle measurement. The silicon oxide surface showed a moderate wettability, with a contact angle of 40.2 ± 1.4° while the methyl-terminated surface had a lower surface energy, with a contact angle of 116.2 ± 1.2°. The measured values are similar to those given in previous reports on the two types of porous Si surface chemistries.[89]

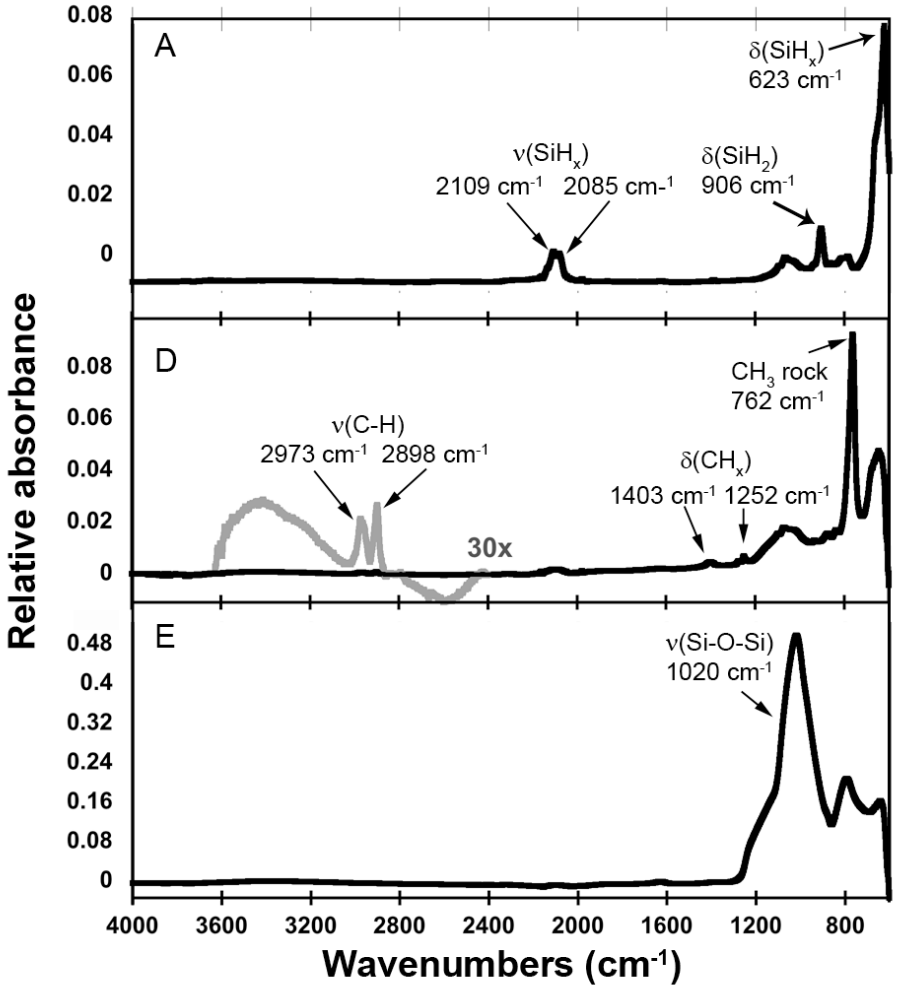

Figure 2.3 ATR-FTIR spectra of porous Si samples obtained from different regions of the spatially functionalized optical sensor and at different stages of the synthesis. (A) Freshly etched porous Si prior to chemical functionalization; (D) methylated region of the porous Si film corresponding to step D in Figure 2.1. A portion of the spectrum, shown in gray, is multiplied by 30 along the vertical axis; (E) oxidized region of the porous Si film obtained after removal of the polystyrene mask (Figure 2.1, step E). Lettering of each spectrum corresponds to the stage in the synthesis given in Figure 2.1.

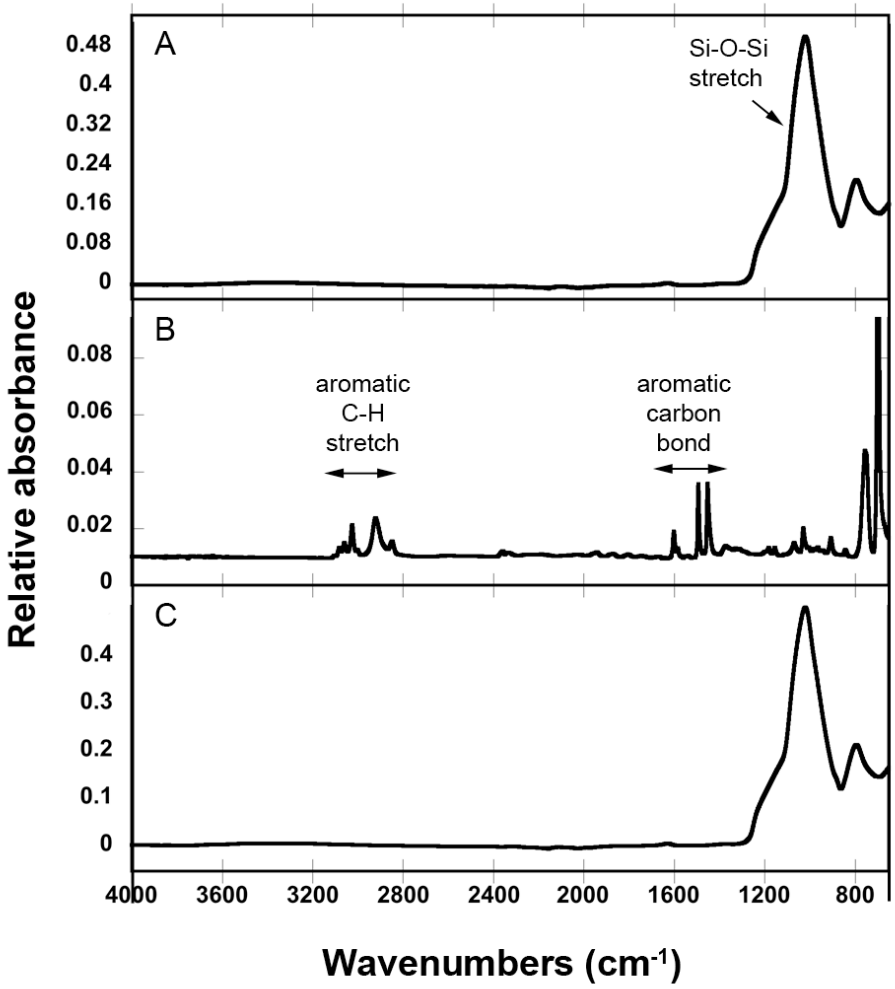

Figure 2.4 ATR-FTIR spectra of partially oxidized porous Si surfaces before and after polystyrene masking. From top to bottom: (A) partially oxidized porous Si (Figure 2.1, step B); (B) spectra of polystyrene; (C) partially oxidized porous Si film recovered from removal of polystyrene mask (Figure 2.1, step E).

2.4.2 Optical Characterization of Analyte Infiltration

Reflective interferometric Fourier transform spectroscopy (RIFTS)[19] was used to optically monitor the diffusion of analytes into both domains of the spatially functionalized porous Si film simultaneously. The focal point of the optics was a circle approximately 1 mm in diameter, and this spot was positioned at the border between the two domains on the sample, such that the reflectance spectrum (Figure 2.5a) contained the interference spectrum from both the hydrophobic and the hydrophilic regions of the chip. The interference spectrum results from thin film Fabry–Pérot interference of light reflected from the air/porous Si and porous Si/crystalline Si interfaces.[90] This rather complicated double interference spectrum can be deconvoluted by applying a fast Fourier transform (FFT) to the reflectance vs frequency spectrum (Figure 2.5a, inset),[19] which yields the value of the effective optical thickness of each of the two layers as separate quantities. The effective optical thickness is defined as $2nL$, where n is the average refractive index of the porous layer and L is the metric thickness of the film. Provided the two domains of the porous Si layer have significantly different values of $2nL$, the FFT spectrum will display two separate peaks, whose positions along the x-axis correspond to $2nL$ for each of the domains. In the present case, the large difference in porosity between the methylated and the oxidized regions (70% vs 44%, respectively) ensured that they would have spectrally resolvable values of $2nL$.

The samples were exposed to 2-acetoxybenzoic acid (aspirin) or diphenyl ether analytes in a 4:1 methanol: aqueous citrate buffer matrix and dose-response curves were obtained by monitoring the value of $2nL$ from the two porous Si domains

simultaneously, as described above and shown in Figure 2.5b and c. The quantity *2nL* was observed to increase with increasing analyte concentration. This is indicative of infiltration of analyte, because the two analytes under study have an index of refraction (1.506 and 1.579 for 2-acetoxybenzoic acid or diphenyl ether, respectively) that is larger than the methanol/aqueous buffer matrix (1.3393). Using the thickness of the porous Si film determined from SEM images and the refractive index of the analyte, a fit to the Bruggeman effective medium model was used to determine the mass loading of analyte in each domain of the porous Si sensor.[91, 92] This information was then used to determine the relative partitioning of analyte between the hydrophilic and hydrophobic domains.

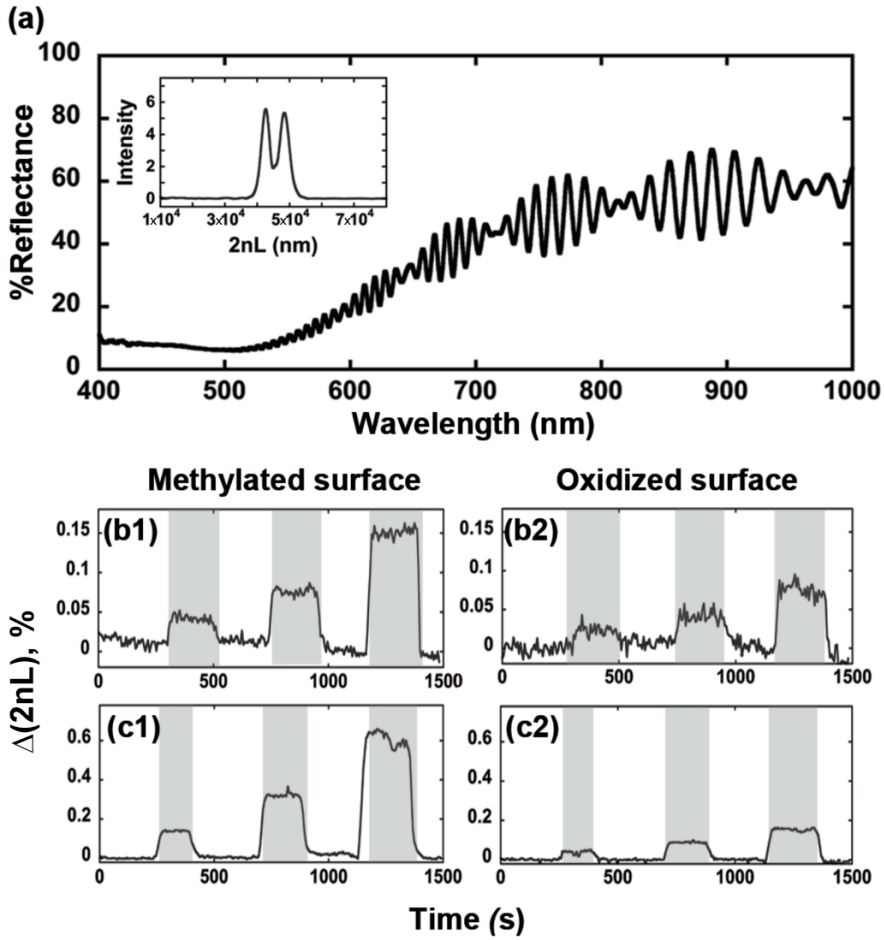

Figure 2.5 Optical response of the spatially functionalized porous Si film to test analytes. (a) White light reflectance spectrum obtained at the border between the two porous Si domains (methyl-terminated and oxide-terminated surfaces, as depicted in Figure 2.1). The spectrum measures thin film interference from both regions simultaneously. The Fourier transform of the reflectance vs frequency spectrum (inset) results in two peaks corresponding to the effective optical thickness ($2nL$) of each surface type. The left peak represents the methylated surface and the right peak represents the partially oxidized surface. (b1-b2) Representitive dose-response profiles obtained simultaneously from the methylated (b1) and the oxidized (b2) regions of the chip, upon exposure to increasing doses of 2-acetoxybenzoic acid. Analyte concentrations of 5, 10 and 20 mg/mL in 4:1 methanol:aqueous citrate buffer were used. (c1-c2) Representitive dose-response profiles obtained simultaneously from the methylated (c1) and the oxidized (c2) regions of the chip, upon exposure to increasing doses of diphenyl ether. Analyte concentrations of 5, 10 and 20 mg/mL in 4:1 methanol:aqueous citrate buffer were used. Sensor was flushed with clean 4:1 methanol:aqueous citrate buffer between all doses. Dosing periods are indicated in gray, while the flushing periods are indicated in white. The quantity Δ(2nL) represents the change in the position of the corresponding peak in the FFT spectrum from above.

2.4.3 Determination of Analyte Partitioning Between the Hydrophobic and Hydrophilic Domains of the Sensor

To explore the differential sensing capability of surface modified biphasic porous Si, 2-acetoxybenzoic acid, commonly known as aspirin, was chosen as the model hydrophilic compound; while diphenyl ether, a less polar molecule with a relatively weak hydrogen-bonding interactions with silica, was chosen as a hydrophobic compound. These two compounds have similar chemical structures and molecular weights but very different chemical properties, including their degree of hydrophilicity. The logarithm of the octanol-water partition coefficient (log *P*) for 2-acetoxybenzoic acid is between 0.77 and 1.28 (pH 3-4), while for diphenyl ether it is 4.21.[93, 94] The partition coefficient is defined as the ratio of equilibrium concentration of a chemical dissolved in two immiscible solvents that are in contact with each other, expressed by Equation 2.1.[95] The higher the log *P* value, the more hydrophobic the compound.

$$P = \frac{[analyte]_{octanol}}{[analyte]_{water}} \qquad (2.1)$$

The relative responses of the test analytes to the two types of the surface chemistries studied here can be interpreted in terms of their surface–molecular structure interactions, particularly the van der Waals and hydrogen bonding interactions. Hydrophobic interactions are attractive in nature, and the attractive force decays exponentially with distance[96]—these forces become negligible at distances > 20 nm.[97] In the present experiments, the average pore diameters were 9 nm (partially oxidized domain) to 13 nm (methyl–terminated domain) so the infiltrated molecules are in close proximity to the pore walls, allowing greater interaction with the surface. These

dimensions are also on the order of the Debye length of dilute electrolyte solutions.[33] Under the conditions of this study, the surface of the oxidized porous Si layer is expected to possess a net negative charge and the surface of the methylated porous Si layer is expected to be neutral. Diphenyl ether is uncharged at the pH used in this study, and so no electrostatic interactions are expected between this analyte and either of the two sensor surfaces. For the 2-acetoxybenzoic acid analyte, the pH of the matrix was set equal to the analyte pKa, so the half the analyte was in its negatively charged deprotonated state and half the analyte was in its nonionic, uncharged state. To minimize electrostatic interactions, the solution electrolyte concentration was set to 24.0–31.3 mM to provide a short Debye length.

Transport rates can be greatly affected as the pore size approaches molecular dimensions due to strong interactions between the pore walls and the molecule of interest.[33, 73] To evaluate the effect of surface-molecule interactions on the time-resolved dose-response curve, a first derivative was applied to the plot of change in optical thickness vs time. Such plots have been used previously to investigate the effect of diffusion in the restricted dimensions of mesoporous Si.[29] Comparison of the first derivative curves for the data obtained from the hydrophobic and the hydrophilic regions of the film (Figure 2.6 and 2.7) showed no apparent differences, suggesting the contents of the aqueous feeding solution diffused into both the hydrophilic and hydrophobic regions at rates too similar to be discerned by our instrumentation. This may be due to the large diameter of the pores in the films (9.2–12.6 nm) relative to the dimensions of the molecules (1 nm) or just weak surface-molecule interactions.

However, the rate of diffusion of diphenyl ether was detectably slower than 2-acetoxybenzoic acid in either film type. The slower rate of diffusion of diphenyl ether was observed during both loading and unloading of the pores for either film type (Figure 2.5 b1 vs c1, and b2 vs c2, and Figure 2.6, 2.7). Thus the rate of diffusion of an analyte in the porous films is detectable, but the effect of surface chemistry on this rate is not significant in the present system.

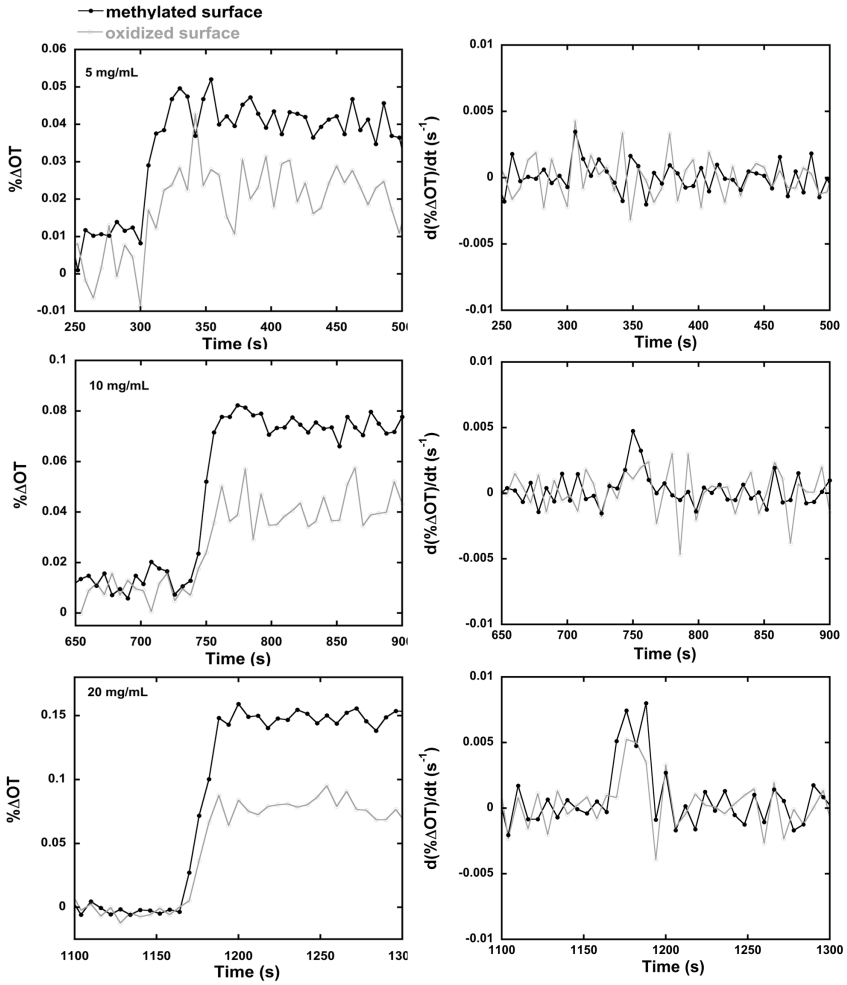

Figure 2.6 Left panel: dose-response curves of 2-acetoxybenzoic acid (5, 10, 20 mg/mL analyte concentrations, top to bottom) in the functionalized porous Si thin film. Responses from hydrophobic methylated (black) and hydrophilic oxidized (gray) region are expressed as the percent optical thickness change (%ΔOT) during the infiltration event as a function of time. Right panel: corresponding first derivative of the data shown in left panel. The points of the maximum rate of change indicate the infiltration events.

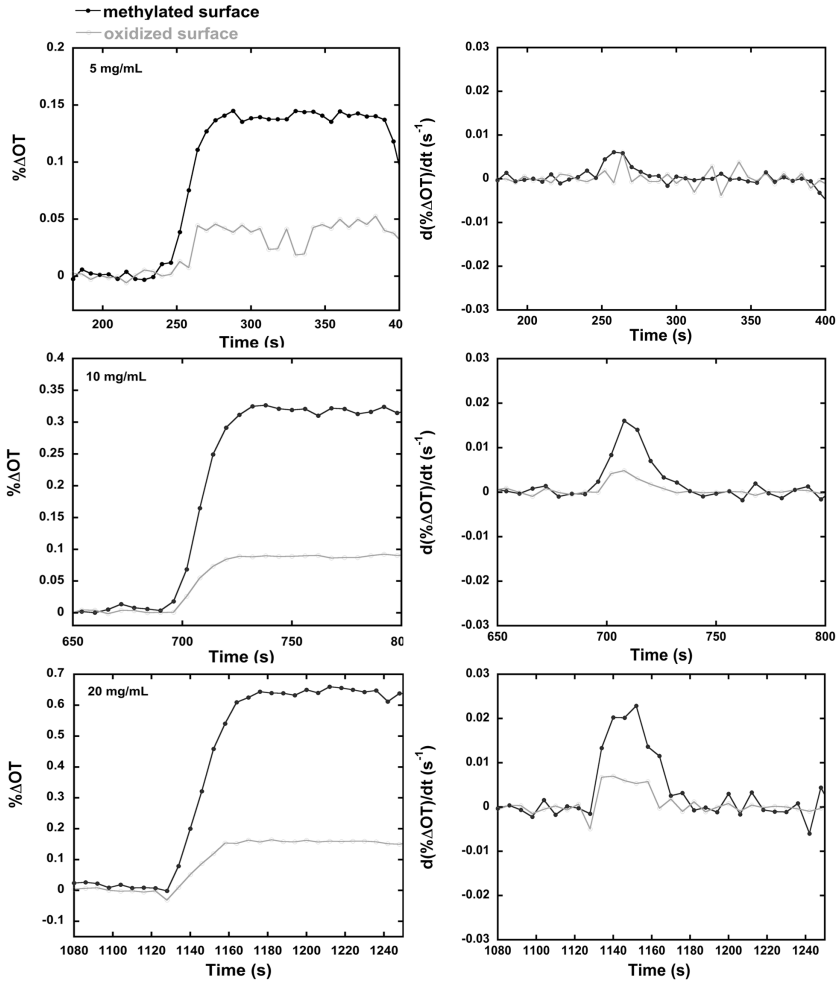

Figure 2.7 Left panel: dose-response curves of diphenyl ether (5, 10, 20 mg/mL analyte concentrations, top to bottom) in the functionalized porous Si thin film. Responses from hydrophobic methylated (black) and hydrophilic oxidized (gray) region are expressed in the percent optical thickness change (%ΔOT) during the infiltration event as a function of time. Right panel: corresponding first derivative of the data shown in left panel. The points of the maximum rate of change indicate the infiltration events.

Although there is no discernable difference in the kinetic behavior of the hydrophobic and the hydrophilic layers, there is a significant difference in the equilibrium selectivity of the two surface types for the test molecules. The equilibrium molecular partitioning values were obtained from the plateau in the dose-response profiles of Figure 2.5b-c. The changes in optical thickness between baseline and plateau were fit to the Bruggeman effective medium model to yield mass loading values, which were determined for both the hydrophobic and the hydrophilic domains. The adsorption selectivity of each surface was quantified using a separation factor (α), by taking a ratio of the mass loading values for each surface, Equation 2.2:

$$\alpha = \frac{(mass\ loading)_{Si-CH_3}}{(mass\ loading)_{Si-O-Si}} \qquad (2.2)$$

Separation factors determined at three different dosing concentrations (5, 10, and 20 mg/mL) are compared in Figure 2.8 for both 2-acetoxybenzoic acid and diphenyl ether. According to the definition in Equation 2.2, the more hydrophobic compounds will yield larger values of α. The analyte diphenyl ether displays larger α values (2.52-2.83) compared with 2-acetoxybenzoic acid (0.72-1.33) in the range of concentrations studied. The α values for the two test compounds are clearly separated ($p = 0.0010$, one-tailed t-test), showing that trend in the partitioning behavior is consistent with the difference in the hydrophobicity of the two test compounds.

The results show that the relative affinity of a molecule for two distinct surface chemistries can be determined in functionalized porous Si nanostructures with a single optical measurement. Advantages of this approach are that the measurement is rapid (~10 min including baseline) and it can be performed on a small physical volume (the

optics probed a volume of only 30 nL in this work). However, one of the intrinsic limitations of this system is the stability of silicon oxide in caustic environments, similar to other silica-based chromatography methods.[98] Although oxidized porous Si has been found to be sufficiently stable at neutral pH to allow a variety of biomolecular sensing experiments, it is a particular challenge for measurements of aqueous analytes at higher pH.[19]

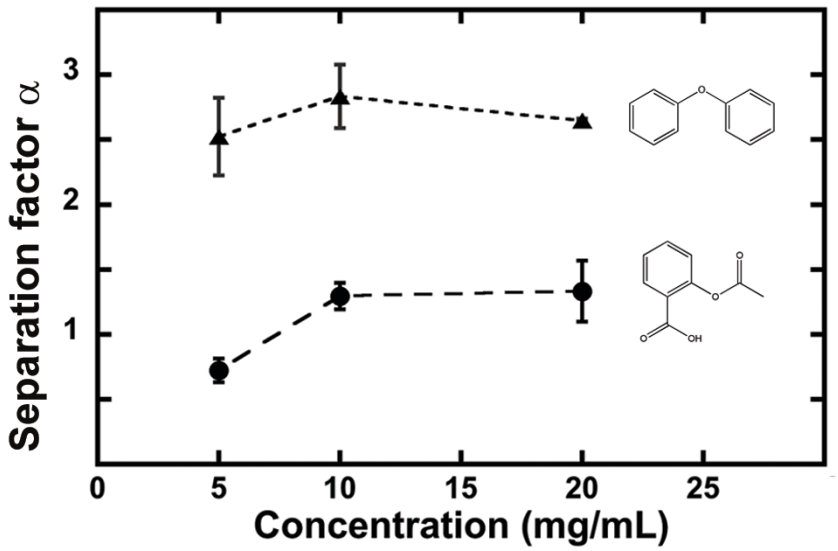

Figure 2.8 Relative affinity of 2-acetoxybenzoic acid (●) and diphenyl ether (▲) for the two porous Si surfaces (hydrophilic Si-O vs. hydrophobic Si-CH_3) measured at three different analyte concentrations. Relative affinity is quantified using the separation factor α defined in Equation 2.2. (Error bars represent one standard deviation of triplicate dosing experiments on the same sample, one sample per analyte).

2.5 Conclusions

The interior surfaces of mesoporous silicon can be modified into two distinct surface chemistries in the X-Y plane using a simple polystyrene masking technique without the need for lithographic patterning. Different chemical groups within the interior walls of the mesopores provide specific adsorption environments and introduce chemical selectivity into the system. Simultaneous interrogation of analytes interacting with the two different surfaces can be achieved using real-time optical reflectance spectroscopy. The partitioning of two model chemicals of different hydrophobicity was demonstrated using this system.

Chapter two, in part or in full, is a reprint (with co-author permission) of the material as it appears in the following publication: Wu, C.; Chen, M. Y.; Sailor, M. J., Differential Adsorption of Small Molecules to Spatially Functionalized Porous Silicon Nanostructures. *Langmuir*, 2013, 29, 11802-11808. The author of this dissertation is the primary author of this manuscript.

CHAPTER THREE

SELECTIVE FUNCTIONALIZATION OF THE INTERNAL AND THE EXTERNAL OF MESOPOROUS SILICON BY LIQUID MASKING

3.1 Abstract

A general approach for selective, differential functionalization of the interior and exterior surfaces of mesoporous Si is reported. The method employs two immiscible liquids, one inert and the other chemically reactive with the porous Si nanostructure. First, a porous Si sample is prepared by electrochemical etch and then it is mildly oxidized, which places a thin layer of silicon oxide at the surface. The inner pore walls of the partially oxidized porous Si film are then infiltrated with an inert liquid (octane). The sample is then immersed in aqueous solution containing hydrogen fluoride (HF), which serves as the reactive liquid. The hydrophobic phase is retained in the interior of the porous nanostructure, and $HF_{(aq)}$ attacks only the exposed surfaces of the oxidized porous Si sample, generating a hydrophobic, hydrogen-terminated (Si-H) outer layer. The reaction is self-limiting due to the immiscibility of octane and water, and the extent of penetration of the Si-H surface into the porous layer is dependent on the time of exposure to $HF_{(aq)}$. The Si-H surface can then be modified by thermal hydrosilylation (1-dodecene or 10-bromo-1-decene) in a subsequent step, resulting in a bifunctional porous Si film containing hydrophobic pore entrances to hydrophilic inner pores. The hydrophobic dodecyl species at the mouths of the pores is found to form a barrier for molecular transport; it decreases the rate of leaching (into water) of a rhodamine test molecule that is pre-loaded into the sample by >8 fold.

3.2 Introduction

Mesoporous materials with engineered surface properties are of interest for molecular separations,[99] catalysis,[100] drug delivery,[101] and chemical sensing.[102, 103] One

of the longstanding chemical challenges in engineering of nanomaterials is to control the placement of different chemistries in spatially distinct regions on a nanoscale object. Examples include Janus particles, where different chemical species are placed on opposite sides of a nanoparticle,[52, 104, 105] and core-shell nanoparticles, where the interior and the surface of a nanoparticle contain distinct materials.[106-109] Selective suface modification has been achieved with mesoporous silica nanoparticles either by co-condensation during the sol-gel synthesis or by post-synthetic grafting of commercially available substituted trialkoxy- or trichloro-silanes.[103] In addition, differential chemistries can be placed in or on porous nanostructures by using the inherent ability of the pores to exclude molecules larger than a certain size.[56, 110]

In the case of porous Si, chemical modification is usually performed either after,[111] or in tandem[51] with the electrochemical etching procedure employed in its synthesis. The differential chemistries of surface Si-H, Si-C, and Si-O species on porous Si have been harnessed to prepare Janus-like structures, and various functional groups such as negatively charged oxide or hydrophobic alkanes have been used to impart unique surface properties, such as self-alignment or differential analyte diffusion.[51, 73, 112] These materials are of interest for drug delivery,[11] chemical sensing,[46, 113] energy harvesting,[114, 115] and lab-on-a-drop types of applications.[116, 117] For the porous Si system, the ability to prepare pores of average diameter anywhere from 1 to 300 nm allows the harnessing of surface tension and capillary forces to promote or obstruct the infiltration of reagents for selective modification.[57] Recently, a photochemical hydrosilylation reaction has been shown to yield depth-resolved chemical

functionalization in porous silicon layers, where the depth of chemical modification depends on the wavelength of light used in the synthesis.[54]

In this chapter, we report a simple strategy for differentially modifying the inner pore walls in porous Si layers. The method uses a hydrophobic organic liquid as a chemical resist; it is infiltrated into the pores to mask the interior of the porous Si film, while the exterior surface and the pore mouths of the film are subjected to an aqueous chemical reaction with HF. This "liquid masking" method yields a hydrophilic silicon oxide surface deeper in the porous layer and a silicon hydride surface nearer to the opening of the pores. The Si-H and Si-O surfaces can then be modified using subsequent, orthogonal chemical reactions. Here we demonstrate a hydrosilylation reaction on the Si-H surface using dodecene, which yields a hydrophobic layer on the pore mouths. The hydrophobic outer layer over a hydrophilic inner pore structure is reminiscent of the structure of a liposome, and selective transport of molecular species (rhodamine B) across the hydrophobic barrier is demonstrated.[57, 102]

3.3 Experimental Methods

3.3.1 Chemicals and Materials

Highly boron-doped 0.9-1 mΩ-cm resistivity, (100) oriented and polished p-type silicon wafers were obtained from Siltronix, Inc. 48% aqueous hydrofluoric acid (ACS grade) was obtained from Macron Chemicals, Fisher Scientific. Absolute ethanol (200 proof) was obtained from Rossville Gold Shield Chemicals. Octane (puriss. p.a., ≥99,0%), hexane (CHROMASOLV® Plus, ≥95%), 1-octanol (~99%), toluene

(anhydrous, 99.8%), 1-dodecene (95%), mesitylene (98%), 10-bromo-1-decene (97%) and rhodamine B (dye content 90%) were obtained from Sigma-Aldrich and used without further purification. Phosphate buffered saline (10X, pH 7.4) was obtained as a stock solution from Mediatech, Inc. and diluted 10-fold by addition of deionized water prior to use. Acetone (HPLC grade) and acetonitrile (certified ACS, ≥99.5%) were obtained from Fisher Scientific.

3.3.2 Fabrication of Porous Silicon

Mesoporous Si films were prepared by anodic electrochemical etch of highly boron-doped p-type silicon in a 3:1 v:v solution of 48% aqueous hydrofluoric acid and ethanol in an electrochemical cell that exposed 1.2 cm^2 of the wafer to the electrolyte, as previously described.[19] A constant current density of 15 mA/cm^2 was applied for 9 min, using a 16 mm diameter ring-shaped Pt wire loop as the counter electrode. Subsequent to etching, samples were rinsed with ethanol and dried under a stream of dry nitrogen.

3.3.3 Chemical Modification of Porous Si Samples

The partially oxidized porous Si-SiO_2 films were prepared by thermal oxidation in tube furnace (Lindgerg Blue M) at 600 °C for 2 h in ambient air. Alkane-grafted porous Si surfaces were prepared by thermal hydrosilylation of the liquid-masked samples with neat 1-dodecene or a 10% (v/v) solution of 10-bromo-1-decene in mesitylene. Using standard Schlenk and syringe inert atmosphere handling methods,[118]

the samples were submerged in the alkene and degassed with 3 freeze-pump-thaw cycles prior to heating at 140 °C for 2 h in a nitrogen environment. The modified samples were then rinsed with acetone and ethanol to remove excess alkene.

3.3.4 Physical Characterization of Porous Silicon

3.3.4.1 Scanning Electron Microscopy

An FEI XL30 ultra-high resolution scanning electron microscope (SEM) operating at an accelerating voltage of 5 kV was used to obtain plan-view and cross-sectional images of the samples. Samples were not coated with metal or carbon prior to imaging, and low beam currents were used to avoid sample charging artifacts. Energy-dispersive X-ray spectroscopy (EDX) analysis was performed on plan-view and cross-sectional samples using a Philips XL-30 Field Emission ESEM with Oxford EDX attachment.

3.3.4.2 Infrared Spectroscopy

Attenuated total reflectance Fourier transform infrared (ATR-FTIR) spectra were acquired on a Thermo Scientific Nicolet 6700 FT-IR spectrometer with a Smart iTR accessory for ATR sampling. 128 scans were averaged. Spectral resolution was 4 cm^{-1} over the range 600-4000 cm^{-1}.

3.3.4.3 Water Contact Measurement

Water contact angle measurements were obtained by imaging water droplets placed on horizontally oriented porous Si samples using a Canon EOS XSi digital camera with 100 mm macro lens. Droplets of 5 μL deionized water were placed on the sample surfaces. The contact angle was measured from the acquired images using Adobe Photoshop CS4 (Adobe Systems, Inc.) Each reported contact angle represents the average of triplicate measurements at different locations on the porous Si surfaces.

3.3.5 Optical Reflectance Spectrum Acquisition and Analysis

The thin film interference spectra were obtained in a 180° reflectance configuration, collected using an Ocean Optics 4000 CCD spectrometer fitted with a bifurcated fiber optic cable. An unpolarized tungsten light source was focused onto the porous Si surface with a spot size of approximately 1 mm^2. Reference spectra were obtained from a broadband metallic mirror (model 10D20ER.2, 25.4 mm dia front-surface silver mirror on a Pyrex® glass support, Newport Corporation). Optical spectra were processed using a computer and algorithms described previously.[19]

3.3.6 Porosity and Fractional Filling Determined by Spectroscopic Liquid Infiltration Method (SLIM)

The SLIM method was used as described in the literature.[19] Briefly, two reflectance spectra of the porous Si film were obtained: (1) with the sample in air and (2) with the sample wetted with ethanol. The values of *2nL*, obtained from the Fourier

transform of the optical spectra, were fit to a two component Bruggeman model using the values of the refractive index of air and ethanol to determine the porosity and the thickness of the porous Si film. The thickness values determined in this fashion were validated on similar samples using cross-sectional SEM imaging. The fractional filling of water into the porous Si-SiO_2 layer was calculated with a similar optical measurement and model, using the thickness and porosity values previously determined from the SLIM measurements using pure ethanol as a filling liquid. The refractive index of all liquids used were independenly measured with a Mettler Toledo Refracto 30GS refractometer.

3.3.7 Loading and Release Study of Rhodamine B from Modified Porous Si Films

3.3.7.1 Loading of Rhodamine B

The organic dye rhodamine B was used as a test molecule for loading into the porous Si-SiO_2 matrix. The functionalized porous Si chip was immersed in 1 mL of 0.2 mg/mL rhodamine B in acetonitrile in a glass vial and agitated for 12 h at room temperature. The sample was then removed and rinsed with acetonitrile to eliminate excess free dye not loaded into the porous reservoir. To determine the loading efficiency, the loaded dye was extracted from the porous matrix by immersion in acetonitrile for 16 h at 37 °C with mild agitation. The quantity of rhodamine B released into solution was determined from the absorption spectrum, collected in the spectral range 400-650 nm using a SpectraMax absorbance spectrometer (Molecular Devices).

The concentration of rhodamine B was determined from calibration curves of the absorbance at 552 nm and assuming Beer's law.

3.3.7.2 Dye Release Studies

Porous Si-SiO_2 chips containing loaded dye were first dried in vacuum. Samples were then immersed in 1 mL of aqueous phosphate buffered saline (PBS) solution (pH 7.4) at 37 °C with mild agitation. The supernatant containing released dye was collected every 2 h over a 12 h period and replaced with 1 mL of fresh buffer. Concentrations of the released rhodamine B were determined from the absorbance at 552 nm, using calibration curves of the dye in PBS.

3.4 Results and Discussion

3.4.1 Selective Chemical Modification using Liquid Masking

The method for differential modification of the inner/outer surfaces of a porous Si layer is summarized in Figure 3.1. The as-formed (freshly etched) porous Si thin film (Figure 3.1A) contained hydride species throughout the inner and outer pore surfaces, as confirmed by Fourier transform infrared (FTIR) spectroscopy (Figure 3.2A): the spectrum displayed a small signal assigned to Si-H vibrations, at 2108 and 2084 cm^{-1} (ν_{SiH2} and ν_{SiH} stretching modes, respectively). Typical porous films consisted of pores of diameter 7 ± 2 nm and film thickness 6.1 ± 0.2 μm (by scanning electron microscopy, Figure 3.3), with a total open porosity of 47% (determined by the spectroscopic liquid infiltration method[119] assuming Si skeleton refractive index of

2.48). Mild thermal oxidation (600 °C in air for 2h, Figure 3.1B) removed the Si-H species, and yielded a thin layer of silicon oxide coating the entire nanostructured Si skeleton, both inside and outside the pores (FTIR spectrum, Figure 3.2B). The porosity of the film at this point decreased to 38% (determined by the spectroscopic liquid infiltration method[119] assuming porous Si-SiO_2 skeleton refractive index of 1.97). The film was then mounted in a Teflon cell, and a small quantity of octane was introduced to fill the porous nanostructure (Figure 3.1C). Although the oxidized surface imparts a hydrophilic nature to the material (sessile contact angle 10 ± 3°), it was found that octane, hexane, 1-octanol, and toluene could penetrate into the oxidized porous Si film. All these liquids were not easily displaced upon immersion in liquid water, with octane showing the best retention behavior. Optical interferometry indicated that less than 3% of the octane in the pores was exchanged by water after 60 min of immersion (Figure 3.4). Therefore, octane was used as the masking liquid for the subsequent experiments. Deionized water (2 mL) was added to the cell containing the octane-wetted porous Si film, and the excess octane was observed to float to the surface of the water due to its lower density (0.6986 g/cm^3, 25 °C) compared to water (0.9970 g/cm^3, 25 °C).[120] An aliquot of 1.55% by volume of aqueous (49%) HF in deionized water (2 mL) was then added to the cell (final HF concentration, 0.77%) and the sample was allowed to sit quiescently for 10 min (Figure 3.1D). The FTIR spectrum of a sample removed from the reaction at this point (Figure 3.2D) displayed bands associated with SiH_x species, at 2112 and 2087 cm^{-1}. It is noteworthy that, although the FTIR spectrum displayed a strong silicon oxide band (~1100 cm^{-1}), the Si-H stretching region of the spectrum

showed no evidence of $O_xSi\text{-}H_y$ species (silicon hydride stretching modes for silicon containing back-bonded oxygen atoms), which are expected to appear in the spectrum at 2160-2260 cm^{-1}. This is indicative of a demarcation between the Si-H and the SiO_2 surface regions of the porous $Si\text{-}SiO_2$ layer. The large increase in sessile contact angle to 102 ± 3° at this stage of the reaction is consistent with the presence of Si-H species on the outermost surface of the porous Si layer. Thus the mechanism of the reaction is assumed to involve reaction of HF with silicon oxide at or near the water/octane interface. HF is soluble in octane (20 mM at 25 °C),[121] so the length of time of exposure is expected to have an effect on the extent of diffusion of HF into the organic phase and thus the extent of reaction of HF with the Si-O surface. The expected products of the reaction are silicon fluoride and an Si-H terminated porous Si surface near the water/octane interface.[19]

The silicon hydride surface generated by the liquid masking procedure was then modified by thermal hydrosilylation (Figure 3.1E). Thermal hydrosilylation was performed using either 1-dodecene or 10-bromo-1-decene. In the case of 1-dodecene (Figure 3.2E), C-H stretching vibrations characteristic of the aliphatic organic chain were apparent in the FTIR spectrum at 2959, 2921, and 2852 cm^{-1}, assigned to asymmetric $–CH_3$, asymmetric $–CH_2–$, and symmetric $–CH_2–$ stretching modes, respectively. A control experiment in which the oxidized sample was subjected to thermal hydrosilylation conditions (without prior liquid masking/HF exposure) resulted in a sample whose FTIR spectrum displayed peaks at 2964, 2929, and 2857 cm^{-1} (Figure 3.5B). The relative intensity of the asymmetric $–CH_3$, band, and its observed shift to

higher frequency, is consistent with bonding of the organic species to the oxidized porous Si surface *via* an Si-OR motif rather than Si-R, as has been described previously.[122] To confirm this, the modified surface was exposed to dilute aqueous ethanolic HF. The FTIR data indicated that the organic species was completely removed from the Si-O surface (Figure 3.5D). By contrast, an oxidized sample that had been subjected to the liquid masking procedure and then hydrosilylated with 1-dodecene displayed a spectral pattern consistent with an Si-R bonding motif; this species was not removed upon exposure to dilute aqueous ethanolic HF (Figure 3.5E). Thus the liquid masking method generates reactive Si-H species which can be grafted to 1-alkenes *via* stable Si-C bonds. Without liquid masking, bonding of the 1-alkene occurs *via* either physisorption or formation of Si-O-C covalent bonds to the oxide surface, resulting in a surface modification that is less stable.[122]

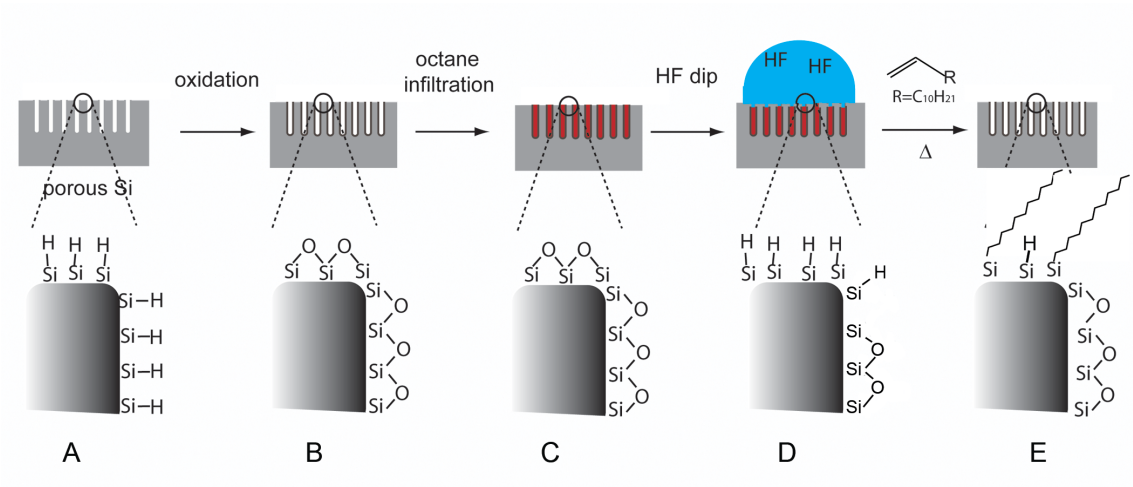

Figure 3.1 Schematic illustration of liquid masking method for selective chemical modification of porous Si films. (A) Freshly etched porous Si consists of a skeleton of crystalline silicon features with hydride species capping the skeleton surfaces. (B) Mild thermal oxidation removes the Si-H species and generates a thin layer of silicon oxide covering the silicon skeleton. (C) The porous Si-SiO_2 layer is then infiltrated with an inert organic liquid (octane). (D) Immersion of the octane-infiltrated sample in aqueous HF forms an immiscible interface that penetrates somewhat into the pores. Action of HF on the silicon oxide removes this oxide and places Si-H species on the outermost portion of the silicon skeleton. (E) Thermal hydrosilylation (140 °C) of the newly generated Si-H surface with 1-dodecene selectively replaces the Si-H species with alkenes, resulting in a spatially resolved surface modification.

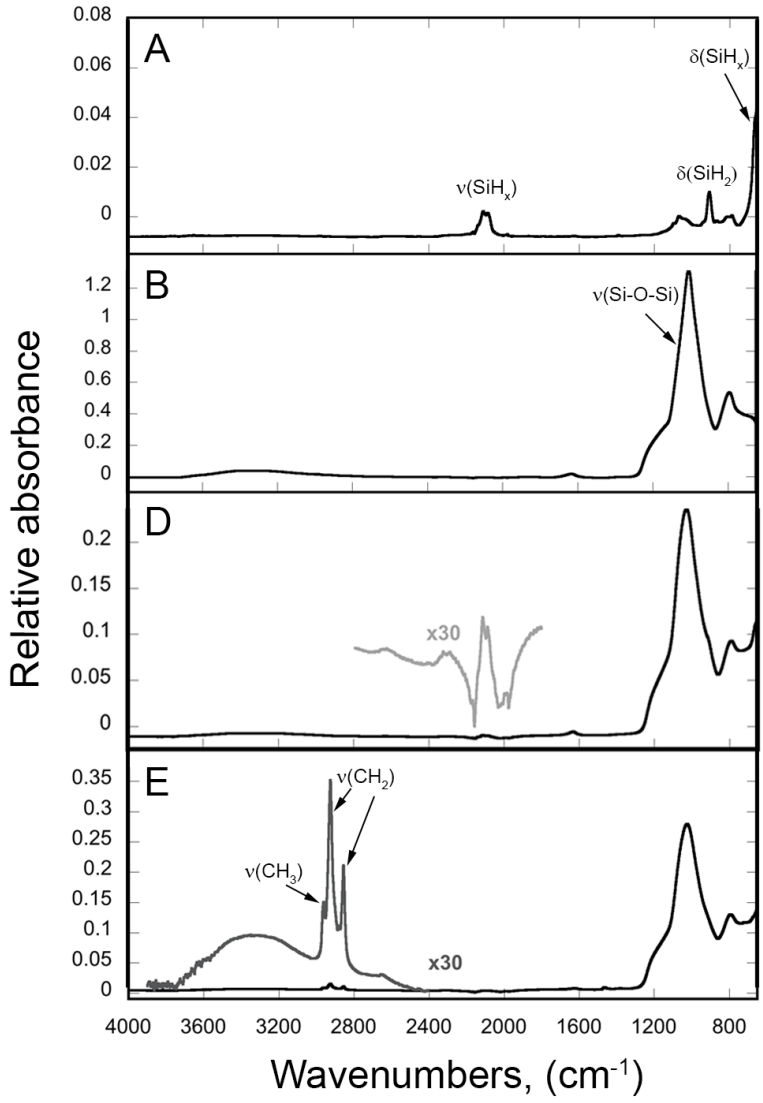

Figure 3.2 FTIR spectra of a porous Si sample at selected steps of the liquid masking procedure outlined in Figure 3.1. (A) freshly etched porous Si; (B) sample partially oxidized in air for 2h at 600 °C; (D) after infiltration with octane and exposure to aqueous HF (0.77%) for 600 s. Sample was rinsed and dried prior to acquisition of the spectrum; (E) after thermal hydrosilylation with 1-dodecene. The letter labels of the above spectra correspond to the stages described in Figure 3.1. Insets shown in (D) and (E) are expanded along the y-axis by 30 times.

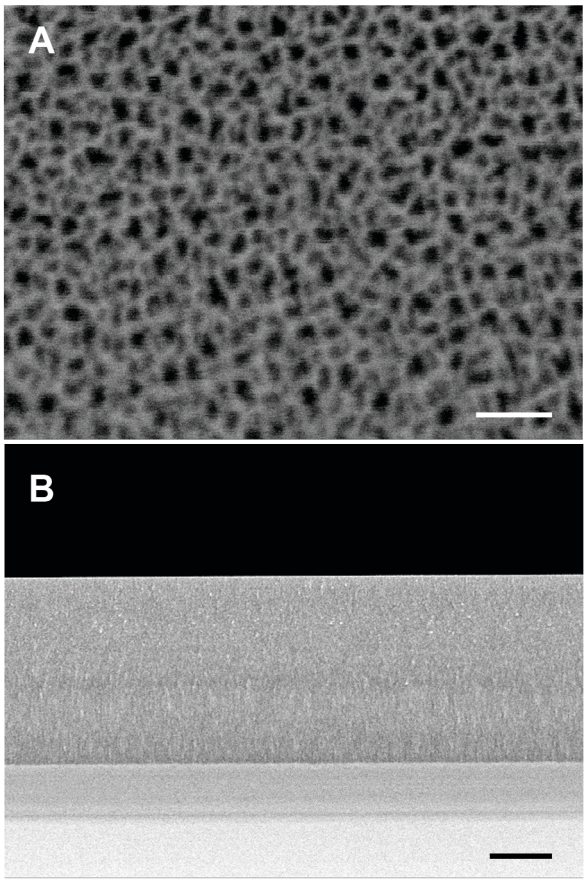

Figure 3.3 Scanning electron microscope (secondary electron) images obtained in (A) plan-view and (B) cross-section of freshly etched porous Si film typical of those used in this study. Scale bars are 50 nm and 2 μm, respectively.

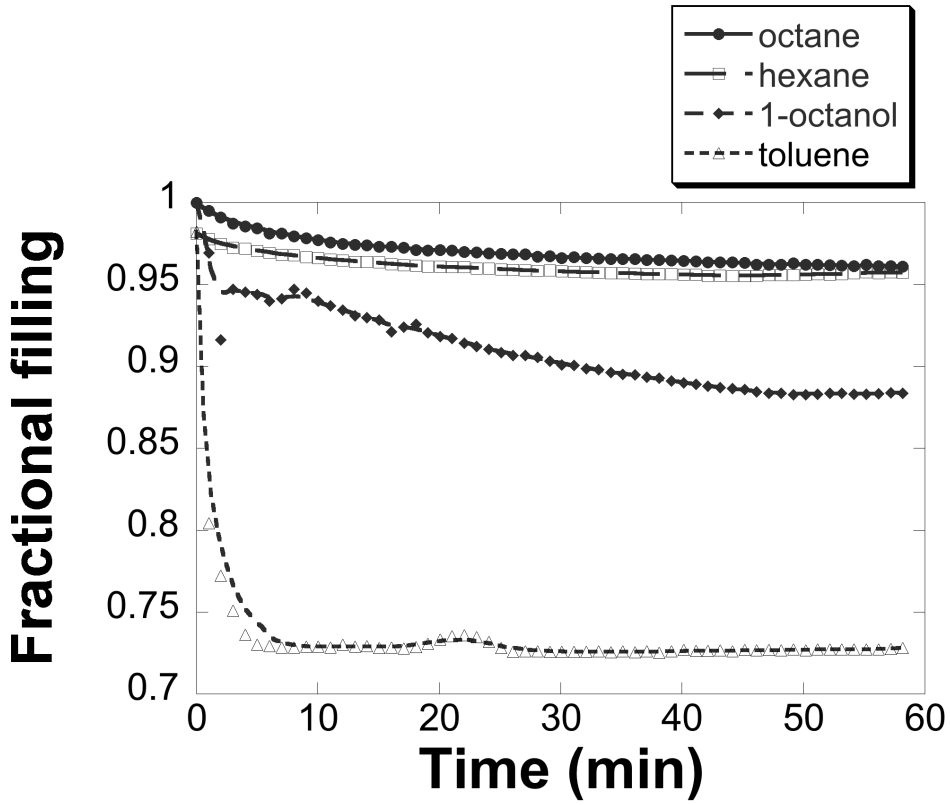

Figure 3.4 Optical measurement of the fractional filling of a partially oxidized porous Si-SiO_2 film containing the indicated organic liquids, as a function of time exposed to liquid water. A small aliquot of the organic liquid was first applied to the porous Si-SiO_2 film in the optical cell. The cell was then flooded with liquid water, and a series of optical reflectance spectra were acquired *in situ*. Values of *2nL*, obtained from the reflectance spectra as described in the text, were fit to a three-component Bruggeman effective medium model that included refractive index values of the porous Si-SiO_2 skeleton, the organic liquid, and water to determine the amount of organic liquid remaining in the pores during the course of the experiment. Data are presented as the fractional filling of the pores, defined as the fraction of the open pore volume that is filled with the organic liquid (the other fraction is assumed to be occupied by water as it infiltrates and displaces the organic layer). It is assumed that the organic and aqueous phases are completely immiscible, and that no mixing of the two liquids occurs. A fractional filling number of 1 indicates that 100% of the pore volume is filled with the organic liquid.

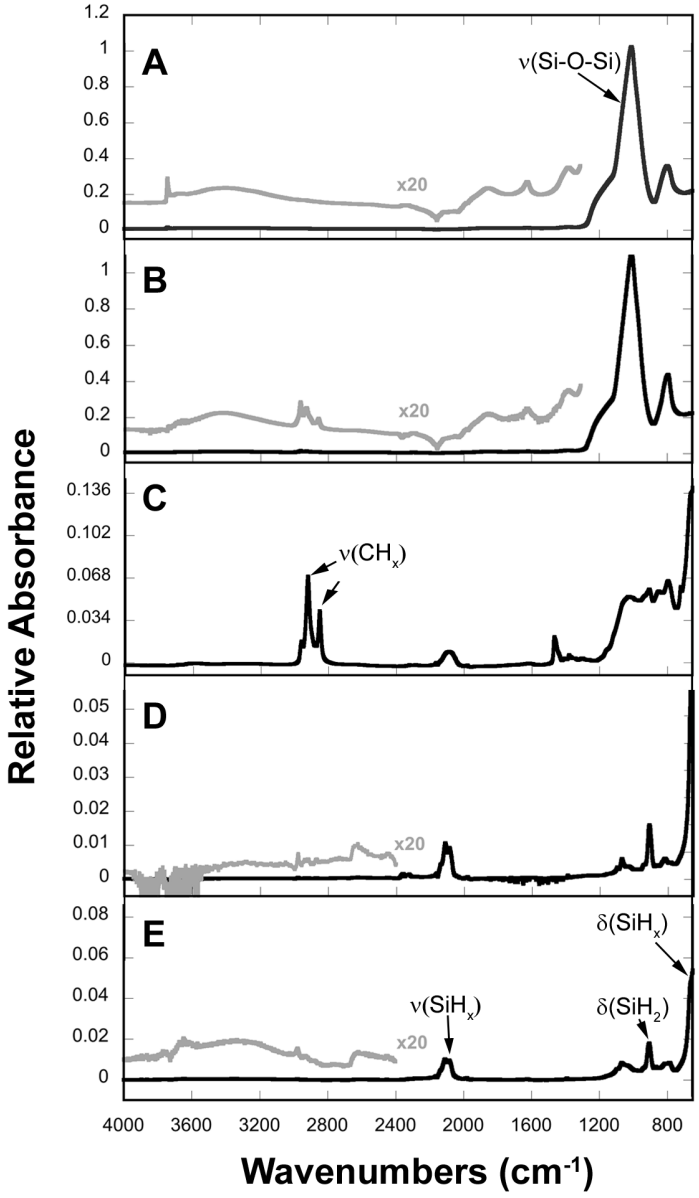

Figure 3.5 FTIR spectra of porous Si samples containing different chemical modifications used in this study. (A) Sample partially oxidized in air for 2h at 600 °C; (B) sample from control experiment in which partially oxidized porous Si was subjected to thermal hydrosilylation conditions with1-dodecene; (C) freshly etched porous Si sample after thermal hydrosilylation with 1-dodecene; (D) porous Si sample from (B) after exposure to dilute aqueous ethanolic HF, rinsing with ethanol and hexane, and then drying under a nitrogen stream; (E) dodecyl-terminated liquid masked sample after exposure to dilute aqueous ethanolic HF, rinsing with ethanol and hexane, and then drying under a nitrogen stream; (F) partially oxidized porous Si film after exposure to dilute aqueous ethanolic HF, rinsing with ethanol and hexane, and then drying under a nitrogen stream.

For the reaction of the surface oxide with HF represented in Figure 3.1D to proceed, the organic liquid used as the mask (octane) must allow the porous Si-SiO_2 layer to be exposed to the HF reactant, which is impeded due to the immiscibility of the aqueous HF solution with octane. Cross-sectional elemental mapping was used to determine the depth of penetration of the chemical reaction front, using energy dispersive X-ray spectroscopy (EDX) in the scanning electron microscope. To better resolve the depth of the reaction front, 10-bromo-1-decene was used in the hydrosilylation step instead of 1-dodecene. EDX elemental scans for Si, O, and Br were obtained from the top, middle and bottom portions of the porous Si-SiO_2 film, with a resolution of ~1 μm (Figure 3.6A and B). Confirmatory EDX spectra of 10-bromo-1-decyl-modified and thermally oxidized porous Si surfaces were obtained in plan view (Figure 3.6C and D). The EDX spectrum of the top 1 μm of porous Si from the air/porous Si interface, obtained from the cross-sectional image, revealed the presence of bromine and carbon peaks that can be attributed to grafted 10-bromo-1-decene. Bromine and carbon peaks were absent in the x-ray emission spectrum obtained from the bottom portion of the porous Si layer (near the porous Si/bulk silicon interface), suggesting that the attachment of 10-bromo-1-decene preferentially occurs near the top surface. The results are consistent with the proposed liquid masking mechanism, where reactive hydride species form in the topmost region of the porous layer. The resolution of the EDX method is not sufficient to obtain an accurate assessment of the thickness of 10-bromodecyl layer. The data from grafting of the bromo-dodecyl species supports the conclusion that hydrosilylation occurs only at the

surface of the liquid masked film. It should be pointed out that this substituted alkyl chain may also be useful to install more complex or larger molecules.

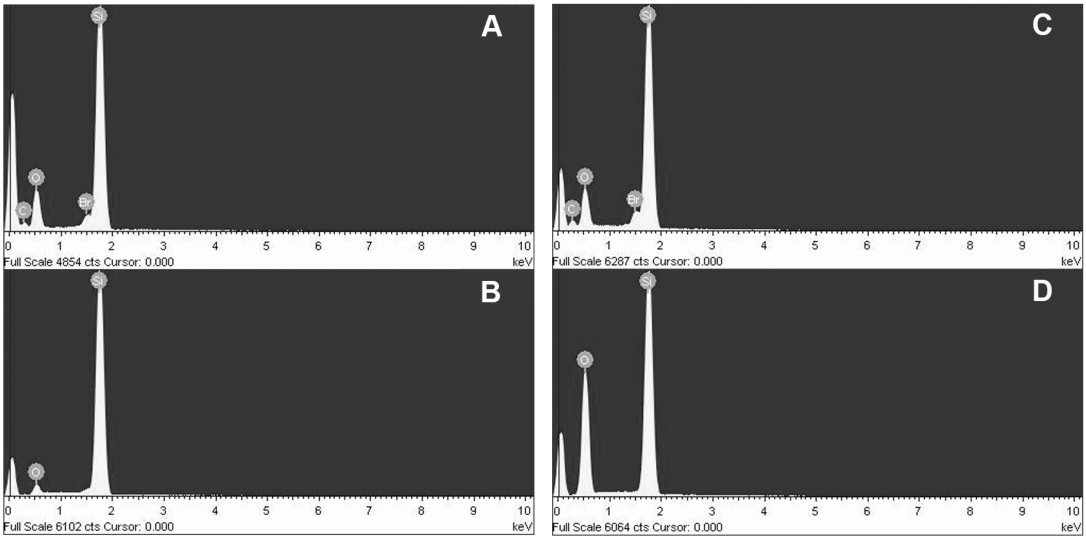

Figure 3.6 Elemental analysis (EDX spectra). (A) EDX spectrum obtained at the cross-section of the liquid masked porous Si film that was modified by hydrosilylation with 10-bromo-1-decene at a distance 1 μm from the top; (B) EDX spectrum obtained at the cross-section of the same modified porous Si film at a distance 1 μm from the bottom (i.e., 1 μm from the interface between the porous Si layer and the bulk silicon substrate). (C) EDX spectrum obtained from a 10-bromo-1-decyl-terminated porous Si at the plan view. (D) EDX spectrum obtained from a thermally oxidized porous Si sample at the plan view.

The chemical reaction between HF and the portion of the porous Si-SiO_2 film exposed by the liquid mask apparently propagates into the porous film at a rate sufficiently slow to allow temporal control of the degree of chemical modification, as discussed above. For this work, two different liquid masked sample types were prepared, along with three control sample types. Characteristics of the five sample types are summarized in Table 3.1. The first sample, Type 1, was a control sample consisting of the oxidized porous Si film with no further modification. Sample Type 2 was another control sample consisting of the oxidized porous Si film that was then subjected to the thermal hydrosilylation conditions with 1-dodecene. As discussed above, this sample type contains dodecyl species incorporated in the oxide layer. Sample Type 3 was a third control sample consisting of the freshly etched porous Si film (Si-H terminated) that was then subjected to thermal hydrosilylation with 1-dodecene. This sample type is thus fully infiltrated with dodecyl species grafted *via* Si-C bonds, and contains no liquid masked layer. Sample Types 4 and 5 were prepared following the procedure described in Figure 3.1D and Figure 3.7, where the time of exposure to $HF_{(aq)}$ was varied in order to control the extent of dodecyl modification in the barrier layer. The surface layer of Si-H species formed by liquid mask on either of these sample types was then modified by hydrosilylation with 1-dodecene (step E in Figure 3.1).[111] Sample Type 4 was less extensively modified, and displayed a contact angle significantly lower than sample Type 5. Both sample Types 4 and 5 are expected to contain a lower oxide layer with properties similar to control sample Type 2. Table 1 compares contact angles measured on the different sample types. Sample Type 1 was

not exposed to aqueous HF (time point 0 in Figure 3.7), and this oxidized porous Si surface was quite hydrophilic. The contact angle increased significantly with HF exposure times between 0 and 300s and then leveled off for times >300s (Figure 3.7), indicating that the extent of the reaction that forms hydride species can be readily controlled. Extending the aqueous HF exposure time of the octane-infiltrated porous Si film to 10 min yielded, upon subsequent thermal hydrosilylation with alkene, a very hydrophobic top surface with contact angle 118 ± 3° (sample Type 5).

Table 3.1 Summary of Sample Types Used in Rhodamine B Release Studies

Sample Type	Contact angle, degrees	Dye loading, μg/mg[a]
1: No barrier, oxide layer	10 ± 3	81.6 ± 8.9
2: No barrier, dodecyl hydrosilylated oxide layer	43 ± 4	75.1 ± 7.0
3: No barrier, dodecyl hydrosilylated Si-H layer	119 ± 2	13.3 ± 2.3
4: Low dodecyl coverage layer on hydrosilylated oxide layer	86 ± 5	40.5 ± 6.4
5: High dodecyl coverage layer on hydrosilylated oxide layer	118 ± 3	16.8 ± 1.9

[a]Dye loading quantified as micrograms of rhodamine B per milligram of porous Si layer. Dye was loaded from acetonitrile solution. Sample Types 4 and 5 were prepared by liquid masking as described in the text.

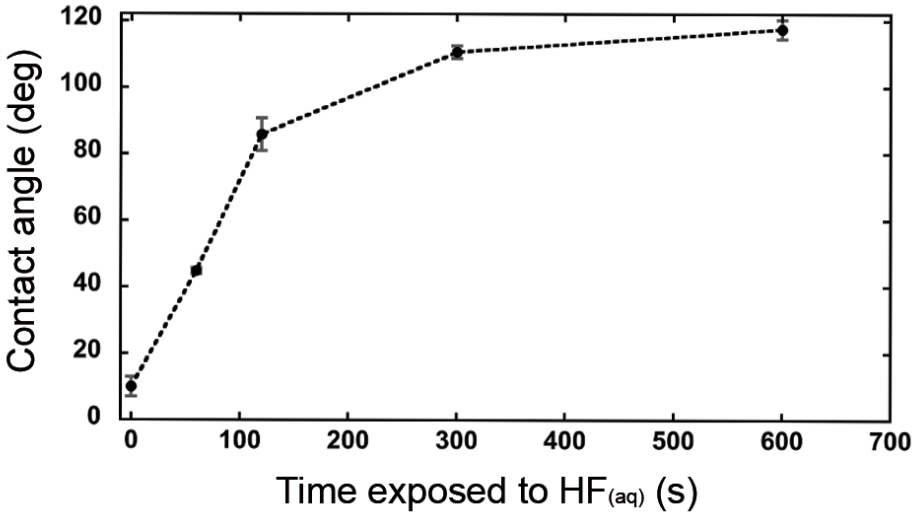

Figure 3.7 Measured sessile contact angle of 1-dodecyl-modified liquid masked porous Si samples as a function of time of exposure of the octane-masked film to aqueous HF. The liquid (octane) masked film was exposed to 0.77% aqueous HF (as indicated in Figure 3.1D) for the indicated time, and the resulting Si-H surface layer was subsequently modified by thermal hydrosilylation of 1-dodecene as indicated in Figure 3.1E. Time points at 120 s and 600 s correspond to the exposure times used to prepare liquid masked sample Types 4 and 5, respectively. Triplicate measurements; error bars indicate one standard deviation.

3.4.2 Monitoring of Liquid Transport through Dodecyl-modified Porous Si Samples

Despite the strong hydrophobic nature of the topmost, dodecyl-modified layer of the porous Si film generated by the liquid masking method, the EDX analysis (Figure 3.6) showed that the lower portion of the porous Si film remained oxidized. Thus the structures are somewhat reminiscent of an inverse micelle, consisting of a hydrophobic film coating an inner hydrophilic core.[123] Unlike a micelle, the structures formed by liquid masking are rigid, and they can be probed by optical interferometry. Lipid-coated porous Si films have been prepared previously, where a lipid bilayer was physisorbed to a rigid, oxidized porous Si film.[124-127] In those structures, the lipid layer was mobile and it often displayed pinholes and discontinuities.[128] In the present system, the hydrophobic dodecene layer was covalently grafted to the porous Si layer, and it apparently formed a uniform, continuous coating. We probed the transport of water across this dodecyl-modified porous Si surface layer and into the underlying hydrophilic porous Si-SiO_2 layer using optical interferometry. A CCD-based spectrometer and white light source were coupled to the optics *via* a bifurcated optical fiber that allowed acquisition of optical reflectance spectra at a time resolution of 1 sec. Reflective interferometric Fourier transform spectroscopy (RIFTS)[28] was employed, which quantified the appearance of water in the underlying porous Si layer as a shift in its optical thickness due to an increase in the average refractive index of the porous layer as air filling the pores was displaced by water.

The optical reflectance spectrum of a dodecyl-modified sample in air (Figure 3.8A) displays Fabry-Pérot interference fringes, corresponding to constructive and destructive interference from light reflected at the air/porous Si and porous Si/crystalline Si interfaces.[90] The peak maximum for each of the spectral fringes follows the Fabry-Pérot interference relationship represented by Equation 3.1 in normal incidence:

$$m\lambda = 2nL \qquad (3.1)$$

where m is the spectral order of the fringe at wavelength λ, n is the average refractive index of the porous layer and its contents, and L is the physical thickness of the film. The liquid masked layer in the top portion of the film did not display sufficient refractive index contrast to be distinguished from the underlying oxidized layer in the interference spectrum, and so the contents of the entire layer are probed as an average in this experiment. In the RIFTS method,[19] the fast Fourier transform (FFT) of the frequency spectrum (inset, Figure 3.8A) yields a peak whose position along the x-axis represents the value of the effective optical thickness (EOT), or $2nL$, from Equation 3.1.

The optical measurement conveniently monitors the infiltration of water into the porous Si-SiO_2 layer in real time. The samples were mounted in a sealed cell fitted with the optical microscope/spectrometer focused on a ~1 mm spot on the porous Si sample. The spectral data from a control experiment, performed on a porous Si-SiO_2 film that had not been subjected to the liquid masking procedure (represented by step B in Figure 3.1) is shown in Figure 3.8B. Introduction of water to the sample chamber resulted in an instantaneous increase in the value of $2nL$ measured from the sample, as the liquid

water replaced the air in the 38% porous film. Using the thickness of the porous Si film measurerd by SEM and the refractive index of air (n_D=1.00) and water (n_D=1.3330) at 20 °C,[120] a fit to the Bruggeman effective medium model[91, 92] was used to determine the fractional filling of the porous volume occupied by the infiltrated liquid. A fractional filling value of 1.0 was observed, indicating full infiltration of water in this sample.

The experimental protocol followed in the water infiltration experiments involved addition of a small quantity of ethanol to the sample cell several seconds after water was introduced. The purpose of the ethanol addition was twofold: (1) ethanol reduces the surface tension of water and thus allows it to more thoroughly wet the nanometer scale pores in the film; and (2) the larger refractive index of ethanol (n=1.3336) introduces a secondary increase in the value of *2nL*. Both of these factors provide verification of the fraction of the porous film that has been infiltrated by water. In the case of the control sample consisting of porous Si-SiO_2 with no hydrophobic barrier layer (Figure 3.8B), ethanol addition resulted in an increase in *2nL* that fit the calculated prediction for a fully infiltrated layer.

The presence of the thin hydrophobic layer on the top portion of the film dramatically changes its behavior with water. As the contact angle measurements demonstrate, the dodecyl-terminated layer is quite hydrophobic, and it was found to effectively exclude water from the underlying porous Si-SiO_2 layer. Addition of water to the optical cell resulted in a fractional filling of only 0.08 with this sample (Figure 3.8C). When ethanol was added to the water, rapid penetration of the hydrophobic layer was observed, and complete infiltration of the porous Si-SiO_2 layer occurred

within 4 sec. In the data shown in Figure 3.8C, the sample was stable, with no additional water infiltration observed, for 20 sec prior to ethanol addition. In separate experiments (not shown), it was found that pure water penetrated the hydrophobic barrier layer very slowly. We conclude that the presence of the hydrophobic barrier layer effectively impedes the penetration of water molecules into the pores.

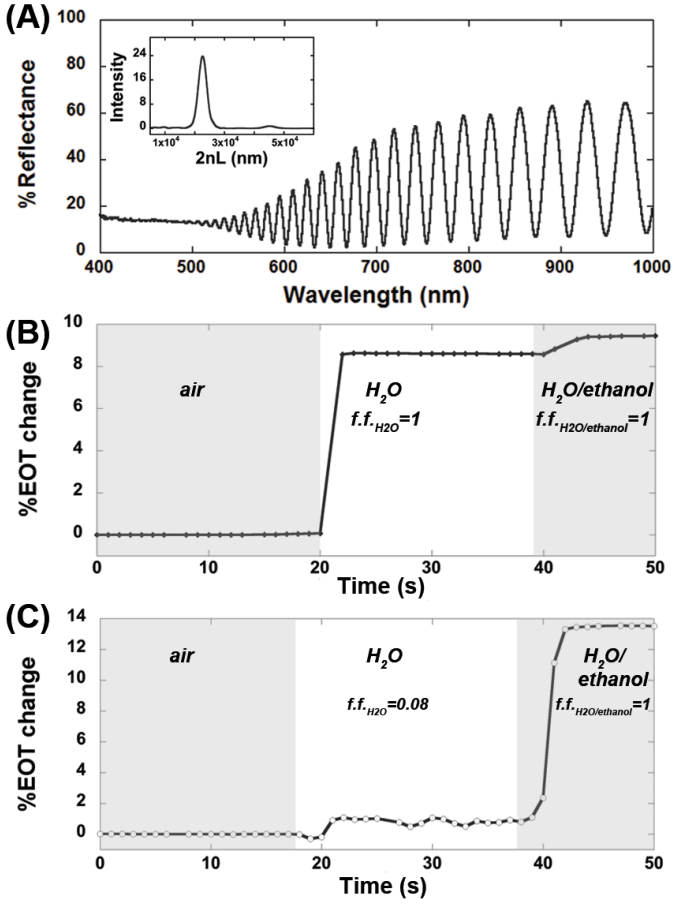

Figure 3.8 Experimental optical response vs. time data showing the penetration of liquid water (n_D = 1.333) or a 1:1 water/ethanol (equal volume) solution (n_D = 1.3598), as indicated, through a hydrophobic dodecyl barrier layer grafted to the top portion of a partially oxidized porous Si-SiO_2 film. The barrier layer was prepared by the liquid masking method described in Scheme 1, and water infiltration to the partially oxidized porous Si-SiO_2 film was quantified by reflective interferometric Fourier transform spectroscopy (RIFTS). (A) Optical reflectance spectrum of a typical sample prepared by liquid masking. Sample consists of ~6 μm-thick surface-oxidized, hydrophilic porous Si-SiO_2 layer underneath a dodecyl-terminated, hydrophobic layer. Inset shows the FFT of the frequency spectrum; the peak position yields the value of *2nL* (the effective optical thickness) of the film. (B) The quantity *2nL* measured as a function of time during water infiltration into a control sample consisting of partially oxidized porous Si, without the hydrophobic barrier layer. The terms "f.f.$_{liquid}$" refer to the fractional filling of the indicated liquid in the porous layer in the indicated temporal region of the curve. (C) The quantity *2nL* measured as a function of time during water infiltration into a sample containing a dodecyl barrier layer. Contact angle of barrier layer in this experiment was 118 ± 3°.

3.4.3 Controlled Release of Small Molecules through the Dodecyl Barrier Layer

The ability of the hydrophobic barrier layer to exclude and impede the transport of water has interesting implications for controlled release drug delivery. Since the first reports of the bioactivity of porous Si in 1995,[129] porous Si has been widely studied as a potential drug delivery material.[11, 12, 130] To test the ability of water soluble molecules to escape through the dodecyl barrier layer, rhodamine B was loaded into the oxidized layer by physical adsorption from an acetonitrile solution. The mass of rhodamine B loaded into the porous Si samples was confirmed by absorbance spectroscopy. Acetonitrile was chosen as the loading and extraction solvent due to the hydrophobic nature of the modified samples. The loading efficiencies for rhodamine B in the five sample types are given in Table 3.1. The general trend that can be seen in the data of Table 3.1 is that the greater the hydrophobicity of the sample, the lower the quantity of hydrophilic dye that can be loaded. The more extensively dodecyl modified sample Type 5 was found to load less dye per mg of porous Si than the less extensively modified sample Type 4. The control sample Type 3, consisting of a fully dodecyl-terminated layer, held an amount of dye similar to the extensively dodecyl modified sample Type 5. The oxidized but un-modified sample Type 1 held the most dye of all the samples. The Type 1 sample was the most hydrophilic of the samples, and so its high loading capacity is consistent with the hydrophilic nature of rhodamine B molecules.[131] The control sample Type 2, consisting of an oxide layer that had been made partially hydrophobic by incorporation of dodecyl species but with no barrier

layer, showed loading capacity similar to, but slightly less than the Type 1 oxide layer. This Type 2 sample contained more dye than either of the "barrier layer" samples (Types 4 and 5).

The rate of release of the rhodamine B test molecule is also reduced in the more hydrophobic sample types. In order to test the dye release characteristics, the samples were immersed in a phosphate buffered saline (PBS, pH = 7.4) solution and the appearance of the dye in solution was monitored by absorbance spectroscopy for a 12 h-period (Figure 3.9). Due to the low wettability of the hydrophobic dodecyl barrier layer, transport of dye from the partially oxidized reservoir layer into aqueous solution is expected to be impeded, as the aqueous medium does not easily penetrate the pores. As shown in Figure 3.9, egress of rhodamine B from the Type 1 samples (hydrophilic oxide with no barrier layer) displayed a typical burst release characteristic, with 100% of the loaded molecule released into solution within 12 h. The samples containing the dodecyl modified oxide layer all showed somewhat slower release characteristics. The control sample Type 2, containing no barrier layer with a dodecyl-modified oxide, released only 70% of the loaded rhodamine B within 12 h. The sample Type 4, containing the minor barrier layer over a dodecyl-modified oxide, displayed a somewhat lower rate of release; only 60% of the dye was released within 12 h. The sample Type 5, containing the most extensive dodecyl barrier layer, exhibited a significantly lower rate of release, with only 20% of the dye released in the 12 h study period. Control sample Type 3, containing a fully dodecyl-terminated surface, displayed the slowest release, with only 1% of the dye released in 12h. As expected from its highly

hydrophobic nature, this sample type also displayed a very low capacity for the hydrophilic dye. The control experiments (sample Types 2 and 3) described above establish the limiting capacity and transport rates of the hydrophilic and hydrophobic surface types that are generated by the liquid masking procedure. In particular, the control experiment where there is no barrier layer and just the hydrosilylated oxide "reservoir" layer (Sample Type 2) establishes the intrinsic release rate and loading numbers for the barrier-free film (rapid release, high loading capacity). Similarly, Sample Type 3, which contains only a hydrosilylated Si-H surface, establishes the intrinsic release and loading characteristics of the hydrophobic barrier layer (slow release, low loading capacity). The dye release rates and loading capacities of the liquid masked samples fall between these two limits, demonstrating the ability of the liquid masking procedure to provide control over these parameters.

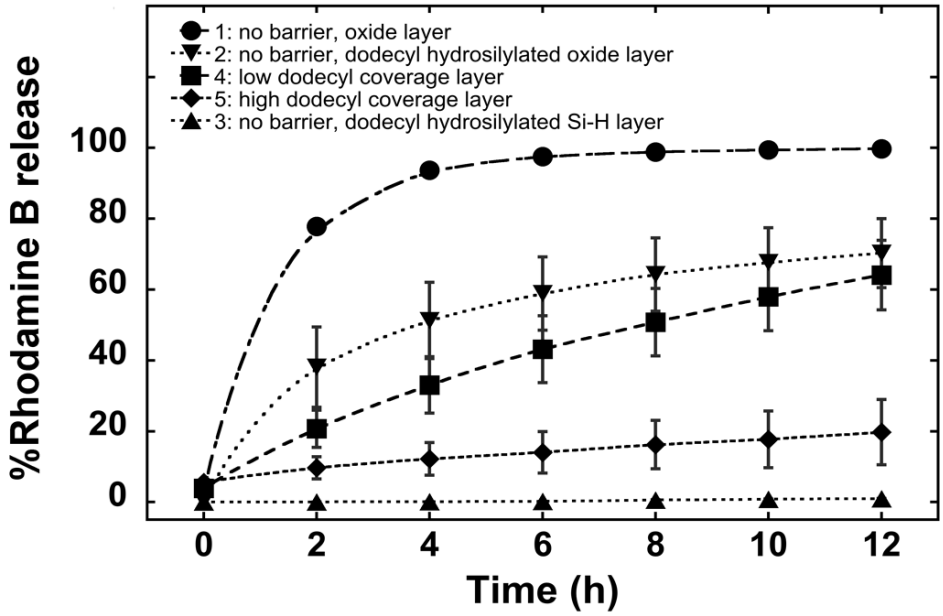

Figure 3.9 Release profiles of rhodamine B into aqueous PBS buffer from partially oxidized porous Si layers containing different top barrier layers and interior surface chemistries: (●) sample Type 1, porous Si/SiO_2 layer with no barrier layer (sample not subjected to liquid masking procedure); (▼) sample Type 2, porous Si/SiO_2 layer subjected to hydrosilylation conditions but containing no liquid masked barrier layer; (■) sample Type 4, porous Si/SiO_2 layer subjected to liquid masking procedure, with low dodecyl coverage in top barrier layer (♦) sample Type 5, porous Si/SiO_2 layer subjected to liquid masking procedure, with high dodecyl coverage in top barrier layer; (▲) sample Type 3, freshly etched porous Si hydrosilylated with 1-dodecene throughout the layer. Each data point in the curves was averaged from three samples and the error bars indicate standard deviation.

This study focused on chip-based films, that is, porous layers still attached to a silicon wafer. However, the liquid masking method reported here may also be useful to prepare micro- or nanoparticles as carriers for drugs or other molecules. The preparation of micro[51] and nanoparticles[132] from porous Si has been described, as has their use as *in vivo* drug delivery materials.[133-138] A key feature of the approach is it provides a simple means to harness the chemistry of porous Si to place a thin hydrophobic barrier layer over a hydrophilic reservoir layer. Alternate chemistries, where the inner reservoir layer of the material is hydrophobic and the exterior is hydrophilic, should also be possible with this approach.[51] With the present formulation, the slowing of release of a highly water-soluble molecule was demonstrated; as observed in the control experiments, this is difficult to achieve without the hydrophobic barrier layer. The oxidized inner pores can potentially accommodate a wide range of molecules, including larger proteins. It has previously been shown that the relatively large pore dimensions (>20 nm) accessible in the porous Si system and the biodegradable oxide surface allow loading of antibodies with little loss of activity upon release.[32] The inert nature of the oxidized surface may also be more compatible with redox-active drugs, compared to the native Si-H surface present in freshly etched or hydrosilylated porous Si.[35]

3.5 Conclusions

The data demonstrate that the liquid masking approach can prepare Janus-type porous Si nanostructures with controllable hydrophobicity/hydrophilicity

characteristics. The layers formed by liquid masking modify the loading capacity and diffusional properties of the porous nanostructures; in this work the potential utility of such materials was demonstrated with a notional controlled drug release experiment using a hydrophilic test molecule, rhodamine B. The presence of octane (the liquid mask) within the oxidized porous nanostructure controlled the diffusion of the aqueous HF developer into the porous nanostructure, which provided control over the surface coverage and depth of penetration of the silicon hydride species available for subsequent modification. Thermal hydrosilylation conditions (using dodecene) modifies both the silicon hydride species at the outer layer and (to a lesser extent) the oxidized silicon surface in the inner layer of the porous Si/SiO_2 film; the resulting hydrophobic outer layer displayed contact angles ranging from 86° to 118°, depending on the length of time the liquid masked layer was exposed to the aqueous HF developer. The outer hydrophobic surface acted as a barrier for water infiltration that was monitored using optical interferometry. One application of this hydrophobic barrier layer was demonstrated for controlled release of small molecules, and the data show that the variable degree of modification afforded by the liquid masking method allows the control of the rate of release of a hydrophilic molecular payload (rhodamine B). It was found that the loading capacity and the rate of release of the hydrophilic dye depended on the degree of hydrophobic modification of the porous Si sample: the greater the hydrophobicity, the lower the capacity and the lower the rate of release. Thus the liquid masking method should provide an ability to fine-tune the delivery of drugs from porous Si films or particles.

Chapter three, in part, is a reprint (with co-author permission) of the material as it appears in the following publication: Wu, C.; Sailor, M. J., Selective Functionalization of the Internal and the External Surfaces of Mesoporous Silicon by Liquid Masking. *ACS Nano,* **2013**, 7, 3158-3167. The author of this dissertation is the primary author of this manuscript.

CHAPTER FOUR

INTERACTION OF POROUS SI PARTICLES WITH BIOLOGICAL SURFACES OF NEMATODES

4.1 Abstract

The interaction of nano- and micro-particles of mesoporous silicon (pSi) of sizes 0.4 ± 0.2 and 5.3 ± 2.0 microns containing an anthelmintic pore-forming toxin with nematodes is assessed. Thermally oxidized pSi particles are stable and show relatively low toxicity to nematodes. Fluorescence imaging of rhodamine-labeled pSi particles within the nematodes *Caenorhabditid elegans (C. elegans)* and *Ancylostoma ceylanicum (A. ceylanicum)* is used to monitor particle ingestion behavior. The ingestion of pSi particles to the worms is found to be dependent on size; particles of size 0.4 ± 0.2 micron are noticeably ingested by both species within 2 h of introduction *in vitro* while 5.3 ± 2.0 micron particles are excluded from *C. elegans* and enter pharynx region of *A. ceylanicum* after 24 h. Fluorescence imaging indicated that all particle types are primarily restricted to the pharynx region after ingestion. Incorporation of the anthelmintic drug Cry5B significantly improves bioavailability and stability of this water insoluble and hydrolytically unstable compound *in vitro*. Cry5B-containing particles show significant degradation of worm viability and motility *in vitro*. Particles of size 0.4 microns display the highest level of *in vitro* toxicity toward *C. elegans* on a drug mass basis. The porous drug carrier also protects Cry5B from hydrolytic and enzymatic (pepsin) degradation in simulated gastric fluid (pH = 1.2) for periods of up to 2 h. *In vivo* experiments with hookworm-infected hamsters showed no significant reduction in worm burden with the Cry5B-loaded particles relative to free drug, which is attributed to the limited quantity of drug released from the particles due to its short residence time in the animal.

4.2 Introduction

Interactions of synthetic inorganic particulates with nematodes are of great interest for the evaluation of environmental toxicity on nanoparticles with multicellular organisms. Toxicity of oxide nanoparticles has been assessed on *Caenorhabditid elegans (C. elegans),* and the particles effect on life span, stress level, and the progeny production varies on material composition, shape, surface chemistry, physical dimension, and concentration applied.[139-141] Understanding the interaction of nanomaterials with nematodes not only provide information on environmental toxicity assessment but also aid on rational design of nanomaterials as drug delivery carriers for the treatment of parasitic diseases.

Mesoporous silicon particles prepared from electrochemical etching with suitable surface modification is compatible with a wide range of protein and other biomolecule payloads.[12, 32, 62, 142-145] Porous Si (pSi) particles show good chemical stability, large pore size and capacity for loading of relatively large proteins, its biodegradability[146, 147] and biocompatibility,[148-150] all of which establish pSi a candidate for drug delivery applications.[12, 151] Oral delivery of therapeutics remain an attractive delivery route for its high patient compliance and ease of application. *In vitro* cytotoxicity of pSi particles on epithelial cell models was shown to be varied by particle concentration, surface chemistry and physical sizes.[65, 152] Oral delivery of peptides using pSi-based microcarriers have recently reported to enhance paracellular delivery of insulin across intestinal Caco-2 cell membranes *in vitro*[153] and to prolong therapeutic

effect of a ghrelin antagonist *in vivo*.[66] Studies on the biodistribution of pSi particles through enteral and parenteral administrations in rats show little internalization in the cells.[154] Particulate parameters such as size, charge, shape, and surface chemistry have been shown to have an effect on the passive transportation through the mucosal layer. Thermal oxidation chemistries have shown to stabilize the Si surface and reduce production of reactive oxygen species from the freshly etched porous Si.[155] Micro- and nano-sized thermally oxidized pSi particles were previously reported to demonstrate low cellular toxicity by the assessment of the cell viability, oxidative stress, inflammation and responses from Caco-2 cell models and RAW 264.7 macrophages.[152] The oxide surface not only proved to be compatible with proteins, the negatively charged surface is advantageous to concentrate proteins in the pores *via* electrostatic forces.[32] Various forms of oxidized pSi particles demonstrate stability in acidic conditions and readily dissolve at pH >7.[64] Dissolution of the nanostructure results in orthosilicate ions, the bioavailable form of silicon naturally found in the body.[147]

Crystal (Cry) proteins made by the bacterium *Bacillus thuringiensis* (Bt) are pore-forming toxins that specifically target insects and have been used worldwide in transgenic crops as pest control for caterpillars and beetles.[156] To access the target tissue, the Bt crystal protein has to first be ingested by an insect, Cry toxins are then solubilized in gut juice, proteolytically activated by midgut proteases and bind to midgut receptors, leading to pore formation and eventually death.[157, 158] Among Bt crystal proteins, Cry5B has been characterized as a nematocidal toxin and has been demonstrated its efficacy on *C. elegans,*[159] *Heligmosomoides bakeri,*[160] *Ascaris suum*[161] and *Ancylostoma ceylanicum (A. ceylanicum).*[162, 163] *C. elegans* is a simple

multicellular eukaryote whose development process is well characterized and have been developed for ecological risk assessment in soil[164] and water.[165] Being sensitive to the majority of anthelmintic drugs that are used against parasitic worm infections of human and livestock, *C. elegans* serves as a good model for *in vitro* evaluation of anthelmintic delivery.[166] *A. ceylanicum*, a hamster hookworm that can be used as a model for the prevalent human hookworm *A. duodenate*,[167] a major global health problem and principle among a number of soil-transmitted helminth (STHs) is chosen for *in vitro* and *in vivo* study as target parasitic worms. In this paper, we characterize the interactions of pSi particles with *C. elegans* and *A. ceylanicum* and evaluate the feasibility of using thermally oxidized pSi particles of different particle sizes as delivery vehicles for therapies against parasitic infections.

4.3 Experimental Methods

4.3.1 Chemical and Materials

(100)-oriented, boron-doped 0.9-1.0 mΩ-cm resistivity p-type silicon wafers were obtained from Siltronix, Inc. Absolute ethanol (200 proof) was obtained from Rossville Gold Shield Chemicals. Hydrofluoric acid (48% aqueous, ACS grade) was obtained from Macron Chemicals, Fisher Scientific. Sucrose (crystalline, certified ACS) was obtained from Fisher Chemical. 5-(and 6)-carboxytetramethylrhodamine succinimidyl ester (NHS-rhodamine), 1-Ethyl-3-(3-dimethylaminopropyl)carbodiimide hydrochloride (EDC), and bicinchoninic acid (BCA) protein assay reagent were obtained from Thermo Scientific. Pepsin from porcine gastric mucosa (lyophilized

powder, 3200-4500 units/mg protein), sodium azide (≥99.5%) and 3-aminopropyltrimethoxysilane (97%) were obtained from Sigma-Aldrich. Sodium hydroxide solution (1.0 N) was obtained from EMD Millipore Chemicals. Recipes for culturing medium special S medium, M9 medium and hookworm culture medium were followed in previous described methods.[162, 168]

4.3.2 Preparation of Porous Si Particles

PSi particles were prepared by anodic electrochemical etch of highly boron-doped p-type silicon (0.97 mΩ–cm resistivity) in a 1:1 v:v solution of 48% aqueous hydrofluoric acid and ethanol (CAUTION:HF is highly toxic and contact with skin should be avoided) in an Teflon cell that exposed 8.04 cm^2 of the wafer to the electrolyte, as previously described.[19] A constant current density of 50 mA/cm^2 between 20 s to 240 s was used in electrochemical etching to generate pSi film of thickness 0.4 μm and 5.0 μm, with a 28 mm diameter spiral-shaped platinum wire loop as the counter electrode. To produce pSi particles with narrow size distributions and high yields, a 'perforated' electrochemical etch was adapted using high current density pulses (200 mA/cm^2, 0.5 s) to induce mechanical stress points that can be easily fractured during ultrasonic.[154] These high-porosity layers with mechanically induced stress points predetermine the particle size and increase synthetic yields. The perforated porous film was then removed from the substrate by electropolishing in a 3.33% HF in ethanol solution for 60 s at a constant current density of 5.0 mA/cm^2. Subsequent to etching, wafers were rinsed with ethanol and dried under a stream of dry nitrogen. The

etching and electropolishing procedure was repeated at ~40 μm steps and total thickness of the pSi films were ~300 μm. The resulting porous films were placed in absolute ethanol and fractured into particles by ultrasonication for at least 20 h. Particles were rinsed with ethanol and centrifuged at 5000 rpm for 5 min for collection of 5.0 μm pSi microparticles and 11000 rpm for 20 min for collection of 0.4 μm pSi nanoparticles.

4.3.3 Chemical Modification of Porous Si Particles

The partially oxidized pSi particles were prepared by thermal oxidation in a muffle furnace (Model FD1545M, Thermo Scientific Inc.) at 400 °C for 1 h in ambient air. Conjugation of rhodamine dye to the thermally oxidized pSi particles was followed from previously described method.[169] A 1.0 mL of 1 M hydrochloride solution was added to 1.0 mg of partially oxidized pSi particles and shaken for 10 min to activate the surface with hydroxyl terminus; the particles were then washed with deionized water and ethanol three times of each. A 400 μL aliquot of 1.0% 3-aminopropyltrimethoxysilane in ethanol was added to the particles and shaken for 1 h. The particles were then washed with ethanol three times and suspended in 500 μL ethanol. Next, 10 μL of 2 mg/mL NHS-rhodamine in water and 50 μL of 10 mg/mL EDC in water were added to the particles, and the mixture was allowed to react for 16 h with constant shaking. The rhodamine-labeled pSi particles were then washed with ethanol and deionized water three times of each prior exposed to nematodes.

4.3.4 *In vitro C. elegans* Bioactivity Assays

C. elegans strain Bristol N2 was used in the study. Worms were maintained according to standard procedures.[170] Biocompatibility of pSi particles on *C. elegans* mortality assays (triplicate wells per trial and two independent trials) and bioactivity of Cry5B loaded pSi particles (triplicate wells per trial and three independent trials) were carried out as previously described.[171] At day 6, the mortality of *C. elegans* was scored for dead worms by absence of reaction upon gentle pokes. Each experiment was performed in wells containing 15 to 30 worms per well.

4.3.5 *In vitro* and *In vivo A. ceylanicum* Bioactivity Experiments

A. ceylanicum hookworms were maintained in golden Syrian hamsters.[163] *In vitro* bioactivity assays on adult *A. ceylanicum* were carried out and scored with motility index as previous described where 3 represents vigorous active as control and 0 as death.[172] All animal experiments were performed under protocols approved by the UCSD Institutional Animal Care and Use Committees (IACUC). All housing and care laboratory animals used in this study conform to the NIH Guide for the Care and Use of Laboratory Animals in Research (see 180F22) and all requirements and regulations issued by the USDA, including regulations implementing the Animal Welfare Act (P.L. 89-544) as amended (see 18-F23). The bioactivity of Cry5B loaded pSi particles was studied on an experimental hookworm infection in hamsters. Double-distilled water (ddH_2O), Cry5B, pSi particles and Cry5B loaded pSi particles were administered by oral gavage to infected hamsters (n=23). On day 18 post infection (P.I.), infected

animals (n=6 in each group, except n=5 for placebo group) were treated *per os* with total volume of 0.4 mL of relevant treatment targeting 6 mg Cry5B/Kg of hamster. Fecal egg counts as an indicator for reproduction capability and worm burden as remaining living worms inside hamster intestines were carried out as previously described to evaluate the therapeutic effect.[173]

4.3.6 Feeding Procedure to Track Particles Uptake by Nematodes

Rhodamine-labeled pSi particles were fed to nematode by incubating labeled pSi particles with L4 stage *C. elegan* was in M9 buffer and 100 mM glucose or with adult *A. ceylanicum* in hookworm culture media.[162] Particles were incubated with the nematodes in a mixture at 0.2 mg/mL. The *C. elegans* mixture was placed on the rocking stage for 2–24 h at room temperature and the worms were handpicked to agarose pad for subsequent fluorescence imaging. A 37 °C, 5% CO_2, incubator was used for *A. ceylanicum* incubation with labeled pSi particles.

4.3.7 Fluorescence Microscopy

Translocation of rhodamine-labeled pSi particles to nematode organs were visualized on an Olympus IX70 Delta Vision microscope (Applied Precision, Issaquah, WA, USA) with Nikon 10× or 40× objective lens and photographed by CoolSnap HQ^2 camera (PhotoMetrics, Inc, USA). Images of pSi ingestion were captured using differential interference contrast (DIC) and deconvolved using the SoftWorx program (Applied Precision). A RD-TR-PE filter (Ex/Em 535/617 nm) was used for fluorescent

image acquisition. To prepare specimens for microscopy, 8~10 *C. elegans* or 2 adult *A. ceylanicum* were mounted on 2% agarose pads containing 10 mM sodium azide; a coverslip was laid upon the worms to fix the position. Images were taken within 2 h after the slide was prepared to avoid drying of the agarose pads.

4.3.8 Protein Loading into Porous Si Particles

Approximately 3.0 mg of thermally oxidized pSi particles was suspended in 300 μL of 50 mM citrate buffer (pH 3.0). An aliquot of 1.0 mg/mL Cry5B (148 kDa, isoelectric point ≈ 5.1) in citrate buffer was added to the suspension and placed on the rotator (Model 24, Reliable Scientific, Inc.) for 16 h at room temperature. The particles were collected by centrifugation at 10000 rpm for 10 min to remove the supernatant. Additional wash with 1 mL citrate buffer was performed to remove loosely bound Cry5B. The adsorption of Cry5B onto the thermally oxidized pSi surface occurs *via* electrostatic interaction, where Cry5B bears slight positive charge and the oxide is negatively charged at pH 3. The amount of Cry5B loaded into the pSi nanostructure was calculated by subtracting the amount of Cry5B removed off the surface in the washing step from the total amount of Cry5B added to the sample using BCA protein assay. The Cry5B concentrations were determined by measuring the maximum absorption at 560 nm from the absorption spectra ranging 400–650 nm on a SpectraMax absorbance spectrometer (Molecular Devices) from a calibration curve assuming Beers' law.

4.3.9 Digestive Fluid for Cry5B Metabolic Fate Study

To determine how well the porous matrix could protect Cry5B in mammalian stomach, Cry5B loaded pSi particles were incubated in freshly prepared simulated gastric fluid (SGF), pH 1.2 with pepsin, as described in the United States Pharmacopeia.[83] Cry5B loaded pSi was added to a 0.5 mL solution of SGF for a final concentration of 2.5 mg/mL Cry5B and incubated at 37 °C with mild agitation. At 2 h time point, the solution was immediately quenched by neutralization with 0.2 M sodium carbonate.[160] Sample was stored on ice and applied to viability assay on *C. elegans* immediately.

4.3.10 *In vitro* Release Study

Cry5B loaded pSi particles (5.0 μm) were incubated with 1 mL of medium (equivalent to 0.64 mg/mL pSi concentration) at 37 °C with mild agitation. Three relevant media were chosen for the release study: 20 mM HEPES (pH 8.0), 50 mM citrate buffer (pH 3.0) and simulated intestinal fluid, without pancreatin, (pH 6.8). The supernatant containing released Cry5B was collected every 2 h and replaced with 1 mL of fresh, temperature-equilibrated, media over a 12 h period. Concentrations of the released Cry5B were determined using BCA protein assay described above. Signal from pSi dissolution in 3 separate media was subtracted from the data to correct for actual protein concentrations.

4.3.11 Statistical Analysis

All data in this article were expressed as the means ± standard error of mean. Dose-response curves were plotted using KaleidaGraph v. 4.1.3 (Synergy Software). Significance testing was conducted using one-tailed t-test assuming unequal variances in Microsoft Excel (2011). The LC_{50} values and associated 95% confidence intervals were calculated using PROBIT algorithm (from XLSTAT add-on to Microsoft Excel).

4.4 Results and Discussion

4.4.1 Morphology of PSi Particles

PSi particles were prepared to have two different physical dimensions: 5.3 ± 2.0 μm and 0.4 ± 0.2 μm (Figure 4.1A and B) using perforated etching described in experimental section. The average pore sizes measured from SEM images were 59.6 ± 13.9 nm for freshly etched pSi surface (Figure 4.1C) and 54.0 ± 15.0 nm (Figure 4.1D) for thermally oxidized pSi surface. No significant difference in pore dimension before and after oxidation was observed given the relatively wide pore dimension distribution. The physical size distribution of 0.4 μm particles was characterized by dynamic light scattering technique and shows Z-average of 422.4 nm in diameter with polydispersity index (PdI) of 0.343 for freshly etched particles; Z-average of 578.1 nm with PdI of 0.458 for thermally oxidized particles (as shown in Figure 4.2). The formation of oxide layer may cause some aggregation from electrostatic interactions between particles and can attribute to the slightly increased particle dimension measured in DLS. The size

distribution of 5.0 μm pSi particles was measured from SEM images with average particles size of 5.8 ± 2.0 μm (as shown in Figure 4.3).

As prepared pSi particles were subjected to furnace oxidation at 400 °C for 1 h and the infrared spectra confirms the conversion of Si–H species (2109, 2085, 903, 623 cm^{-1}) with Si–O–Si species (1058 cm^{-1}) in Figure 4.4. The thermally oxidized surface chemistry is chosen for its inert property with reduction-oxidation active compounds and therefore is less likely to cause conformational changes to the protein payload.[174]

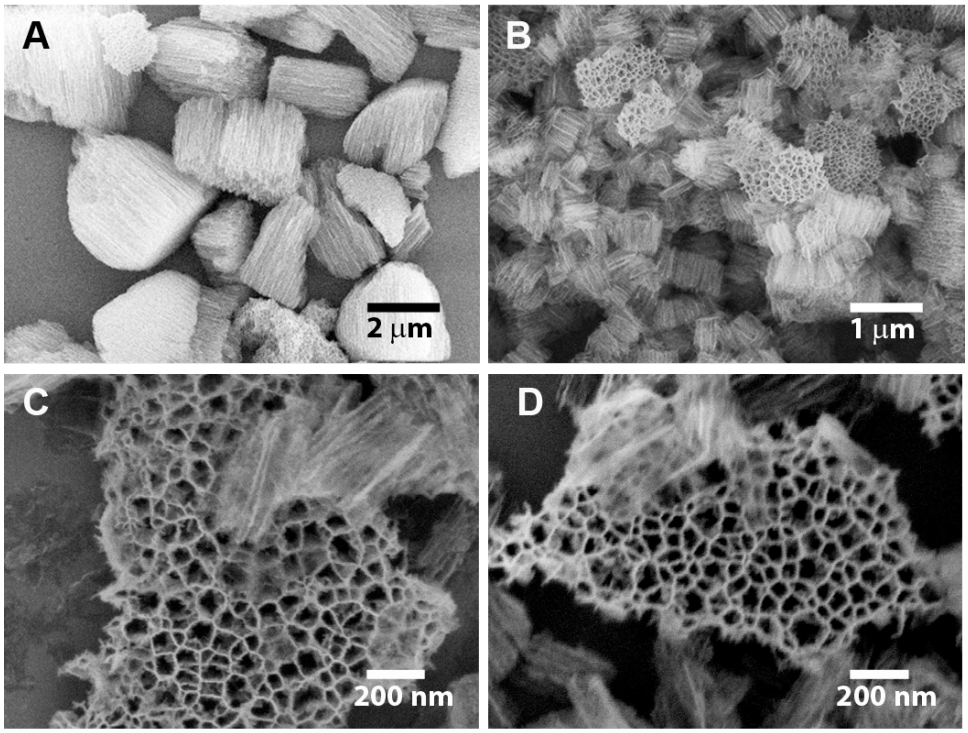

Figure 4.1 Scanning electron microscope images of pSi particles. (A) Freshly etched particles targeted 5.0 μm; (B) particles targeted 0.4 μm. (C) Pore morphology of freshly etched pSi particles; (D) pore morphology of psi particles after furnace oxidation at 400 °C for 1 h.

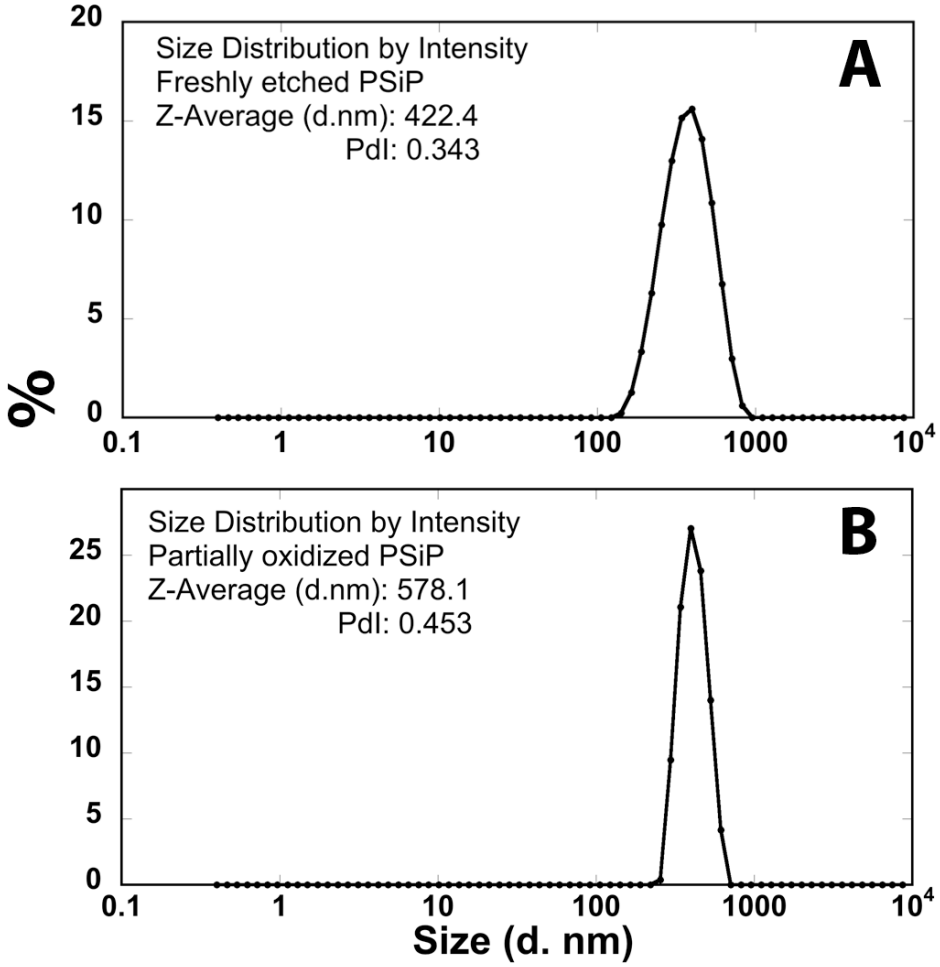

Figure 4.2 Size distribution of (A) freshly etched particles followed sonication and (B) partially oxidized porous Si nanoparticles (0.4 μm) measured in ethanol. The size distribution for 0.4 μm pSi nanoparticles were measured in ethanol on a Zetasizer Nano instrument (Malvern Instruments Ltd.) using dynamic light scattering principles.

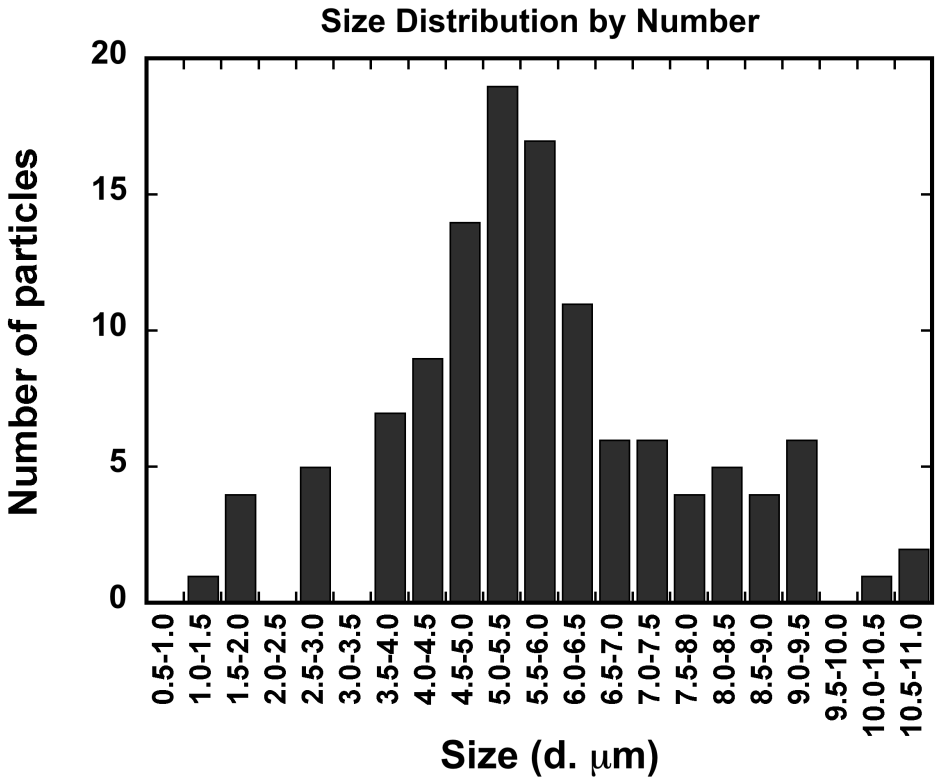

Figure 4.3 Size distribution of micron-sized porous Si particles targeting 5.0 μm measured from SEM images. The particle size is 5.8 ± 2.0 μm averaged from 120 particles.

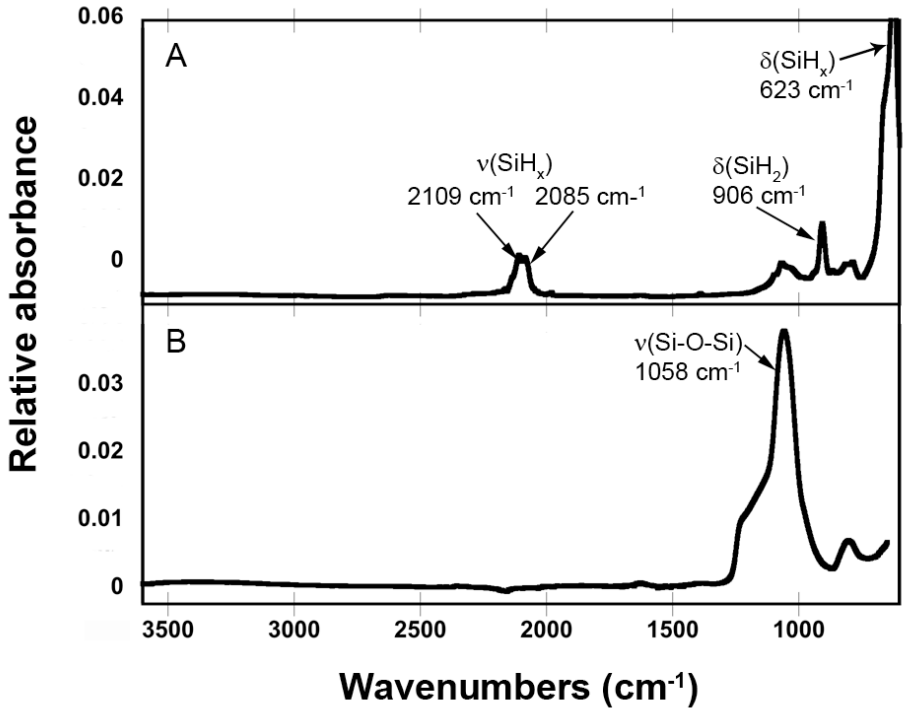

Figure 4.4 Infrared spectra of (A) freshly etched porous Si particles and (B) partially oxidized (400 °C, 1 h) particles. The characteristic peaks for Si-H species (2109, 2085, 906 cm^{-1}) were gone after oxidation treatment. Attenuated total reflectance Fourier transform infrared (ATR–FTIR) spectra were acquired on a Thermo Scientific Nicolet 6700 FTIR spectrometer with a Smart iTR accessory for ATR sampling. Spectra were each averaged from 128 scans. Spectral resolution was 4 cm^{-1} over the range 650-4000 cm^{-1}.

4.4.2 Biocompatibility of PSi Particles to *C. elegans*

The biocompatibility of thermally oxidized pSi particles to nematodes was addressed by a mortality assay where particles were incubated with *C. elegans* for 6 days and scored the biocompatibility by live/dead counts. As shown in Figure 4.5, thermally oxidized pSi particles bear little to no toxic effect on the mortality of *C. elegans* over 6 days of incubation at 25 °C for both 5.0 μm and 0.4 μm-sized pSi particles.

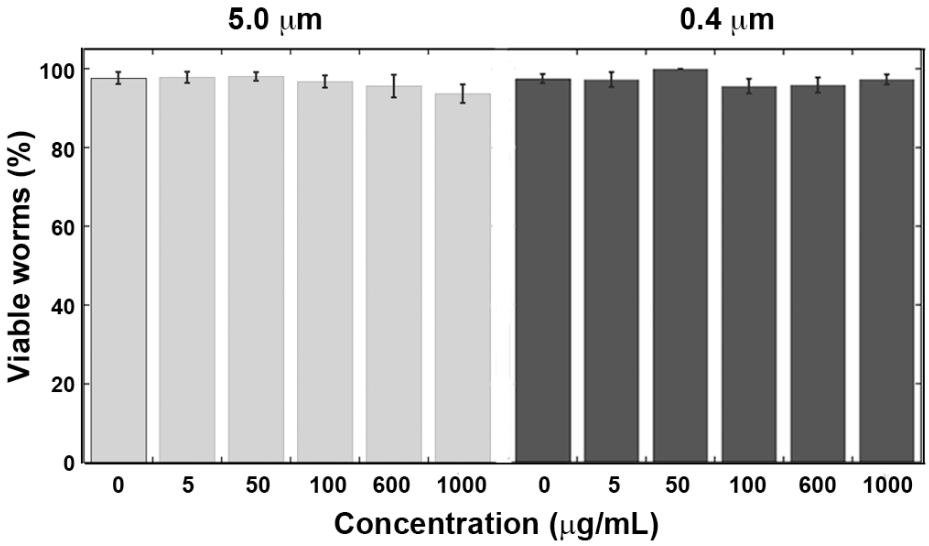

Figure 4.5 Untreated control *C. elegans* (0 μg/mL) and worm incubated with two different sizes of thermally oxidized pSi particles exhibit similar viability up to 1000 μg/mL over 6 days of incubation at 25 °C.

4.4.3 Cry5B Protein Loading Content

Loading of Cry5B was achieved by mixing thermally oxidized pSi particles with Cry5B (148 kDa, isoelectric point ≈ 5.1) in 50 mM potassium citrate buffer (pH 3.0) in which the protein is highly soluble and bears a net positive charge. The protein is expected to concentrate in the pores based on electrostatic force to the negatively charged partially oxidized pSi surface under the loading condition.[175] The loading efficiency was determined by depletion method where Cry5B concentration from loading and rinsing solutions were quantified from BCA assay. The difference in mass was attributed to the amount of Cry5B loaded into the oxide pSi particles and calculated to be 100–120 μg Cry5B/mg of pSi. Both the 0.4 μm and 5.0 μm pSi particles show similar loading efficiency. Additional evidence on the Cry5B adsorption to the pSi surfaces was the change in surface charge. The Zeta potential of pSi particles measurement in citrate buffer show the potential changed from –3.63 mV to 19.60 mV after Cry5B loading, confirming the presence of Cry5B on the pSi surfaces.

4.4.4 *In vitro* Release Study of Cry5B Loaded into PSi Particles

Cry5B loaded into pSi (5.0 μm) can be released and was characterized by temporal release profile in three different media relevant to *in vitro* assays and *in vivo* environment. Water insoluble Cry5B is known to be highly soluble in 20 mM HEPES (pH 8.0) and 50 mM citrate buffer (pH 3.0). Figure 4.6 shows the release profile of Cry5B in three different media over a 12 h period at 37 °C. Incubation with HEPES buffer showed the highest release rate of Cry5B up to 43.8%, while similar release rates

were observed in citrate buffer and simulated intestinal fluid. Two factors govern the release profiles of Cry5B from the porous matrix: (1) the solubility of Cry5B in the buffer solution which generates the concentration gradient for Cry5B to diffuse out of the matrix and (2) the pH of buffer solution that assists Cry5B release from the porous matrix via electrostatic repulsion. At pH = 8.0, both Cry5B and oxidized silicon surface exhibit net negative charge, together with the high solubility of Cry5B in HEPES, explains the highest total release of Cry5B into HEPES buffer among three buffers used in the study.

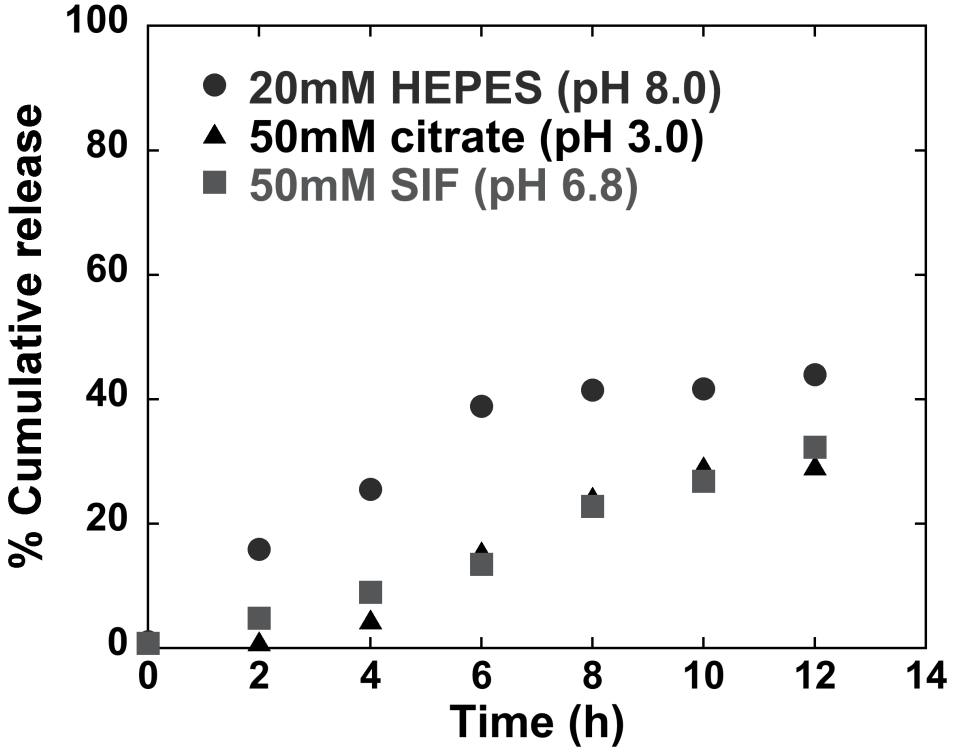

Figure 4.6 Release profiles of Cry5B from 5.0 μm pSi particles into aqueous 20 mM HEPES (pH 8.0), 50 mM citrate buffer (pH 3.0), and simulated intestinal fluid without pancreatin (pH 6.8) at 37 °C as a function of time. The concentrations of released Cry5B in each buffer collected at predetermined time point were quantified using BCA total protein assay.

4.4.5 Bioactivity Assay of Cry5B loaded PSi Particles on *C. elegans*

To evaluate if loaded Cry5B still retain therapeutic effect, Cry5B loaded pSi particles were incubated with *C. elegans* and scored in live/dead ratio compared to free Cry5B protein. Figure 4.7A shows the efficacy of free Cry5B towards *C. elegans* with LC_{50} concentration of 2.04 μg/mL, consistent with previous rounds (data not shown). As shown in Figure 4.7A, Cry5B loaded pSi particles requires higher concentration of Cry5B to achieve similar or even slight less efficacy compared to the free Cry5B protein. (The concentration of Cry5B in each well was calculated with loading efficiency of 100 μg Cry5B/mg pSi particles, equals to 664 μg/mL pSi particles, applied per well.) For four different sizes of pSi particles tested, there was apparent size effect from the pSi particles under the same dosage of Cry5B in well. Highest drug efficacy appeared in 0.4 μm pSi particles followed 1.0 and 5.0 μm particles; however, the smallest size (0.2 μm) studied showed least effect. It is worth noted that smallest particles appeared be severely aggregated after 6 days incubation and a majority of the particle aggregation had settled to the bottom of 48-well plates. We hypothesized two routes for Cry5B to access and affect the nematodes: (1) Cry5B diffused out of pSi nanostructures and was ingested by nematodes; (2) nematodes directly ingested pSi particles containing Cry5B and has Cry5B released inside the midgut of nematodes. In the controlled experiment of culturing medium without *C. elegans*, only 11% of Cry5B released from the pSi particles under the same experimental condition, confirming that most of the Cry5B protein was still retained inside the pSi particles. The relatively low solubility of Cry5B in culture media limited the release rate of Cry5B and therefore

limited the bioavailability of Cry5B to access nematodes. However, smaller particles in which nematodes can directly ingest provide another route for Cry5B to reach midgut of the worms. We later conjugated fluorescent dye to the pSi particles to monitor the translocation path inside the nematodes (Figure 4.8).

For oral delivery of therapeutic proteins, gastric fluid is the first challenge for drug delivery carrier to transit through and reach the target intestine where parasitic worms located. A simulated gastric fluid (SGF, pH 1.2, with pepsin) experiment was performed on Cry5B and Cry5B loaded pSi particles to evaluate the resistance of each against acidic environment. Particle size of 0.4 μm was chosen to load with Cry5B since it showed the best bioavailability among four particle sizes tested (Figure 4.7A). Both free Cry5B and Cry5B loaded pSi particles were exposed to SGF at 37 °C for 2 h under mild shaking. After neutralization, the acid treated Cry5B and Cry5B loaded particles were incubated with *C. elegans* and assess its efficacy. Compared to free Cry5B, Cry5B loaded to pSi particles show some degree of retention in efficacy (Figure 4.7B), suggesting the nanostructure provides some protection of Cry5B payload from SGF exposure.

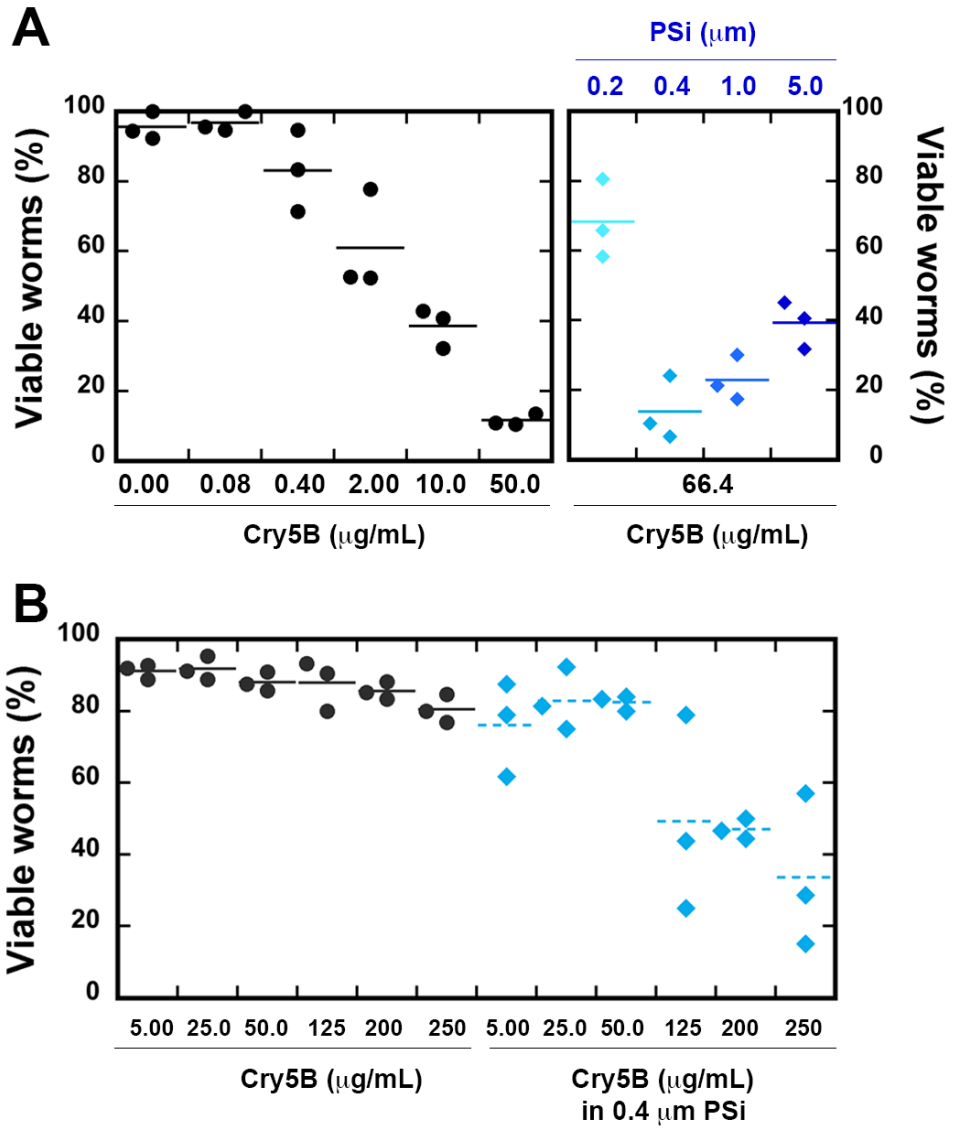

Figure 4.7 Bioactivity of Cry5B loaded into pSi nanostructures studied on *C. elegans*. (A) Left panel: control experiment of Cry5B alone on *C. elegans*. Right panel: bioactivity of Cry5B loaded in four different sizes of pSi particles. (B) Cry5B and Cry5B loaded pSi particles subjected to 2 h simulated gastric fluid treatment followed incubation with *C. elegans*.

4.4.6 Size Dependence on Porous Si Particles Uptake by *C. elegans*

To evaluate the hypothesis that nematode can directly ingest pSi particles, rhodamine dye was conjugated to oxidized pSi particles. Rhodamine dye was chosen to provide a differential vision to circumvent the autofluorescence from gut granules of *C. elegans*.[176] Rhodamine-labeled pSi particles were allowed to incubate with *C. elegans* for 2-24 h and imaged with fluorescence microscopy. The uptake of rhodamine-labeled pSi particles after 2 h incubation is shown in Figure 4.8, where the pSi particles (0.4 μm) translocate to the lumen of the pharynx and the intestine of *C. elegans*. PSi particles were exclusively found in primary organs of entry, e.g. the lumen of the digestive tract. No translocation to secondary organs was observed for particles of 0.4 μm in dimension, suggesting such size limited its endocytosis by lumen cells. Note the theoretical resolution limitation of microscopy used here is about 200 nm, it cannot be excluded that single or smaller particle penetrate further into *C. elegans.* The observed location of pSi particles remained excluded in pharynx and intestinal lumen of *C. elegans* is consistent with previous reported 50 nm silica nanoparticles uptake from *C. elegans*.[141] Particularly, the irregular shape and physical property were observed to cause clumps inside the lumen, which reflects on the aggregation close to the anus shown in Figure 4.8D. As for the larger pSi particles of 5.0 μm size, no significant uptake was observed under the same exposure time and this may due to size exclusion from the pharynx of the *C. elegans*.

The effect of Cry5B toxin on *C. elegans* takes place at the glycolipid receptors present abundantly at the inner surface of lumen.[177] For low solubility protein payload

like Cry5B, the release rate is highly hindered. As shown in Figure 4.6, only 43.8% of total Cry5B released from 20 mM HEPES over 12 h incubation at 37 °C. An alternative approach for delivering the protein would be to incorporate the low soluble protein in the porous matrix and consumption of the particles to the worms that would result in the indirect delivery of the protein. Engineering the physical dimensions of drug delivery carriers may aid in understanding the routes of anthelmintic delivery and for designing more effective drug delivery platforms for treatment of parasitic infections.

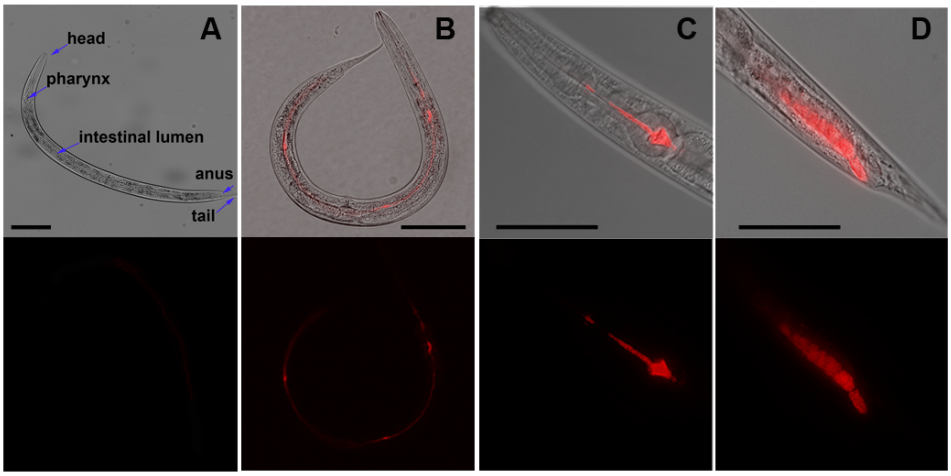

Figure 4.8 Fluorescence/DIC-merged and fluorescence images of *C. elegans*. (A) An untreated young adult. (B) Worm fed with 0.4 μm rhodamine-labeled pSi particles for 2 h. (C, D) zoomed in images of pharynx and anus part of the worms treated at the same condition as (B). A RD-TR-PE filter (Ex/Em 535/617 nm) was chosen to visualize the location of rhodamine-labeled pSi particles; low to no autofluorescence was observed at the exposure time and excitation wavelength used for worms treated with deionized water. Exposure times were identical for images (A) and (B). Scale bar were 50 μm, 50 μm, 100 μm, and 100 μm, respectively.

4.4.7 Porous Si Particles Uptake by *A. ceylanicum*

Ingestion of pSi particles was also observed on adult hookworms. Due to the thicker sample specimen of *A. ceylanicum*, high autofluorescence was observed throughout. The pharynx showed the least signal and therefore was chosen for imaging (Figure 4.9A). It is shown that adult hookworms could ingest 0.4 μm pSi particles after 2 h incubation (Figure 4.9B); the larger 5.0 μm pSi particles were not observed to be ingested under 2 h incubation (Figure 4.9C) eventually reach the pharynx after 24 h incubation (Figure 4.9D). As indicated with white arrow in Figure 4.9D, the large clump of pSi particles was restricted in the pharynx and could not transit through the intestine of hookworm. We also observed retropulsion of pSi clump inside the pharynx for all hookworm treated under this condition, suggesting worms itself trying to swallow the large particles through the restricted passage to intestine. The additional fluctuation of this retropulsion behavior may be helpful to leach out payload in drug delivery application.

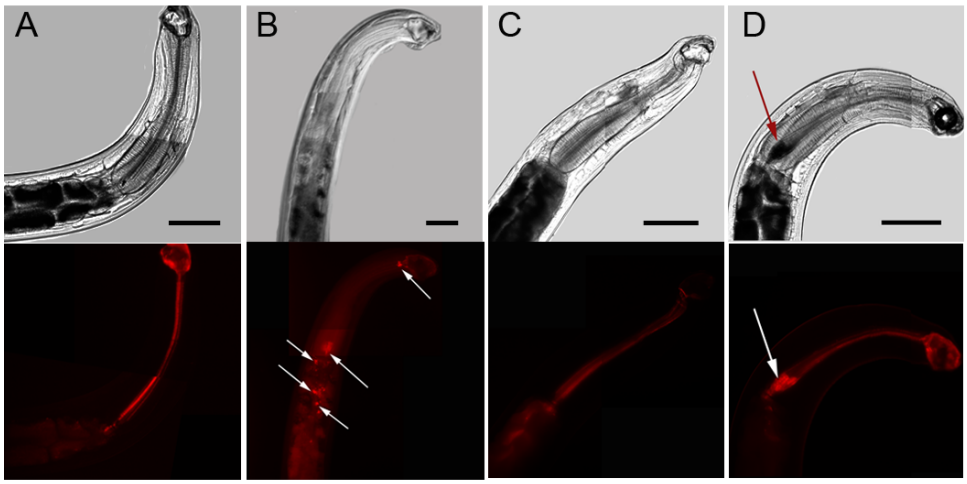

Figure 4.9 DIC and fluorescence images of *A. ceylanicum* with and without rhodamine-labeled pSi particles. (A) An untreated adult hookworm. (B) Worm fed with 0.4 μm rhodamine-labeled pSi particles for 2 h. White arrows indicate the clumps of pSi particles inside the lumen of adult hookworm. (C) Worm fed with 5.0 μm rhodamine-labeled pSi particles for 2 h, no apparent clumps of labeled particles were observed. (D) Worm fed with 5.0 μm labeled pSi particles up to 24 h. A RD-TR-PE filter (Ex/Em 535/617 nm) was chosen to visualize the location of rhodamine-labeled PSi particles; autofluorescence was observed at the exposure time used for imaging condition on worms treated with deionized water. Exposure times were identical for each image taken. Each scale bar represents 200 μm.

4.4.8 *In vitro* Bioactivity Assay of Cry5B Loaded PSi Particles on *A. ceylanicum*

Research has shown the mechanism of Cry5B action on *C. elegans* is conserved on the hookworms in which invertebrate-specific glycolipid receptor are functionally similar in hookworms as they are in *C. elegans*.[163] To evaluate if loaded Cry5B still retain therapeutic effect against *A. ceylanicum*, Cry5B loaded pSi particles were incubated with *A. ceylaicum* for 7 days and scored in a motility assay compared to free Cry5B protein and buffer. The efficacy of free Cry5B towards *A. ceylanicum* at final concentration of 5 μg/mL and Cry5B loaded to pSi particles of two different sizes were shown in Figure 4.10. The bare oxidized pSi particles post little to no toxic effect on the adult *A. ceylanicum.* Further more, Cry5B after loaded to the pSi particles still retains the bioactivity against adult hookworm over 7 days incubation.

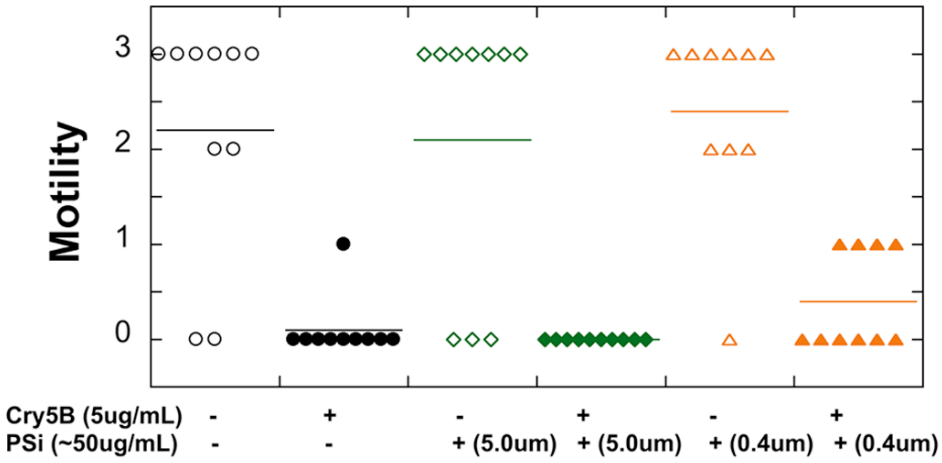

Figure 4.10 Effect of Cry5B loaded pSi particles on adult *A. ceylanicum in vitro*. Solid symbols indicates presence of Cry5B protein; open symbols indicates either the double deionized water or plain pSi particles controls. Two particle sizes were studied: 5.0 μm and 0.4 μm, with target Cry5B concentration at 5 μg/mL per well.

4.4.9 Single-dose *In vivo* Efficacy of Cry5B/PSi Particles Against Hookworm Infection in Hamster

Given the *in vitro* result from previous section where Cry5B retain its efficacy on *A. ceylanicum* after impregnated into pSi particles, we further conduct its efficacy test *in vivo* on hookworm-infected hamsters. The efficacy evaluation were followed previously reported methods to monitor hamster fecal egg counts and intestinal worm burden.[173] In a preliminary screening experiment of Cry5B loaded into 5.0 and 0.4 μm pSi particles on *A. ceylanicum* infected hamster, 5.0 μm sized pSi particles showed better efficacy compared to 0.4 μm. We therfore increased the numbers of hamster in each group and included Cry5B controls for repetition. On day 18 P.I., placebo (double-distilled water), Cry5B protein, 5.0 μm pSi particles and particles loaded with Cry5B were introduced to infected hamsters at 6 mg/kg mass ratio of Cry5B to hamsters *via* intragastric gavage approach. Effects on parasite progeny production was reflected in the fecal egg count change of 50.4 ± 16.5%, 70.1 ± 26.2%, 40.6 ± 28.1% and -53.9 ± 28.8% for water, pSi, pSi with Cry5B and Cry5B respectively on day 3 post treatment (Figure 4.11; relative to the average egg count before treatment.) Result of intestinal worm burden from each group was shown in Figure 4.12 that no apparent reduction in worm burden form the pSi particles loaded with Cry5B.

The differences between the *in vitro* results and the *in vivo* results can be attributed to a number of factors. One major factor is the difference in residence times of pSi particles exposed to the hookworms. In the *in vitro* assay on *A. celanicum*, pSi particles were allowed to incubate with hookworms up to 7 days before motility

scoring; while in the *A. ceylanicum* infected hamsters, pSi particles were believed to rapidly transit through the gastrointestinal tract within 1-2 days. The relatively slow release rate of Cry5B in simulated intestinal fluid, ~32% over 12 h (Figure 4.6), together with the slow dissolution rate of pSi particles (Figure 4.13), may account for limited bioavailability of Cry5B to reach hookworms. For the treatment of parasitic worms like *A. ceylanicum*, located mostly in the duodenum region in the intestine, where the reported transit time in human to range from a few seconds up to some minutes,[178] a burst release of payload is desired in drug delivery system. Alternatively, engineering the surface chemistry of drug carriers to target the mucosal layers with lectin, for example, may extend carriers retention time in the intestine. Prolonged retention time inside the intestine has advantages not only to extend time window for the release of payload from the carriers[179] but also increase the opportunity of carriers uptake by the parasitic worms.

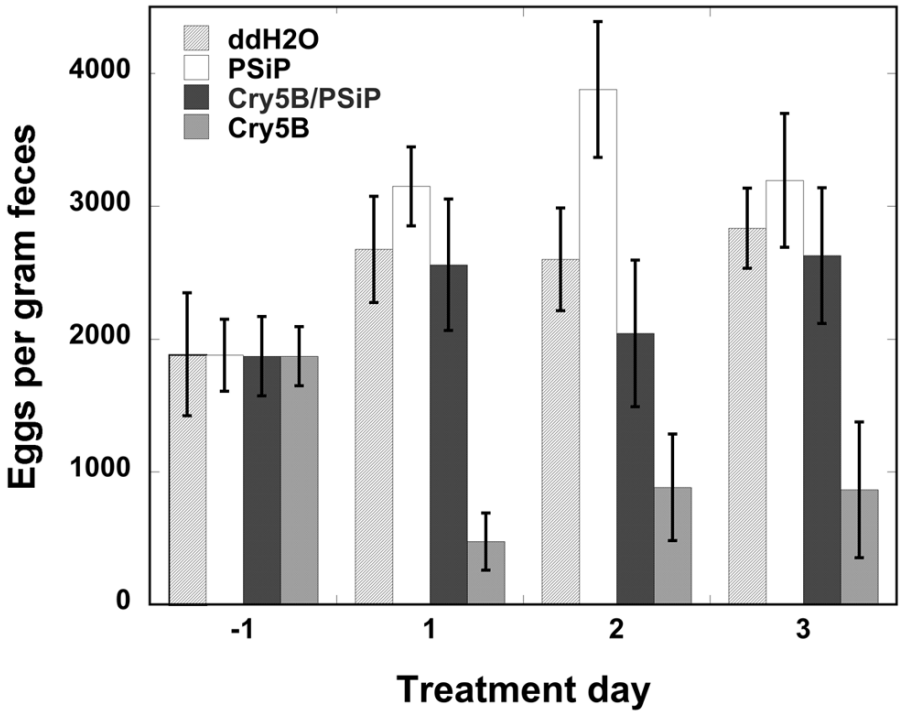

Figure 4.11 Effect of single dose of Cry5B loaded pSi particles on egg production in *A. ceylanicum* infected hamsters. Average eggs/gram of feces/hamster were shown for double-distilled water, ddH_2O, (n=5), pSi particles (n=6), Cry5B loaded pSi particles (n=6), and Cry5B-treated groups the day before treatment (-1) and later days until the animals were euthanized on day 3 post treatment. Each bar represents the mean value from each treatment group and the error bars indicate standard error of mean.

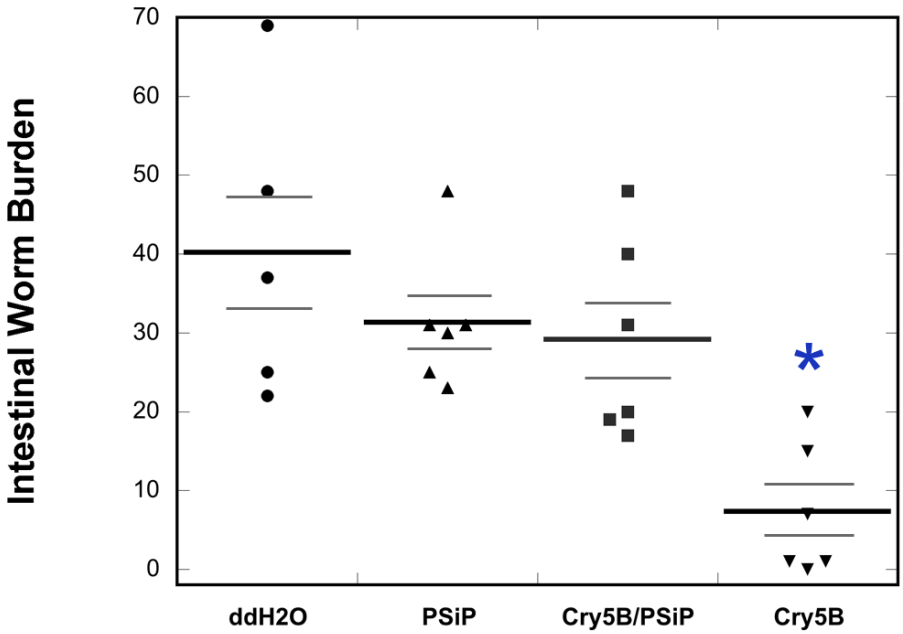

Figure 4.12 Effect of Cry5B loaded pSi particles on intestinal worm burdens in *A. ceylanicum* infected hamster. Numbers of adult worms found in intestine in each infected hamster treated with placebo (ddH_2O), pSi particle, Cry5B loaded pSi particle and Cry5B (6 mg/kg). The treatment was conducted on day 18 P.I. and intestinal worm burden assessed on day 22 P.I. Each separate symbol represents worm burden from each hamster. Long horizontal bars represent mean worm burdens for each treatment group; short horizontal bars represent the standard error of mean. A one-tailed t-test was used to compare data within each group, asterisk indicate statistical significance of treatment compared to placebo (ddH_2O) control. * $P<0.05$; no asterisk indicates no significant difference.

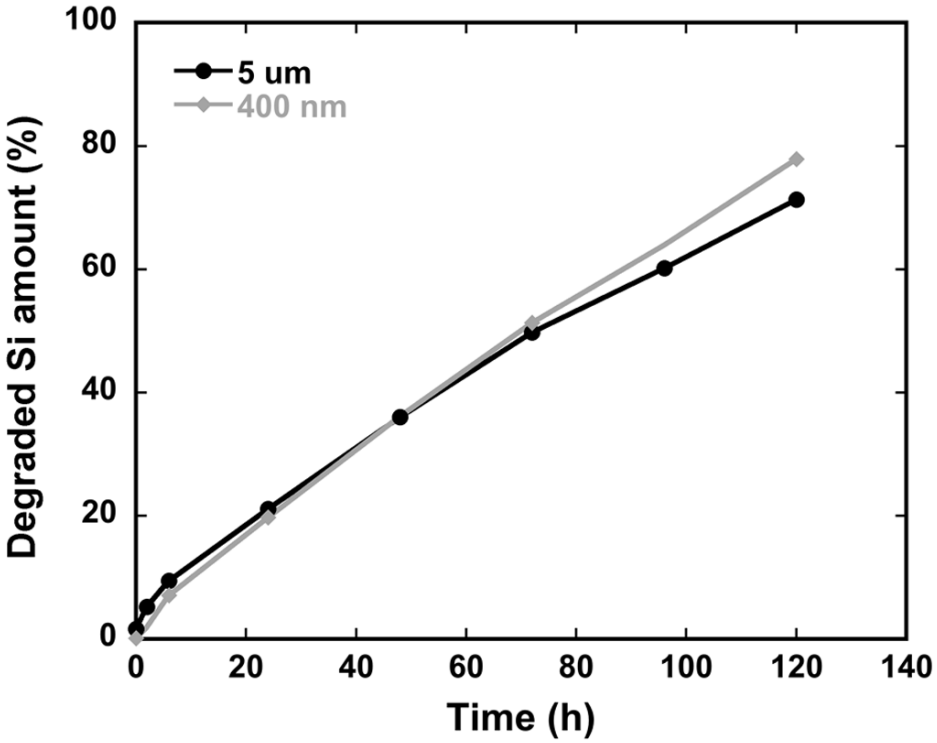

Figure 4.13 Dissolution profile of partially oxidized pSi particles of two different dimensions: (●) 5.0 μm and (◆) 0.4 μm incubated at 0.64 mg/mL concentration in simulated intestinal fluid at 37 °C as function of time. Silicon contents were quantified with inductively coupled plasma-optical emission spectrometry analysis.

4.5 Conclusions

The interaction of pSi particles on *C. elegans* and *A. ceylanicum* were reported. First of all, the pSi particles showed little to no toxicity on the mortality assay of *C. elegans* up to 1 mg/mL concentration over 6 days of incubation and motility assay on *A. ceylanicum* for 7 days incubation. In additional to the low toxicity of thermally oxidized pSi particles, the porous nature allows anthelmintic drug loading and release. The release profiles of Cry5B from pSi particles show the release rate is limited by the solubility of the Cry5B in buffer used for release study; Cry5B is most soluble in pH 8.0 HEPES buffer and the highest total release of 43.8% was achieved over 12 h incubation at 37 °C. We also observed a size dependency for drug efficacy in *C. elegans* assay. Conjugation of rhodamine dye to pSi particles allowed for tracking the uptake of pSi particle to the nematodes. For the *C. elegans*, only 0.4 μm-sized pSi can be ingested by the L4 stage worm and further reach the anus region while 5.0 μm pSi was excluded from ingestion. For the *A. celanicum*, both 0.4 and 5.0 μm were observed to taken up by adult *A. ceylanicum*, however, the 5.0 μm could not reach to the intestine and take longer time to accumulate inside the pharynx. Although the 5.0 μm cannot reach the intestine, the extended residential time of pSi particles in pharynx would increase the opportunity for Cry5B to diffuse out of the matrix. Drug delivery vehicle uptake by nematode could therefore be an alternative delivery route for anthelmintic drugs administration. Although the *in vivo* experiment did not show positive results, understanding the particles interaction with nematodes still provide some information for rational designing a more effective drug delivery system to treat parasitic diseases.

Surface modification to attach drug delivery vehicles to the mucosal layer is promising to distribute the vehicles adjacent to the site of parasitic worms and enhance the residential time and bioavailability of the anthelmintic drugs.

Chapter four, in part, is a reprint (with co-author permission) of the material as it appears in the following publication: Wu, C.; Hu, Y.; Miller, M.; Aroian, R.; Sailor, M. J., Interaction of Porous Si Particles with Biological Surfaces of Nematodes. Manuscript in preparation. The author of this dissertation is the primary author of this manuscript.

APPENDIX A

LABEL-FREE OPTICAL DETECTION OF BACTERIA ON A 1-D PHOTONIC CRYSTAL OF POROUS SILICON

A.1 Abstract

The construction of a specific, label-free, bacteria biosensor using porous silicon 1-D photonic crystals will be described. Bacteria resident on the surface of porous silicon act as scattering centers for light resonant with the photonic crystal; the diffusely scattered light possesses the optical spectrum of the underlying photonic crystal. Using a spectrometer fitted to a light microscope, the bacteria are imaged without using exogenous dyes or labels and are quantified by measuring the intensity of scattered light. In order to selectively bind and identify bacteria using porous Si, we use surface modifications to reduce nonspecific binding to the surface and to engineer bacteria specificity onto the surface. Bovine serum albumin (BSA) was adsorbed to the porous Si surface to reduce nonspecific binding of bacteria. The coatings were then chemically activated to immobilize polyclonal antibodies specific to *Escherichia coli*. Two *E. coli* strains were used in this study, *E. coli* DH5α and non-pathogenic enterohemorrhagic *Escherichia coli* (EHEC) strain. The non-pathogenic *Vibrio cholerae* O1 strain was used to test for antibody specificity. Successful attachment of antibodies was measured using fluorescence microscopy and the scattering method was used to test for bacteria binding specificity.

A.2 Introduction

There is a worldwide effort in the development of biosensors for detection, quantification and monitoring of specific bioorganisms. Bacteria sensors are of great

importance in clinical diagnostics, food analysis and environmental monitoring.[180] Biosensors are usually composed of two components: the recognition moiety for specific biomolecules or bioorganisms and the transducer that transmits the signal when a binding event occurs. Porous Si has been used successfully as an optical sensor of biorecognition events. The material has tunable structural properties[14] for admitting biomolecules, facile surface chemistries[181] for attaching biorecognition agents, and unique optical properties[4] for transmitting biorecognition events. These features allow the use of porous Si in various sensing applications.[17, 61, 182]

Recently, it was demonstrated that light reflected from a porous Si 1-dimensional photonic crystal can be used to quantify bacteria concentrations in media[62] and to sense biological events associated with cell viability.[182] The method relies on the ability of cells to scatter light from a highly reflective, colored porous Si chip, Figure A.1. When incident light is directed off-normal to the surface, light is reflected back at the same angle and no light is collected by the detection optics positioned normal to the surface (Figure A.1 inset A). However, when there are scattering centers such as bacteria on the surface, the reflected light is scattered by the bacteria in all direction and some light is collected by the detection optics (Figure A.1 inset B). Porous Si rugate filters are generated by applying a sinusoidal varying current density during the duration of etch. The reflective color can be tuned to a variety of wavelengths[26] and for this study porous Si films were generated with maximum peak position at 590 nm, producing material that appears green to the eye. For detecting bacteria by the scattering method, the intensity of the characteristic optical signature can be monitored to measure bacteria density on the porous Si film as bacteria nonspecifically adsorb to

the surface. Therefore, we hypothesized that the scattering technique could be used to investigate antifouling and antimicrobial properties of coatings designed to minimize bacterial adhesion or viability[183] and provide a starting template to monitor specific bacteria binding to the surface. The surface chemistry of electrochemically etched silicon can be exploited to form a highly adhesive surface for adsorption of antifouling coatings. Specific recognition moieties, such as an antibody, can be covalently coupled to this antifouling surface and used for specific binding of a bacteria target.

Here, we demonstrate that porous Si photonic crystals can be used as a platform for label-free optical detection of pathogenic bacteria. The biosensor was constructed by first creating a porous Si thin film, modifying the surface chemistry, adsorbing an antifouling layer, and then covalently attaching antibodies specific to *E. coli* to the antifouling layer. Bacteria binding efficiency is detected and quantified from the intensity of scattered light from the underlying porous Si photonic crystal. Bacteria detection was monitored and recorded by measuring the scattering spectra from porous Si chips under different surface conditions and microscope images were collected to verify the spectral observations.

A.3 Experimental Methods

A.3.1 Fabrication of Porous Silica

Porous Si chips were prepared from single-crystal, highly doped p-type silicon (boron doped, 0.9 mΩ–cm resistivity, <100> orientation) by electrochemical etch in a 3:1 v/v solution of aqueous hydrofluoric acid (48%, EMD Chemicals Inc., Gibbstown,

NJ) and 100% ethanol (Pharmco-AAPER, Brookfield, CT). A sinusoidal current density ranging from 13 to 88 mA/cm2 was used to generate a rugate filter with a sharp reflectivity peak in the spectrum between 540-590 nm. Freshly etched porous Si was then thermally oxidized in a tube furnace for 1 h at 400 °C.

A.3.2 Physical Characterization of Porous Silica

Modified porous Si samples were characterized by Fourier transform infrared (FTIR) spectroscopy using a Nicolet 6700 FT-IR Spectrometer in reflectance mode. Sessile drop contact angle measurements were conducted by applying a droplet of 5 μL deionized water onto the porous Si surfaces. A commercial digital camera was used to capture the droplet interaction and Adobe Photoshop was used for image analysis. Contact angles for a droplet were determined by taking the average of the two angles on either side of the droplet. A total of three droplets were averaged for each surface condition.

A.3.3 Adsorption of Antifouling Layer on Porous Si

A bovine serum albumin (BSA) layer was applied to the porous Si thin film prior to antibody coupling. To achieve high BSA adsorption to the oxidized porous Si, a 0.75 mM BSA solution was prepared by dissolving 0.05 g of BSA (Sigma-Aldrich) in 1 mL of pH 5 phosphate solutions. The pH 5 solution was prepared by dissolving 0.3603 g/L Na_2HPO_4 (Sigma-Aldrich) and 13.6145 g/L NaH_2PO_4 (Sigma-Aldrich) in deionized water. The oxidized porous Si chips were immersed in the BSA solution for

2 h at room temperature with gentle shaking for 30 sec every 30 min. Chips were then rinsed three times with 2 mL of pH 5 solution to remove excess BSA.

A.3.4 Coupling of Antibody to Antifouling Surface

Two approaches were used to generate an intermediate active ester on BSA for coupling with free amines on the antibody. We investigated both pentafluorophenyl ester and N-hydroxysuccinimidyl ester to activate carboxylic acid groups on the BSA layer. For the first approach, the BSA-coated porous Si chips were activated by immersion in a solution of dimethylformamide containing 0.1M 1-Ethyl-3-(3-dimethylaminopropyl)carbodiimide (EDC) (Sigma-Aldrich) and 0.2M pentafluorophenol (Sigma-Aldrich) for 10 min. The activated surfaces were rinsed three times with ethanol and dried under a stream of nitrogen prior to antibody coupling. For the second approach, the BSA-coated porous Si chip was immersed in pH 5 solution containing 0.5 M EDC and 5 mM N- hydroxysulfosuccinimide (sulfo-NHS) (Sigma-Aldrich) for 30 min.[184] The surfaces were then rinsed three times with pH 5 solution and were kept in wet condition without drying. After ester activation of the BSA layer, the surfaces were rinsed with 2 mL of PBS (pH 7.4) (Mediatech, Inc., VA) three times before applying the antibody. Modified porous Si chips were placed at the bottom of a polystyrene Petri dish and immersed in 2 mL of 5 μg/mL rabbit anti-*E. coli* IgG (Meridian Life Science Inc., ME) for 2 h at 25°C. The samples were then rinsed five times with 2 mL of PBS (pH 7.4) to remove unbound rabbit anti-*E. coli* IgG.

Antibody attachment to the ester-activated BSA surface was verified using a fluorescein isothiocyanate (FITC)-conjugated rabbit IgG (Sigma-Aldrich). Activated surfaces were rinsed with pH 7.4 PBS three times prior to antibody coupling. These samples were immersed in solution of 68.6 μg/mL FITC-conjugated rabbit IgG in PBS (pH 7.4) for 2 h in the dark. The FITC-conjugated rabbit IgG was applied at a higher concentration than rabbit anti-*E. coli* IgG in order to maximize the fluorescence intensity for analysis. The samples were rinsed five times with 2 mL of PBS (pH 7.4) to remove unconjugated antibodies. It is important to point out that the amide bond bioconjugation occurs between both antibody and BSA and between the individually adsorbed BSA molecules. This crosslinking of the BSA molecules results in stabilization of the antifouling coating.[183]

A.3.5 Cell Culture on Porous Si

Three different strains of bacteria were used in this study. They were enterohemorrhagic *Escherichia coli* (EHEC) strain 86-24 h11, *E. coli* DH5α, and *Vibrio cholerae* CVD 101 (provided by Prof. Chao and Dr. Camilla Rang, University of California, San Diego).[185] EHEC strain 86-24 h11 is a derivative of wild type strain 86-24 containing a mutation in the *stx*A_2 gene that inactivates Shiga toxin 2.[186] *V. cholerae* A^-B^+ CVD 101 is a vaccine strain prepared by recombinant DNA techniques from pathogenic classical Ogawa 395, in which the A subunit of cholera toxin was deleted.[187] Stocks were stored frozen at -80 °C. All bacteria were grown on Luria Broth (LB) agar plates at 37 °C overnight. Plates of EHEC 86-24 h11 and *E. coli* DH5α were kept at 4

°C while plates of *V. cholerae* CVD 101 were stored at 15 °C. The cell culture was prepared by selecting a single colony from the culture plate and incubating with LB liquid medium at 37 °C overnight. Before applying bacteria cells to modified porous Si chips, the cell cultures were refreshed to achieve log-phase growth by diluting overnight cultures (10%) into fresh LB medium and incubating aerobically for 2 h. The log-phase culture was diluted to an optical density of 0.5 at 600 nm before being applied to the functionalized porous Si chips. The functionalized chips were placed at the bottom of polystyrene Petri dish and incubated in 2 mL of the bacteria suspension with shaking (50 rpm) for 1 h at 32 °C. Chips were then rinsed with 2 mL reduced-NaCl LB medium with gentle shaking for 2 min, and this rinsing method was repeated five times to remove unattached cells. After rinsing, samples were allowed to dry in air overnight before viewing. Bacteria cell concentration at optical density 0.5 was confirmed by colony plating on LB agar plate and recorded in units of colony forming unit per milliliter (CFU/mL). The average concentration of EHEC 86-29 h11 and *E. coli* DH5α is 6.8×10^8 CFU/mL and the concentration of *V. cholerae* CVD 101 is 5.1×10^9 CFU/mL at optical density 0.5.

A.3.6 Optical Spectrum Acquisition

Bacteria attachment efficiency on various surfaces of porous Si was investigated using the scattering method described in Figure A.1. Images of the porous Si surfaces were obtained using a light microscope (Nic-PlanTM, IR microscope, 10x objective) with attached camera (Nikon COOLPIX 4300). Incident light images were recorded

using normal incident light from the microscope illuminator. For scattering images, the microscope illuminator was turned off, and light was directed onto the surface of porous Si chip at a 52° angle relative to normal. Reflectance spectra were obtained from the porous Si film using a halogen light source incident at an angle approximately 14° off-normal and reflected light was collected by a CCD Spectrometer (Ocean Optics, S-2000) positioned normal to the surface. The reflectance spectrum displayed a sharp peak between 540-590 nm.

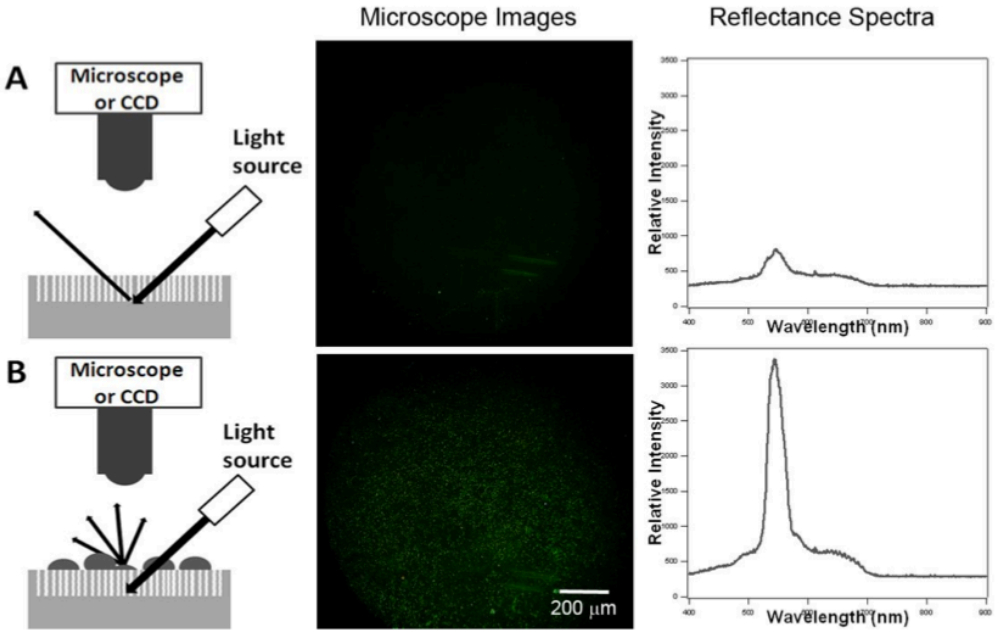

Figure A.1 Optical set-up to observe scattering from cells on a porous Si photonic crystal. (A) Light reflecting off the porous Si film from an off-normal source results in minimal light reaching the microscope objective aligned with its optical axis normal to the chip. (B) Scattering centers, like bacteria cells, on the surface of the photonic crystal cause some of the resonant light from the photonic crystal to be scattered into the microscope objective or detection optics. The left column illustrates the optical set-up; the middle column shows microscope images of the porous Si surface when white light is directed at an angle to the surface; the right column shows spectra collected by a CCD spectrometer with intensity of scattered light correlating to bacteria density on the surface.

A.3.7 Fluorescence Measurement

FITC-conjugated rabbit IgG was used to verify activation efficiency and antibody attachment on the BSA surface. The samples were imaged using a fluorescence microscope (Nikon Eclipse LV 150) and images were captured using a CCD camera (Photometrics CoolSNAPHQ2). A 480 ± 20 nm excitation filter and a 535 ± 25 nm emission filter were used. Images were processed using MetaMorph (Universal Imaging, Westchester, PA) to calculate average intensity from each sample.

A.4 Results and Discussion

A.4.1 Characterization of Porous Si

Fourier transform infrared spectroscopy was used to verify the chemical modification of freshly etched porous Si and adsorption of the BSA layer. The FTIR spectrum of a freshly etched porous Si chip (Figure A.2a) shows the presence of Si–H_x stretching modes with bands at approximately 2100cm^{-1}. Also, a Si–H_2 scissor deformation band at 910 cm^{-1} is observed as well as a Si–H wag deformation at 650 cm^{-1}. Furnace oxidized porous Si (Figure A.2b) shows a strong vibrational band corresponding to asymmetric Si–O–Si stretching around 1100 cm^{-1}. After BSA adsorption to the oxidized porous Si surface, bands assigned to amide I (at 1643 cm^{-1}) and amide II (at 1559 cm^{-1}) in the FTIR spectrum are observed. The amide bands indicate the presence of the BSA protein.

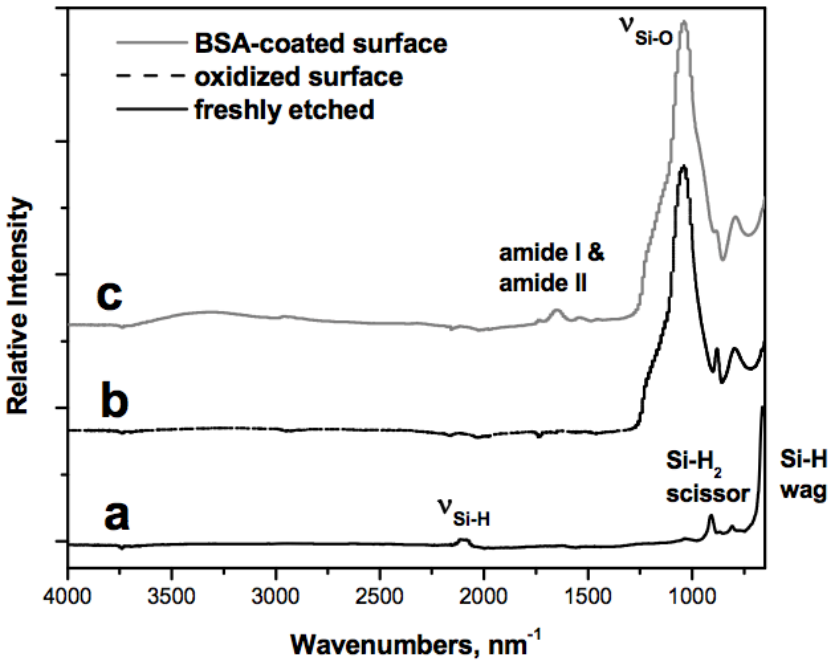

Figure A.2 Fourier transform infrared (FTIR) spectral characterization of (a) freshly etched, (b) oxidized, and (c) BSA coated porous Si surfaces.

Contact angle measurements confirm surface oxidation of the porous Si film prior to adsorbing protein to the surface. The contact angle of freshly etched porous Si is 110.2 ± 3.5° indicating the hydrophobicity of the porous layer. Oxidation of the surface by heating at 400 °C transforms the surface to a hydrophilic layer with a contact angle of 29.2 ± 1.8°.

A.4.2 Coating of BSA onto Porous Si

Nonspecific binding of bacteria is a serious issue for constructing bacteria sensors because it can yield false positive signals for intended binding events. Therefore surface coatings or surface chemical modifications are commonly proposed to minimize bacterial attachment and colonization on synthetic surfaces.[188] Bovine serum albumin (BSA) is commonly used to inhibit biomolecule and bacteria non-specific adhesion to surfaces. For example, a crosslinked albumin coating was shown to effectively inhibit bacterial adherence on titanium surfaces up to 85% over a 20-day period.[183]

In our study, we used adsorbed BSA on the oxidized porous Si surface to create a layer that would inhibit nonspecific adsorption of bacteria. Optimized conditions for maximum BSA adsorption on the hydrophilic silica-water interface is at pH 5.1,[189] which is close to the isoelectric point of BSA (pH 4.8). The effectiveness of the BSA adsorbed layer at preventing bacteria adhesion to the porous Si chip was measured using the scattering method and is discussed below.

A.4.3 Fluorescence Confirmation of Antibody Attachment

The BSA layer is known to effectively reduce nonspecific binding of proteins. Therefore we adapted two approaches to activate the BSA layer for antibody coupling. FITC-conjugated rabbit IgG was used to verify antibody attachment onto the ester-activated BSA surface. The fluorescence intensity from the FITC dye, measured for different surface modifications, is shown in Figure A.3. FITC-conjugated rabbit IgG adsorbed to an uncoated oxidized porous Si surface gave extremely high fluorescence intensity, indicating high nonspecific adsorption of the antibody to the surface. However, when a BSA layer is adsorbed to the oxidized porous Si surface, the fluorescent antibody is effectively prevented from adsorbing to the surfaces as observed by the lower fluorescence intensity. When the pentafluorophenol (PFP)/EDC route is used to activate the BSA layer for covalent attachment of the antibody, higher fluorescence intensity is observed relative to the antibody-exposed BSA layer without ester-activation. This indicated that antibody has been successfully coupled to the BSA layer. On the other hand, EDC/sulfo-NHS ester activation showed no increase in fluorescence intensity relative to the antibody-exposed BSA layer without ester-activation. Hereafter, we used pentafluorophenyl esters to activate the BSA layer for coupling the antibody specific for the target bacteria, *E. coli.*

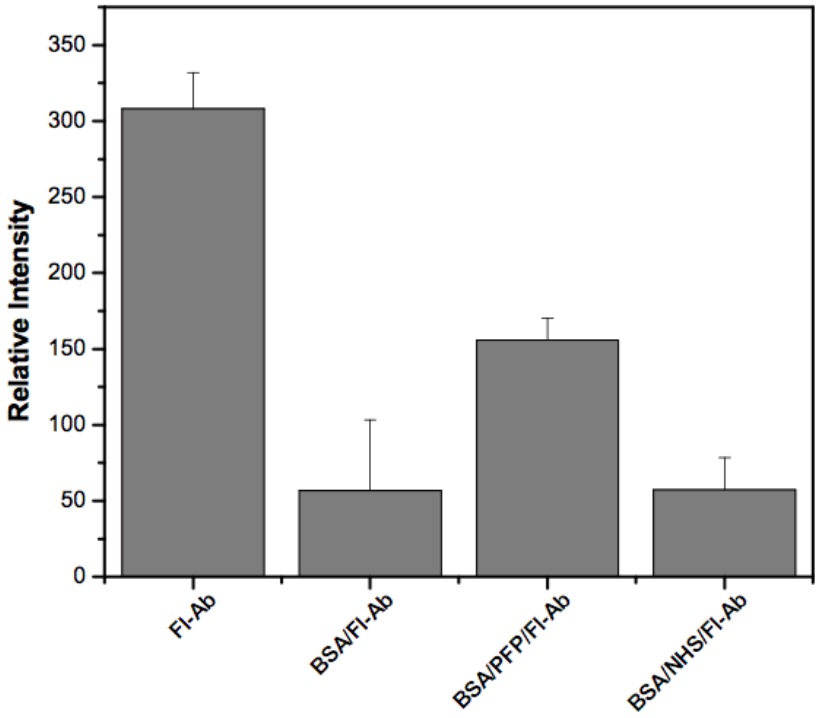

Figure A.3 Relative fluorescence intensity of a FITC-conjugated rabbit IgG antibody attached to modified oxidized porous Si surfaces. Antibody adsorbed to oxidized porous Si surface (Fl-Ab), antibody adsorbed to the BSA layer on oxidized porous Si (BSA/Fl-Ab), antibody covalently attached to the EDC/PFP ester-activated BSA layer (BSA/PFP/Fl-Ab), antibody covalently attached to the EDC/NHS ester-activated BSA layer (BSA/NHS/Fl-Ab).

A.4.4 Quantification of Bacteria Adhesion

A.4.4.1 Quantification of Bacterial Adhesion by Scattering Intensity

The scattering method illustrated in Figure A.1 was used to measure the efficiency of the BSA coating at preventing nonspecific adsorption of bacteria and to measure specific attachment of bacteria when the surface was chemically modified with an antibody specific for *E. coli.* The intensity of light scattered from the porous Si photonic crystal is correlated to the concentration of bacteria resident on the porous Si surface.[62] Representative scattering spectra are plotted in Figure A.4 and illustrate the relative binding efficiency of different bacteria on the modified porous Si surfaces. When an antibody for *E. coli* is covalently attached to the surface and exposed to *E. coli*, a higher intensity of light is scattered from the surface than the surface exposed to *E. coli* without antibody attached. Similar spectral intensities are observed from the antibody-coupled chip incubated with cell growth media and the same type of chip incubated with *V. cholerae*, indicating that little or no *V. cholerae* cells attached to the surface modified to specifically bind *E. coli*. Figure A.4 inset B shows the linear dependence of scattering intensity to numbers of cell resident on the porous Si surface; we can therefore quantify bacteria concentration on the surfaces by measuring the intensity of reflectance peak. The numbers of cells were determined by performing cell counts using the captured microscope images. The offset intensity in Figure A.4 inset B when no bacteria are present is due to stray light entering the detection optics when the angle is fixed at 14° from the surface normal.

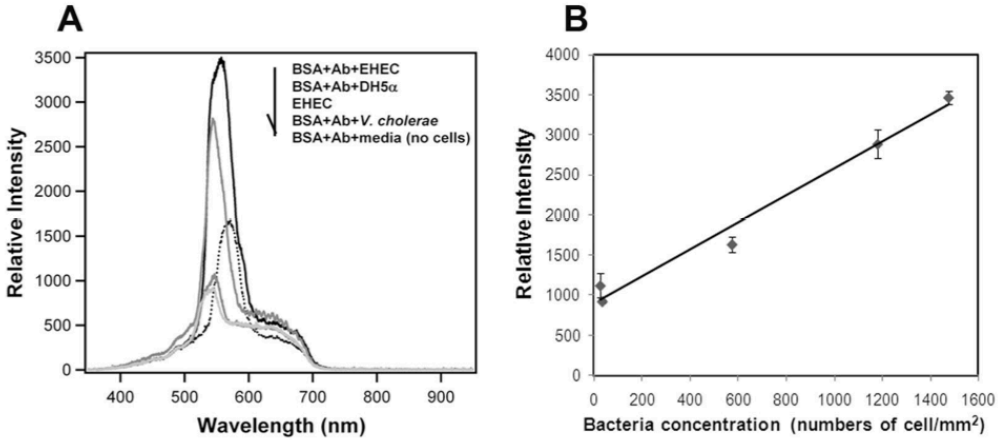

Figure A.4 Quantification of cell adhesion by scattering spectrum from samples prepared with different surface modifications. (A) Relative scattering intensity on PFP-activated rabbit anti-*E. coli* IgG coupled BSA surface with different bacteria strains applied. Surfaces coated with BSA gives a blue shift in the observed spectra. *E. coli* strains gave higher reflectance intensity towards antibody-coupled surface than *V. cholerae*. (B) Results from (A) representing the correlation between scattering intensity and cell concentration. Conventional cell counting methods were used to quantify cell concentration.

In Figure A.5, the scattering intensities observed for the different surface conditions and cell applications are presented. The scattering intensities were normalized to the sample consisting of an antibody-coupled BSA-coated surface with EHEC applied for each set of experiments, and the normalized values were averaged from experiments performed on 4 different days. Standard error is used to express the intensity distribution. *V. cholerae* and *E. coli* are both gram negative, rod shaped bacteria. *V. cholerae* is somewhat smaller than *E. coli. E. coli* has a cylindrical shape of ~1 micron in diameter and ~2.5 microns long while *V. cholerae* has dimensions of ~1 micron in diameter and ~2 microns long. The oxidized porous Si chip exposed to EHEC has a higher scattering intensity than the BSA-coated chip exposed to EHEC, indicating BSA prevents nonspecific cell adhesion to porous Si. *E. coli* specific antibody-coupled surfaces exposed to the *E. coli* strains, EHEC and DH5α, demonstrated higher scattering intensities than non-specifically adsorbed *V. cholerae*. Some scattering of light is observed from material incubated with *V. cholerae* indicating that the BSA layer reduces nonspecific binding of bacteria but it does not completely block binding.

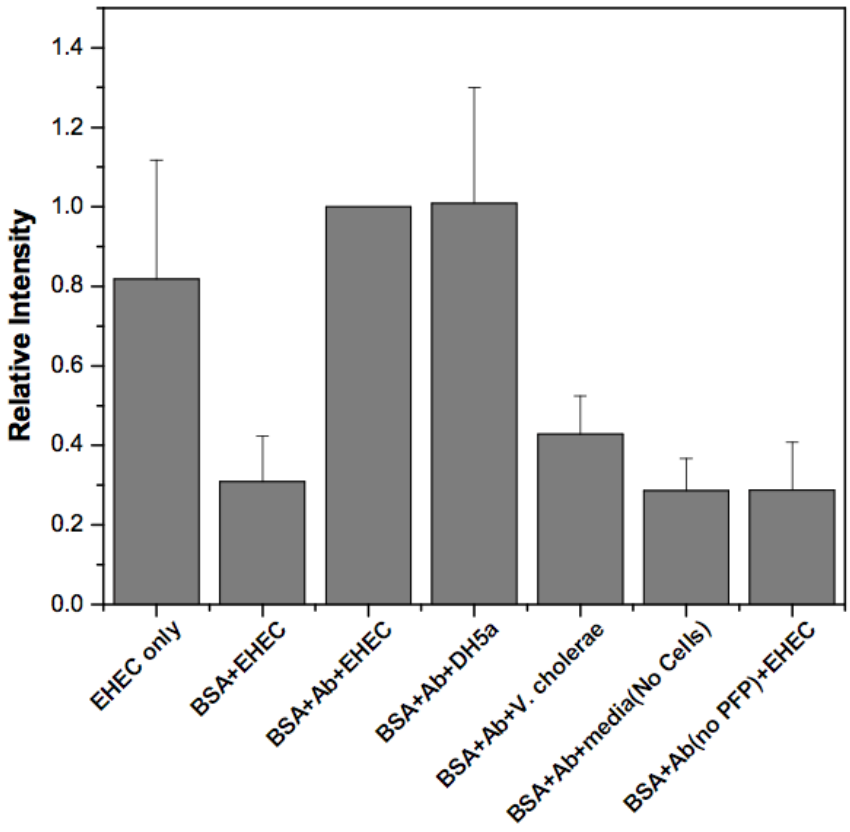

Figure A.5 Intensity of the scattered light spectrum from surface-modified oxidized porous Si chips allows quantification of cell adhesion. EHEC strain of *E. coli* nonspecifically attached to uncoated oxidized porous Si surface (EHEC only), EHEC attached to BSA-coated oxidized porous Si surface (BSA+EHEC), EHEC attached to PFP ester-activated BSA layer and antibody-coupled surface (BSA+Ab+EHEC), DH5α attached to PFP ester-activated BSA layer and antibody-coupled surface (BSA+Ab+DH5α), *V. cholerae* attached to PFP ester-activated BSA layer and antibody-coupled surface (BSA+Ab+*V. cholerae*), media incubation on PFP ester-activated BSA layer and antibody-coupled surface (BSA+Ab+media (No Cells)), EHEC-attached, antibody-adsorbed BSA layer without PFP activation (BSA+Ab(no PFP)+EHEC).

A.4.4.2 Quantification of Bacterial Adhesion by Cell Counting

An advantage of using the porous Si photonic crystal for the cell scattering method is that no dyes or labels are necessary to observe the cells resident on the substrate. The cells appear with the color of the underlying porous Si film, which in this case is green and the background where no cells are present is black. The degree of adhesion of bacteria is apparent in the microscope images of Figure A.6. Cell counts from three different regions of the chip were averaged from four separate experiment sets, Figure A.7. In general, EHEC cells attached to oxidized porous Si, producing bright regions in the images associated with increased light scattering efficiency (Figure A.6 inset A and Figure A.7). The BSA-coated surface (Figure A.6 inset B), generates relatively little scattered light, indicating that nonspecific binding of bacteria is greatly reduced relative to an uncoated surface. The inhibitory effect to bacteria attachment was ~74% based on cell counting. The larger scattered light intensity observed from *E. coli* strains relative to *V. cholerae* CVD 101 from the surfaces containing surface-attached rabbit anti-E.coli IgG (Figure A.6 inset D, E, and F) indicates that these surfaces are effective at capturing a targeted organism. The relative bacteria concentrations on the modified oxidized porous Si surfaces obtained from cell counting (Figure A. 7) are similar to the values obtained from the spectral light scattering experiments (Figure A. 5). Some light scattering centers are also observed in the control samples that contain only medium and no cells (Figure A. 7). These features are attributed to adventitious particulates in the dish, salt precipitated from the dried LB medium, and dust particles from the air.

With carefully selected intensity and angle of incident light and proper control sample, scattering intensity can be used as a measurement tool to define bacteria concentration on the porous Si surface without the use of an exogenous dye.

The electrochemistry of porous Si allows the generation of photonic crystals with resonance wavelengths spanning a large range;[26] the distinct wavelengths can be designed to couple to different antibodies for immunoassays, providing an alternative to the use of organic fluorophores or dyes in bioassays.

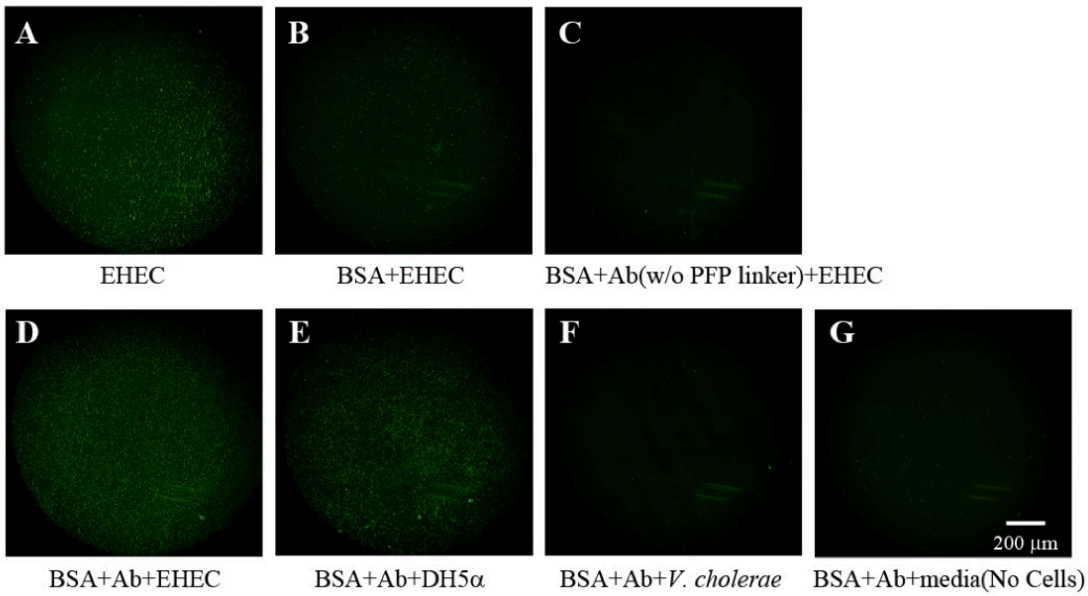

Figure A.6 Optical microscope images of bacteria on BSA-coated, uncoated, and antibody-coupled thermally oxidized porous Si when light is directed at an angle to the surface. (A) Image of EHEC applied to oxidized porous Si without BSA coating. (B) Image of porous Si with BSA coating and EHEC. (C) Images with BSA layer exposed to EHEC, but no pentafluorophenol activator was used in the antibody coupling reaction. (D) Image of BSA-coated surface modified with rabbit anti-*E. coli* IgG and exposed to EHEC cells. (E) BSA-coated surface modified with rabbit anti-*E. coli* IgG and exposed to DH5α cells. (F) BSA-coated surface modified with rabbit anti-*E. coli* IgG and exposed to *V. cholerae* cells. (G) Media incubation on rabbit anti-*E. coli* IgG-coupled BSA-coated surface and no addition of cells.

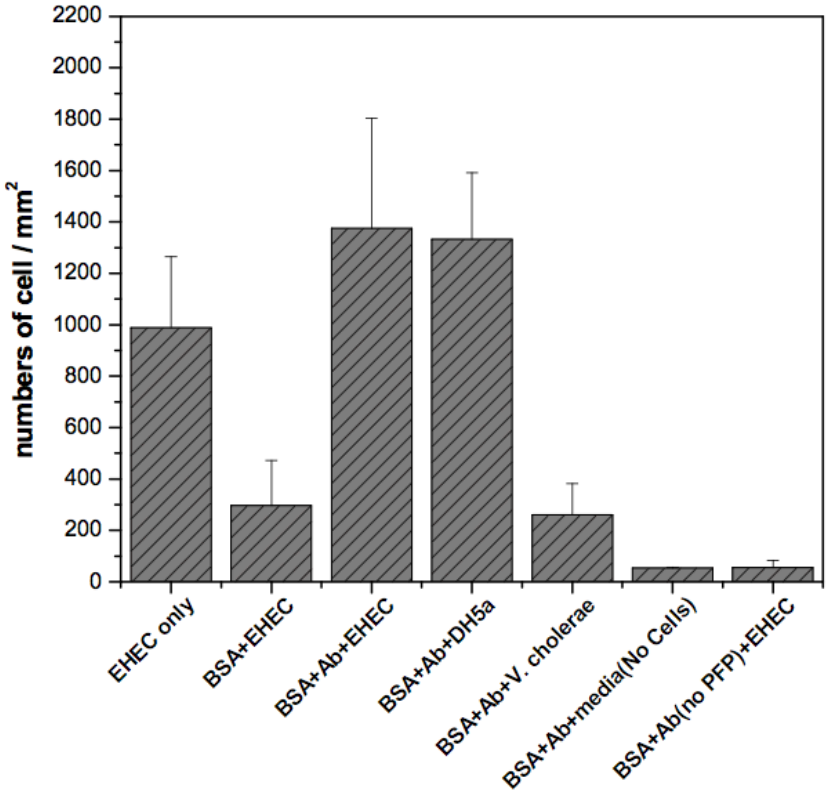

Figure A.7 Cell counting from scattered microscope images. The assessment of antibody attachment to BSA layer was verified by larger numbers of EHEC and DH5α than *V. cholerae* counted on scattering images. The cell count from the media control sample is due to other particulate scattering centers.

A.5 Conclusions

The incorporation of an antifouling layer that reduces nonspecific binding on the surface of oxidized porous Si has been demonstrated. The layer can be modified with covalent linkers to attach antibodies for specific bacteria detection. Bacterial adhesion on modified porous Si photonic crystals can be determined and quantified by the amount of light scattered from cells resident on the structures. This approach provides useful information on the effectiveness of antifouling and antimicrobial coatings important for various bioassays, including water quality monitoring. Both microscope images and scattering spectra were analyzed and showed similar results. On oxidized porous Si, EHEC cells attach more effectively to an uncoated surface than to a BSA-coated surface. Cell attachment was quantified by measurement of the intensity of photonic peaks in the scattered light spectra, and the method was confirmed using conventional cell counting methods employing optical microscopy. When an *E. coli* specific antibody is attached to the BSA coating, a higher intensity of scattered light is measured from samples incubated with *E. coli* strains relative to samples incubated with *V. cholerae.* A limitation of this scattering method is that other scattering centers of similar size to bacteria, such as dust particles, may introduce significant error in the analysis. Thus, a proper reference, media control sample, should be used to normalize the data. The integration of the scattering technique, the tunable porous Si nanostructure, and the corresponding optical properties should allow the realization of multiparametric assays in which a distinct optical reflectivity spectrum is coupled to a different biorecognition element.

Appendix A, in part, is a reprint (with co-author permission) of the material as it appears in the following publication: Wu, C.; Alvarez, S.; Rang, C.; Chao, L; Sailor, M. J., Label-free Optical Detection of Bacteria on a 1-D Photonic Crystal of Porous Silicon. *Proceeding of the SPIE,* 2009, 71670Z. The author of this dissertation is the primary author of this manuscript.

APPENDIX B

CARBON/POROUS SILICON COMPOSITE RUGATE FILTER-BASED SENSOR AS AN END-OF-SERVICE LIFE INDICATOR

B.1 Abstract

Suitability of carbon/porous silicon composite rugate filter for detection of toluene vapor with presence of water vapor is evaluated. The modulated porosity prepared in the porous silicon provided a mean for optical detection of vapor sensing. Carbon coated surface mimics the activated carbon for adsorption of chemical species. Higher affinity towards toluene vapor compared to water vapor was observed as expected with strong interaction between hydrophobic carbon surface and nonpolar analyte. In the dosing of toluene vapor at varied relative humidity, sensor responded to similar peak shift though not complete eliminate the water adsorption. For the sensor pre-conditioned with water vapor, sensors were not saturated from the pretreatment and additional optical signal change was observed upon introduction of toluene vapor. The miniaturization capability of this carbon/porous silicon composite flake has potential to be integrated into carbon cartridge as an end-of-service life indicator. A simulation of breakthrough experiment with carbon/porous silicon composite flake mounted to optical fiber was demonstrated.

B.2 Introduction

In realistic scenarios of respiratory protection, water is a commonly seen interfering molecule present in large concentrations relative to analyte of interest. Presence of water molecules from the flowing air or water pre-adsorbed to the gas-mask filter during previous exposures has shown to reduce the efficacy of the gas-mask filter against physically adsorbed toxic vapors.[190] Despite the urgent need of end-of-service

life indicators for filtration packs to improve the safety of gas mask users, there is a lack of capable sensors in the market to perform such a task. Chemiresistors are commonly used in gas sensing for their low-cost and ease of operation. However, its detection mechanism, which the metal oxides change their electrical resistance by the presence of chemical species, has limited its use in high humidity environment that it generally gives large signal towards moisture compared to hydrocarbon molecules.[191] In order to discriminate water interference from the signal of target molecules on the sensor, which is the main challenge faced in practical environmental setting, various strategies to eliminate the effects of this non-specific interaction have been proposed. Integration of a hygrometer into a sensor system is proposed for correcting interfering signal from water vapor. However, this may limit the miniaturization capability that is key for personal protection equipment. Built-in discrimination function onto the sensing element is desired for its potential in miniaturization. Ruminski et al. developed a double-stacked porous silicon layer with tailored surface chemistries of each stack which provided a means to correct humidity response.[102] A colloidal metal-insulator-metal ensemble chemiresistor using an octanethiol monolayer coating was demonstrated to have negligible response towards water.[192]

Miniaturization of the sensor component capable of pre-concentration, signal transducer, and integration into portable analytical instruments are highly desired. Optical fibers with a diameter of a few tens to hundreds of microns have been widely studied and used as small remote sensors.[193, 194] Caron et al. demonstrated a porous glass optical fiber sensor as an end-of-service life indicator for respirator cartridges by monitoring the decrease in transmittance intensity as the sensor was saturated by

analyte.[195, 196] King et al. proposed optical-fiber-mounted porous silicon photonic crystals for sensing of organic vapor breakthrough in simulated activated carbon chamber with sensitivity down to 50 ppmv for isopropanol.[195]

The concept of surface chemistry, porosity, molecular interaction, diffusion, and optics as it is studied in the porous silicon system has shown its potential for use in environmental sensing.[4, 5, 197] One major attractive feature of porous silicon is its dual role as both sensor and transducer in one unit which has potential to be miniaturized for in-field applications. The high surface area of porous silicon (few hundreds m^2/g) provides adequate binding sites for the adsorption of target molecules; the optical property originated from its nanostructure enables an effective transduction of the molecular binding events into a macroscopically detectable signal in optical spectrum shift. Demonstration of this "smart dust" on optical fibers has shown its potential to extend to the concept of sensor arrays to target a wide variety of vapor analytes.[195] Surface modifications not only passivate the porous silicon to avoid signal drift for long-term sensing application, but also provide selectivity or affinity towards specific molecules. The effect of surface chemistry on stability and specificity of porous silicon-based optical microsensors were studied previously and sensitivity to analytes was found to highly dependent on surface energy.[198] The hydrophilic surface displays greater response towards polar molecules such as isopropanol while hydrophobic surface respondes better against non-polar compounds such as heptane. For the development of porous silicon-based gas sensor for end-of-service life application, we proposed a surface chemistry similar to adjacent activated carbon bed would give similar adsorption behavior with little to no time delay as adsorption of target molecule

occurs.

In this work, we prepared a carbon/porous silicon composite film to mimic the surface of activated carbon used in respiratory cartridges. Previous study on this composite material has shown stronger adsorption of organic vapor compared to an oxidized surface and its optical property provides a way for signal transduction.[199] The adsorption of nonpolar hydrocarbons to the carbon surface is a strong interaction that is mainly due to the dispersive forces between the solid and the hydrocarbon chain or chain segments; whereas the water adsorption on carbon is dominated by hydrogen-bonding force and is a weaker interaction.[200] We hypothesize such carbon coating on porous Si surface can provide higher affinity towards the hydrocarbon molecules and discriminate from water adsorption. To evaluate the suitability of porous Si based sensor for end-of-service life indicator, the sensor response to relative humidity (RH) both prior and during the exposure to toxic vapors are of prime interest and studied here.

B.3 Experimental Methods

B.3.1 Preparation of Carbon/Porous Silicon Composite Thin Films

Mesoporous silicon thin film was prepared from electrochemical etching of a highly doped p-type silicon wafer (R=0.9-1.0 mΩ cm, Siltronix Corp.) in a 3:1 aqueous 48% HF: ethanol (v/v) solution. A sinusoidally varying current density between 10-100 mA/cm^2 was controlled by computer (LabVIEW, National Instruments Corp.) and applied during the etching, yielding a rugate filter of 24.1 ± 0.1 μm in thickness with a

reflectivity peak in a visible wavelength of the optical spectrum. Surface modification of carbon coverage was achieved using the method described previously.[199] The freshly etched porous Si film was partially oxidized under a stream of ozone gas (Ozone Solutions, Model VMUS-4S, AZCO Industries Ltd) at 1.5 SCFH for 20 minutes. The remaining pore volume was then filled with a solution of 5 mg/mL oxalic acid (ACS grade, EMD Chemicals) in furfuryl alcohol (98%, Aldrich). Upon heating to 70 °C in a furnace (Thermo Scientific, Model FD1545M) for 16 h, the furfuryl alcohol underwent an acid-catalyzed thermal polymerization process, yielding a poly(furfuryl alcohol) (PFA) infiltrated porous silicon film. The PFA-porous silicon composite was then heated to 700 °C (ramp rate: 10 °C/min) under a flow of nitrogen (1 SLPM) for 5 h to produce the carbon-modified porous silicon film. For the freestanding carbon/porous silicon composites, a thicker porous silicon film, 48.1 ± 0.1 μm, was etched and it underwent a partial lift off as furfuryl alcohol evaporates. The rest ot the heating steps were the same as described above. After the heating treatment, the partially lift-off composite film was then mechanically fractured into desired dimension for later integration into optical fibers.

B.3.2 Characterization of Carbon/Porous Si Composite Films

Pore morphology of carbon/porous silicon composite film was characterized using a FEI SFEG Ultra High Resolution (UHR) scanning electron microscopy (SEM) operating in secondary electron mode with an accelerating voltage of 5 keV. The plan-

view and cross-sectional images of the composite films were examined to determine pore dimension and thickness of the film.

The reflectance spectra of carbon/porous silicon composite film were obtained in a 180 degree reflectance configuration, collected using an Ocean Optics USB4000 spectrometer coupled to a bifurcated fiber optic cable. An unpolarized tungsten halogen (Ocean Optics LS-1) light source was focused onto the composite film in specular reflection with a spot size of approximately 1 mm^2. Optical spectra were processed using a computer and algorithms described previously[19] in which a Gaussian fit was applied to the reflectivity spectrum to determine the peak position and monitoring peak shift upon analyte dosing.

B.3.3 Vapor Dosing Experiments

Detection of vapor mixtures which consisted of various concentrations of toluene and water vapor were carried out using a computer-controlled gas dosing system. Sensor responses to the single analyte of toluene and water vapor were conducted separately to characterize affinity of carbon/porous silicon towards an individual vapor. Nitrogen carrier gas was set to a flow rate of 1 L/min using a mass flow controller (MC 1SLPM, Alicat Scientific, Inc.) The various air humidity levels were achieved by diverting a portion of the total nitrogen stream with a separate mass flow controller through the humidifier, and then combining it with the main stream. Both mass flow controllers were controlled by LabView (National Instruments) software. The humidifier consisted of two bubblers half-filled with distilled water and

adjusting the flow rate of the nitrogen stream flow through the humidifier controlled the designed relative humidity levels. The final relative humidity was measured by a relative humidity detector (HIH-4010-002, Honeywell Sensing and Control, Inc.) positioned in the mixer flask before the inlet of the flow cell chamber. For the controlled concentration of toluene vapor, liquid toluene was pumped at a constant and consistent flow rate with a low-volume liquid handling pump (M6, Valco Instruments Co. Inc.) and injected into a brass block heated to 110 °C. The toluene vapor in humidified nitrogen carrier gas was first directed through a 1 L flask mixer for thoroughly mixing and then delivered to a custom built Teflon flow cell containing the carbon/porous silicon chip with a copper back plate and a transparent glass window on top for optical probing. The optical responses of carbon/porous silicon chip were captured by a CCD spectrometer (USB4000, Ocean Optics, Inc.). Toluene concentrations were validated with a gas chromatograph (SRI Instruments 8610C with FID detector) positioned at the downstream. After each concentration run, the composite film was heated to 110 °C for at least 20 min to repel previously adsorbed toluene and allowed to cool to room temperature prior further dosing. A resistive heater (Minco Products, Inc.) and a K-type thermocouple (Omega Engineering, Inc.) were used to control the heat refresh process. For the carbon/porous silicon composite films exposed to water vapor, the heat treatment was not sufficient to regenerate the sensor back to previous baseline in optical spectrum, therefore these chips were used one-time only.

B.3.4 Construction of Freestanding Composite Film with Optical Fibers for Remote Sensing

Freestanding carbon/porous silicon composite films were mounted to optical fibers (600 micron silica core, low OH) for remote sensing by physical attachment. The freestanding carbon/porous silicon composite flake was prepared from ~48 μm porous silicon layer that was partially lifted off from the bulk Si substrate after infiltration of 5 mg/mL oxalic acid in furfuryl alcohol. After carbonization treatment at 700 °C for 5 h, the freestanding carbon/porous silicon particle was attached to the polyether ether ketone (PEEK) tubing by electrotatic force after rubbing PEEK tubing on a glass slide. A porous stainless steel cap was used to hold the particle against the PEEK tubing; the optical fiber was then slide into the PEEK tubing and fixed with heat-shrink tubing. The sub-micron sized composite film was sandwitched between the distal end of optical fiber and a porous stainless steel cap. The physical mounting process produces no significant change in reflectivity spectrum relative to the original chip-based sensor. Optical fiber was cleaved to a desired length, stripped partially of the outer cladding layer, and polished on aluminum oxide lapping film to provide a smooth tip for optical light coupling.

B.3.5 Remote Sensing Application: Detection of Analyte Breakthrough with Activated carbon Respiratory Cartridge

The detection of toluene vapor breakthrough in an activated carbon respiratory cartridge simulator was demonstrated in a bench-scale experimental system. A

simulator chamber was constructed to hold a powered air purifying respirator which used three commercially available carbon cartridges. One of the cartridges contained a sample port at the mid bed for inserting an optical fiber with a sensor element mounted at the tip using the method described previously. A probe for conventional gas chromatography (GC) (8610C, SRI Instruments, Scientific Repair, Inc.) was placed at the outlet of the chamber to determine the breakthrough time of toluene vapor. The entire assembly was placed in a Plexiglass container to hold the controlled humidity and toluene concentrations. Airflow was set at 32 L/min using an air conditioning system with adjustable relative humidity (HCS-401, Miller-Nelson Instruments, a unit of Assay Technology, Inc.). Toluene vapor at a desired concentration was controlled by injecting liquid toluene with a low-volume liquid flow pump as previous described.

B.4 Results and Discussion

B.4.1 Preparation and Characterization of Carbon/Porous Si Rugate Filter

Porous silicon prepared from electrochemical etching with a time-varying current gives a sharp peak in reflectivity spectrum which is categorized as a rugate filter.[23] The layered structure acts as a one-dimensional photonic crystal, displaying a peak in the reflectance spectrum whose wavelength is determined by the periodicity of modulated sinusoidal current and the refractive index of the porous layer. The carbon deposition on porous silicon rugate filters have a higher affinity towards nonpolar analytes as reported in the previous described method.[199] The freshly etched porous silicon was first oxidized in a stream of ozone to enhance the adsorption of furfuryl

alcohol. The *in situ* polymerization of furfuryl alcohol yields a resin-infiltrated film that was later carbonized at 700 °C for 5 h. Figure B.1 (A) shows the pore morphology of carbon/porous silicon composite film with pore size 7.3 ± 1.6 nm. The film thickness of composite film was assessed by cross-section SEM image, Figure B.1 (B). Differing intensities bands shown in inset of Figure B.1 (B) were due to modulated porosity variation from the sinusoidal waveform applied during the etching process.

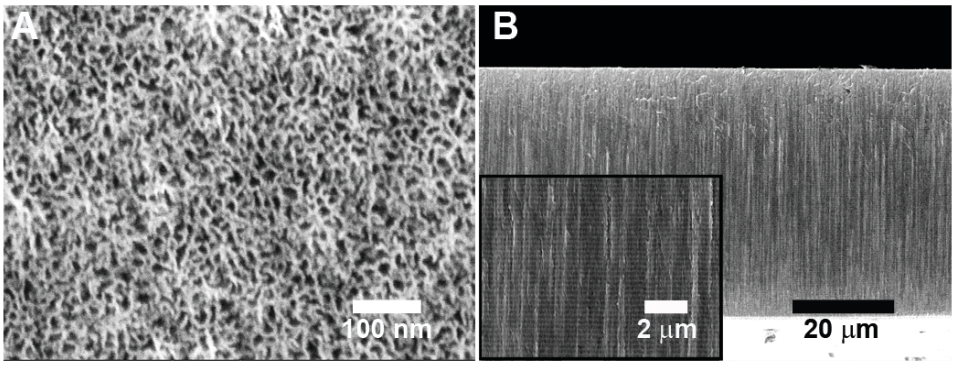

Figure B.1 Scanning electron microscopy images of carbon/porous silicon composite thin film. (A) Plan-view of carbon/porous silicon thin film. (B) Cross-section of the composite thin film; the banned structure of the original rugate is visible in the higher magnification (inset).

B.4.2 Optical Monitoring of Sensing Event with Composite Films

The flow cell setup for carbon/porous silicon composite film exposed to vapor is illustrated in the inset of Figure B.2 (A). The adsorption event could be monitored by optical reflection spectroscopy. As analyte (toluene and/or water vapor) replaces nitrogen in the porous matrix, the change in local refractive index results in a shift in reflectivity peak. The relation between the effective refractive index (n_{eff}) of the porous matrix and the thickness of one period repeat layer in the rugate structure (d, nm) can be expressed in the Equation B.1:

$$\lambda = 2n_{eff}d \qquad \text{(B.1)}$$

The peak position was experimentally determined by a Gaussian fit to the reflectivity peak. The sensor response was measured by the difference between peak position (λ') in the presence of analyte relative to its value in pure nitrogen (λ_0) according to the Equation B.2:

$$\Delta\lambda = \lambda' - \lambda_0 \qquad \text{(B.2)}$$

The shift of reflectance peak position is correlated to refractive index change associated with replacing nitrogen with toluene or water vapor and therefore is concentration dependent (Figure B.2 (B)). The analyte concentrations were introduced sequentially. Between each run of toluene exposure, a nitrogen purge and thermal heating were used to refresh the sensor back to initial baseline. As shown in Figure B.2 (B), the composite sensor is capable for detecting toluene vapor at lower concentrations than the permissible exposure limits in time-weighed average of 200 ppmv published by Occupational Safety and Health Administration.[201]

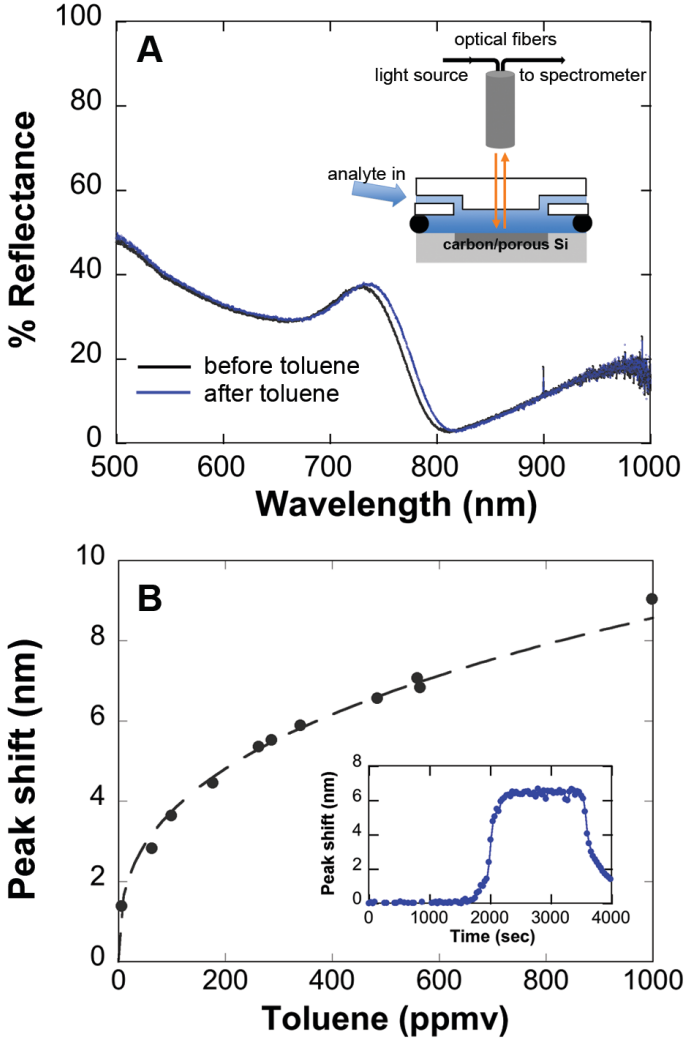

Figure B.2 Quantification of toluene exposure on carbon/porous silicon rugate filter using optical measurement. (A) Reflectance spectra of the carbon/ porous Si composite rugate before and after 400 nm toluene exposure. Inset shows the schematic optical spectrum acquisition from a sensor exposed to a stream of toluene vapor; the spectrum was corrected with a polished silicon wafer. (B) Typical dose-response curve of toluene vapor at 0% RH on carbon/porous silicon film. The wavelength of the reflectivity peak was monitored as a function of time as the composite film exposed to pure nitrogen carrier gas, the toluene vapor in nitrogen, and purged again with pure nitrogen, as shown in the inset. All the on-chip measurements were performed with 24.0 μm-thick carbon/porous silicon composite film.

B.4.3. Effect of Humidity on Sensor Response to Organic Vapor

The fundamental principle in optical detection in porous silicon relies on the change of refractive index as analytes, and/or interfering water molecules, replaces previous nitrogen molecules. Response of carbon/porous silicon composite film to water vapor is shown in Figure B.3 (A). The shift in wavelength after reaching the plateau was found to be in linear correlation with the increased relative humidity (RH) up to 80% RH. The carbon/porous Si composite prepared in this study could not completely exclude the adsorption of water molecules onto the surface and therefore contribute to the observed shifts in optical spectra.

To study the sensor response to toluene with presence of water vapor, two types of experimental conditions were performed: (1) toluene vapor with water vapor introduced at the same time; (2) water vapor pre-condition followed toluene vapor with the same water content. These two schemes were to mimic the real exposure conditions where the sensor and carbon cartridge may pre-adsorb water vapor during the storage or from previous exposures. The sensor responses to 500 ppm toluene and varied relative humidity (Figure B.3 (C)(D)) show similar responses in wavelength shift, suggesting the toluene concentration dominated the sensor responses, which is consistent with stronger interaction between carbonaceous surface and toluene vapors. It is worth noted that water vapor-exposed composite films could not be regenerated with thermal heating procedure described previously. Therefore, separate carbon/porous silicon composite films for water vapor sensing were used one-time only for this set of data. This may attribute to the slight variation in sensor responses shown in Figure B.3 (D).

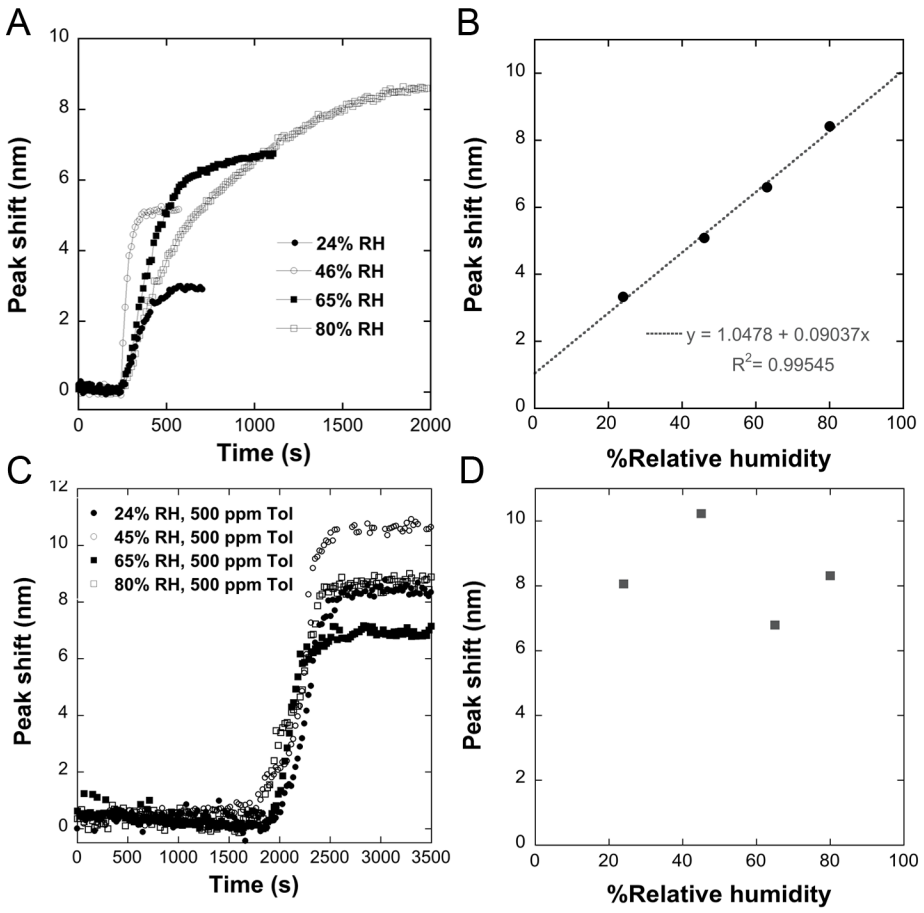

Figure B.3 Carbon/porous silicon interaction with water vapor alone and toluene/water vapor concurrently. (A) Dose-response curves of carbon/porous silicon composite films against varied relative humidity environment. (B) Correlation of sensor response to relative humidity. (C) Carbon/porous silicon composite film challenged with 500 ppm toluene at varied relative humidity. (D) Sensor responses correlation with 500 ppm toluene at varied relative humidity. Note. Water vapor-exposed composite films could not be regenerated with thermal heating procedure described previously. Separate carbon/porous Si composite films for water vapor sensing were used one-time only for this set of data.

A second scenario is when sensor pre-adsorb water vapor, equilibrate with relative humidity, and followed toluene challenges. Two relative humidity was chosen for this study, 45% and 80% RH. The water pre-condition experiments were performed by first exposing the carbon/porous Si composite films to a constant nitrogen stream with fixed relative humidity. After the sensor response curve reached plateau, toluene vapor of 490 ppm were then introduced into the humidified stream under the same RH. As shown in Figure B.4, additional red shifts in reflectivity peak were observed as toluene introduced into the humidified stream for both 45% and 80% RH pre-conditioned composite films. The refractive index for toluene is 1.4941 (25 °C, 589 nm) and 1.333 for water. The additional red shift indicates adsorption of toluene occurs. This can be explained by co-adsorption of two immiscible components[202] in which toluene vapor is adsorbed in the micropore volume left free by water. The sensor pre-conditioned with 45% RH shows an additional 5.9 nm peak shift in optical response compared to an additional peak shift of 5.3 nm from the sensor pre-conditioned with 80% RH. The similar degree of peak shift suggests that the high surface area of carbon/porous silicon film (309 m^2/g) provides sufficient binding sites for toluene vapor to adsorb that it is not saturated from previous exposed water vapor even up to 80% RH. We could not exclude the possibility that displacement may take place where water molecules are replaced by the toluene molecules given the greater interaction between carbonaceous surface and non-polar molecules.

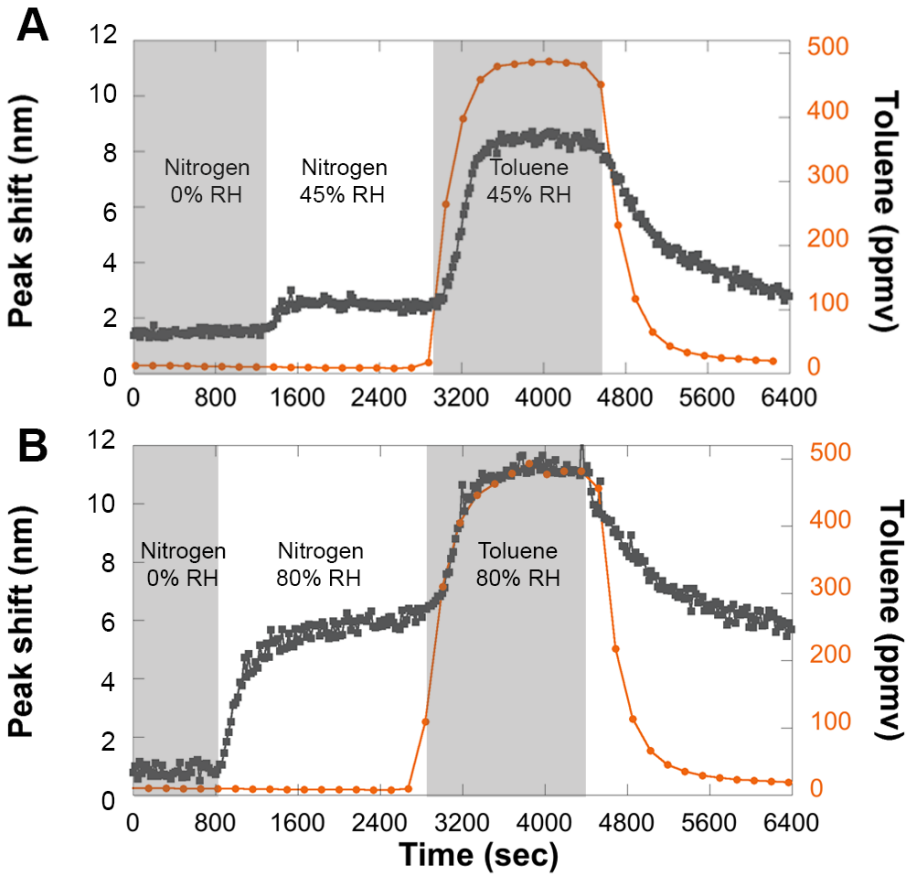

Figure B.4 Water vapor pre-conditioned carbon/porous silicon composite film followed toluene vapor challenge under the same conditioned relative humidity. (A) Sample exposed to 490 ppm toluene vapor after pre-conditioning with 45% RH; (B) sample exposed to 490 ppm toluene vapor after pre-conditioning with 80% RH. The grey traces depicted the time-resolved sensor response where the orange traces indicated the concentration of toluene quantified with the gas chromagraph positioned at downstream.

B.4.4. Demonstration of Miniaturized Sensor in Breakthrough of Carbon Respiratory Cartridges

With the established sensing capability of carbon/porous silicon composite film demonstrated above, we further miniaturized the sensing element by attaching the sub-micron composite flake to the distal end of the optical fiber. A breakthrough experiment on the carbon respiratory cartridges was then conducted for evaluation. The principle for implementing the sensor element is to position sensors at different positions in the activated carbon bed to indicate the capacity left for respiratory protection. In this experiment, the sensor element was placed at the mid bed of the cartridge and therefore approximately half of the breakthrough time was expected to be observed from sensor response. The breakthrough with challenging toluene vapor were determined by a GC probe positioned at the outlet of the carbon cartridge. Construction of miniaturized sensing element to be integrated into carbon cartridge is shown in Figure B. 5. This miniaturized device was integrated into a respiratory cartridge simulator for breakthrough experiment (Figure B. 6).

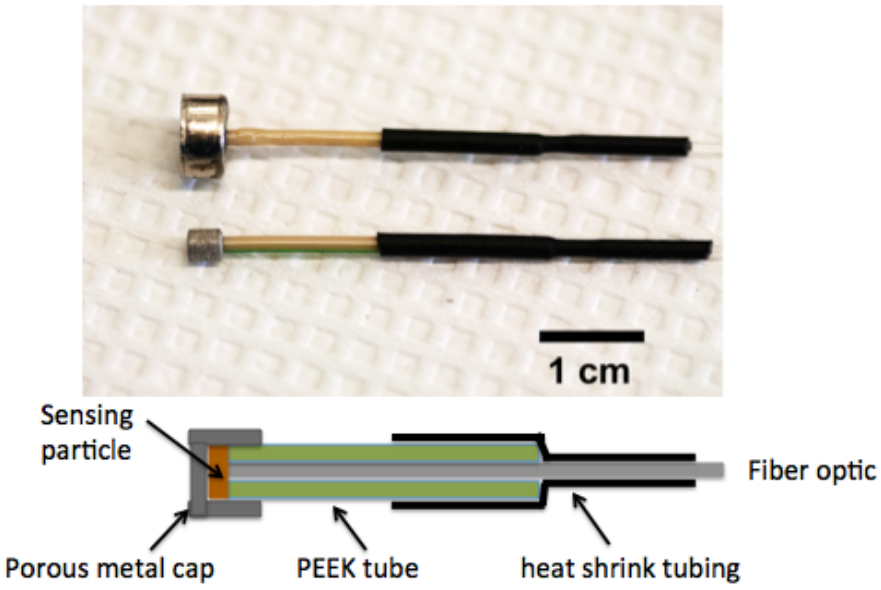

Figure B.5 An optical fiber-mounted carbon/porous Si composite film. The carbon/porous silicon composite flake was mechanically held in place by the porous metal cap surrounded it while accessible to vapor analyte and a fiber optic to transduce light signal. A bifurcated cable was attached to the other end of optical fiber, with one end coupled to an unpolarized light source and the other end to a CCD-based detector.

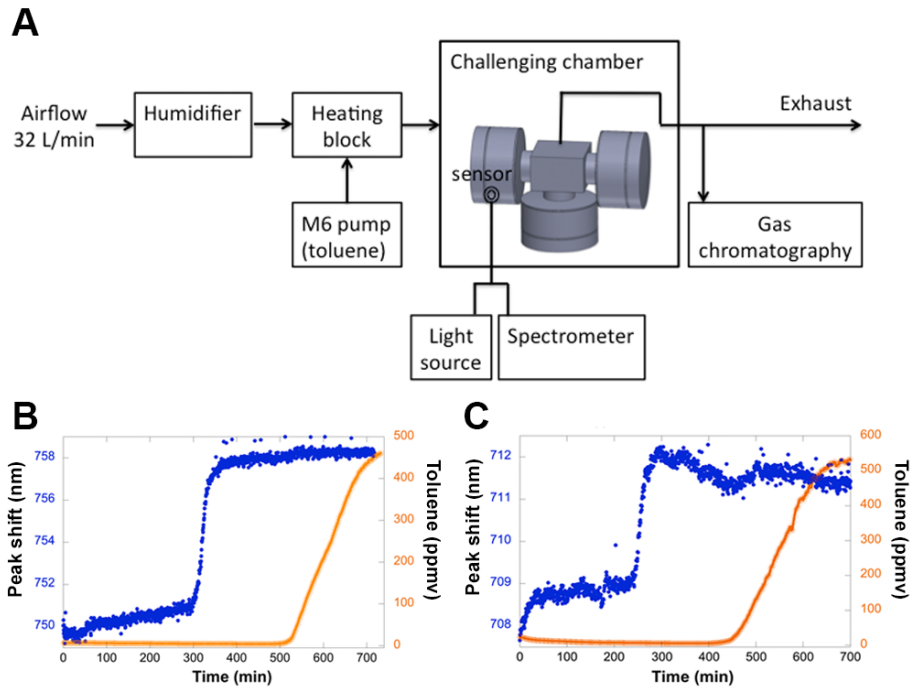

Figure B.6 Respirator cartridge simulator for the breakthrough experiments with carbon/porous silicon sensor. (A) Schematic flow of the breakthrough experiment conducted to evaluate sensor response. The flow chamber was made of Plexiglas to confine challenging gas and to hold a powered air purifying respirator with three carbon cartridges. An optical fiber-mounted carbon/porous silicon sensor was placed at midpoint in the bed of one of the carbon cartridge and a GC probe was placed at the outlet to determine breakthrough of challenging gas. (B) Response of carbon/porous silicon composite sensor in breakthrough experiment with 20% RH and (C) 65% RH. Vapor breakthrough was monitored by GC probe (right y-axis) at the outlet of the chamber and by fiber-mounted carbon/porous silicon sensor (left y-axis). Optical sensors data points were obtained every 20 s. GC data points were obtained every 4 min. A stream of 500 ppmv toluene vapor flow with predetermined humidity was initiated at time=0 in a carrier gas.

Detection of the toluene vapor in air containing humidity using a sub-micron carbon/porous silicon-based sensor elements was demonstrated. Figure B. 6 (B) and (C) displayed the response of a carbon/porous silicon composite film to the challenging toluene gas ~500 ppmv with 20% and 65% RH. As expected, higher humidity shortened the breakthrough time determined by the GC from 510 min (20% RH) to 420 min (65% RH), as indicated by black arrow on orange traces. Slow red shifts in the sensor responses were correlated to the humidity that pass through first, and instant change occurred approximately 60% of breakthrough time, indicating the detection of toluene vapor and is position dependent. Results show the detection of toluene vapor was not overwhelmed by the presence of water vapor and the position where sensor was placed can be used for indicating remaining capacity left in the carbon cartridge.

B. 5 Conclusions

A carbon/porous silicon composite thin film was evaluated for the detection of toluene vapor with the presence of humidity. This carbon-abundant surface mimics the activated carbon surface and provides high affinity towards toluene vapor over water vapor although not completely eliminating the adsorption of water vapor. Sensor response to toluene vapor of 500 ppmv was not overwhelmed by the presence of water vapor even up to 80% RH. Samples pre-conditioned with water vapor followed by a challenge gas of 500 ppmv toluene vapor under the same level of humidity showed addition shift in optical spectra that the sensitivity was not lost by previous adsorbed water molecules. A miniaturized carbon/porous silicon sensor as an end-of-service life

indicator to provide information about the remaining capacity was demonstrated in a respirator cartridge simulator. Proper positioning of the sensor element in the carbon cartridge allows for early indication on residual capacity left in cartridge for protection from non-polar analytes. Future investigations to characterize the carbon/porous silicon sensor response to other type of volatile organic compounds and in the mixture of challenging gas would be important for evaluating its performance in real environmental setting.

Appendix B, in part or in full, is a reprint (with co-author permission) of the material as it appears in the following publication: Wu, C.; Chan, D.; Snyder, J. L.; Sailor, M. J., Carbon/porous Si Composite Rugate Filter-based Sensor As An End-of-Service Life Indicator. Manuscript in preparation. The author of this dissertation is the primary author of this manuscript.

References

1. Uhlir, A., Electrolytic Shaping of Germanium and Silicon. *Bell System Tech. J.* **1956,** *35*, 333-347.

2. Canham, L. T., Si Quantum Wire Array Fabrication by Electrochemical and Chemical Dissolution. *Appl. Phys. Lett.* **1990,** *57*, 1046-1048.

3. Lehmann, V.; Gosele, U., Porous Silicon Formation: a Quantum Wire Effect. *Appl. Phys. Lett.* **1991,** *58*, 856-858.

4. Snow, P. A.; Squire, E. K.; Russell, P. S. J., et al., Vapor Sensing using the Optical Properties of Porous Silicon Bragg Mirrors. *J. Appl. Phys.* **1999,** *86*, 1781-1784.

5. Lauerhaas, J. M.; Credo, G. M.; Heinrich, J. L., et al., Reversible Luminescence Quenching of Porous Silicon by Solvents. *J. Am. Chem. Soc.* **1992,** *114*, 1911-1912.

6. Sohn, J.; Letant, S.; Sailor, M. J., et al., Detection of Fluorophosphonate Chemical Warefare Agents by Catalytic Hydrolysis with a Porous Silicon Interferometer. *J. Am. Chem. Soc.* **2000,** *122*, 5399-5400.

7. Content, S.; Trogler, W. C.; Sailor, M. J., Detection of Nitrobenzene, DNT and TNT Vapors by Quenching of Porous Silicon Photoluminescence. *Chem. Europ. J.* **2000,** *6*, 2205-2213.

8. Janshoff, A.; Dancil, K.-P. S.; Steinem, C., et al., Macroporous p-Type Silicon Fabry-Perot Layers. Fabrication, Characterization, and Application in Biosensing. *J. Am. Chem. Soc.* **1998,** *120*, 12108-12116.

9. Chan, S.; Fauchet, P. M.; Li, Y., et al., Porous Silicon Microcavities for Biosensing Applications. *physica status solidi (a)* **2000,** *182* (1), 541-546.

10. Letant, S. E.; Hart, B. R.; Kane, S. R., et al., Enzyme Immobilization on Porous Silicon Surfaces. *Adv. Mater.* **2004,** *16*, 689-693.

11. Salonen, J.; Kaukonen, A. M.; Hirvonen, J., et al., Mesoporous Silicon in Drug Delivery Applications. *J. Pharm. Sci.* **2008,** *97* (2), 632-653.

12. Anglin, E. J.; Cheng, L.; Freeman, W. R., et al., Porous Silicon in Drug Delivery Devices and Materials. *Adv. Drug Delivery Rev.* **2008,** *60*, 1266–1277.

13. Canham, L., *Properties of Porous Silicon* Institution of Engineering and Technology: London, 1997; Vol. 18.

14. Zhang, X. G., Morphology and Formation Mechanism of Porous Silicon. *J. Electro. Soc.* **2004,** *151* (1), c69-c80.

15. Buriak, J. M., Organometallic Chemistry on Silicon and Germanium Surfaces. *Chemical Reviews* **2002,** *102* (5), 1271-1308.

16. Berger, M. G.; Arens-Fischer, R.; Thoenissen, M., et al. In *Dielectric Filters Made of Porous Silicon: Advanced Performancce by Oxidation and New Layer Structures*, E-MRS 96 Spring Meeting, Symposium L: New Developments in Porous Silicon: Relation with Other Nanostructure Porous Materials, 1996; pp 237-240.

17. Lin, V. S.-Y.; Motesharei, K.; Dancil, K.-P. S., et al., A Porous Silicon-Based Optical Interferometric Biosensor. *Science* **1997,** *278*, 840-843.

18. Wei, J.; Buriak, J. M.; Siuzdak, G., Desorption-ionization Mass Spectrometry on Porous Silicon. *Nature* **1999,** *399*, 243-246.

19. Sailor, M. J., *Porous Silicon in Practice: Preparation, Characterization, and Applications*. Wiley-VCH: Weinheim, Germany, 2012; p 249.

20. Sing, K. S. W., Reporting Physisorption Data for Gas/Solid Systems with Special Reference to the Determination of Surface Area and Porosity (Provisional). *Pure Appl. Chem.* **1982,** *54*, 2201-2218.

21. Collins, B. E.; Dancil, K.-P.; Abbi, G., et al., Determining Protein Size Using An Electrochemically Machined Pore Gradient in Silicon. *Adv. Funct. Mater.* **2002,** *12*, 187-191.

22. Karlsson, L. M.; Tengvall, P.; Lundström, I., et al., Back-side Etching: A Tool for Making Morphology Gradients in Porous Silicon. *J. Electrochem. Soc.* **2002,** *149*, C648-C652.

23. Berger, M. G.; Arens-Fischer, R.; Thoenissen, M., et al., Dielectric Filters Made of Porous Silicon: Advanced Performance by Oxidation and New Layer Structures. *E-MRS 96 Spring Meeting, Symposium L: New Developments in Porous Silicon: Relation with other Nanostructures Porous Materials* **1997,** *297*, 237-240.

24. Orosco, M. M.; Pacholski, C.; Sailor, M. J., Real-Time Monitoring of Enzyme Activity in a Mesoporous Silicon Double Laye. *Nature Nanotech*. **2009,** *4*, 255-258.

25. Pacholski, C.; Sartor, M.; Sailor, M. J., et al., Biosensing using Porous Silicon Double-Layer Interfereometers:Reflective Interferometric Fourier Transform Spectroscopy. *J. Am. Chem. Soc*. **2005,** *127*, 11636-11645.

26. Cunin, F.; Schmedake, T. A.; Link, J. R., et al., Biomolecular Screening with Encoded Porous Silicon Photonic Crystals. *Nature Mater*. **2002,** *1*, 39-41.

27. Quyang, H.; Chrostophersen, M.; Viard, R., et al., Macroporous Silicon Microcavities for Macromolecule Detection. *Adv. Funct. Mater*. **2005,** *15*, 1851-1859.

28. Pacholski, C.; Yu, C.; Miskelly, G. M., et al., Reflective Interferometric Fourier Transform Spectroscopy: A Self-Compensating Label-Free Immunosensor Using Double-layers of Porous SiO2. *J. Am. Chem. Soc*. **2006,** *128*, 4250-4252.

29. Schwartz, M. P.; Alvarez, S. D.; Sailor, M. J., A Porous SiO2 Interferometric Biosensor for Quantitative Determination of Protein Interactions: Binding of Protein A to Immunoglobulins Derived from Different Species. *Anal. Chem*. **2007,** *79*, 327-334.

30. Petrova-Koch, V.; Muschik, T.; Kux, A., et al., Rapid-Therml-Oxidized Porous Si-The Superior Photoluminescent Si. *Applied Physics Letters* **1992,** *61* (8), 943-945.

31. Song, J. H.; Sailor, M. J., Dimethyl Sulfoxide as a Mild Oxidizing Agent for Porous Silicon and Its Effect on Photoluminescence. *Inorganic Chemistry* **1998,** *37* (13), 3355-3360.

32. Andrew, J. S.; Anglin, E. J.; Wu, E. C., et al., Sustained Release of a Monoclonal Antibody from Electrochemically Prepared Mesoporous Silicon Oxide. *Adv. Funct. Mater*. **2010,** *20*, 4168–4174.

33. Chen, M. Y.; Sailor, M. J., Charge-Gated Transport of Proteins in Nanostructured Optical Films of Mesoporous Silica. *Anal. Chem*. **2011,** *83*, 7186-7193.

34. Dancil, K.-P. S.; Greiner, D. P.; Sailor, M. J., A Porous Silicon Optical Biosensor: Detection of Reversible Binding of IgG to a Protein A-Modified Surface. *J. Am. Chem. Soc*. **1999,** *121*, 7925-7930.

35. Wu, E. C.; Andrew, J. S.; Buyanin, A., et al., Suitability of Porous Silicon Microparticles for the Long-Term Delivery of Redox-Active Therapeutics. *Chem. Commun.* **2011,** *47*, 5699–5701.

36. Sung, M. M.; Kluth, G. J.; Yauw, O. W., et al., Thermal Behavior of Alkyl Monolayers on Silicon Surfaces. *Langmuir* **1997,** *13*, 6164-6168.

37. Linford, M. R.; Chidsey, C. E. D., Alkyl Monolayers Covalently Bonded to Silicon Surfaces. *L. Am. Chem. Soc.* **1993,** *115* (26), 12631-12632.

38. Terry, J.; Linford, M. R.; Wigren, C., et al., Determination of the Bonding of Alkyl Monolayers to the Si(111) Surface Using Chemical-shift, Scanned-energy Photoelectron Diffraction. *Appl. Phys. Lett.* **1997,** *71*, 1056-1058.

39. Terry, J.; Mo, R.; Wigren, C., et al., Reactivity of the H-Si (1 1 1) surface. *Nucl. Instrum. Methods Phys. Res., Sect. B* **1997,** *133*, 94-101.

40. Gurtner, C.; Wun, A. W.; Sailor, M. J., Surface Modification of Porous Silicon by Electrochemical Reduction of Organo Halides. *Angew. Chem. Int. Ed.* **1999,** *38* (13/14), 1966-1968.

41. Lees, I. N.; Lin, H.; Canaria, C. A., et al., Chemical Stability of Porous Silicon Surfaces Electrochemically Modified with Functional Alkyl Species. *Langmuir* **2003,** *19*, 9812-9817.

42. Salonen, J.; Bjorkqvist, M.; Laine, E., et al., Stabilization of Porous Silicon Surface by Thermal Decomposition of Acetylene. *Applied Surface Science* **2004,** *225*, 389-394.

43. Kelly, T. L.; Gao, T.; Sailor, M. J., Carbon and Carbon/Silicon Composites Templated in Rugate Filters for the Adsorption and Detection of Organic Vapors. *Adv. Mater. (Weinheim, Ger.)* **2011,** *23*, 1776-1781.

44. Buriak, J. M., Organometallic Chemistry on Silicon Surfaces: Formation of Functional Monolayers Bound Through Si-C Bonds. *Chem. Commun.* **1999,** *12*, 1051-1060.

45. Ruminski, A. M.; King, B. H.; Salonen, J., et al., Porous Silicon-Based Optical Microsensors for Volative Organic Analytes: Effect of Surface Chemsitry on Stability and Specificity. *Adv. Funct. Mater.* **2010,** *20* (17), 2874-2883.

46. Thompson, C. M.; Ruminski, A. M.; Sega, A. G., et al., Preparation and Characterization of Pore-Wall Modification Gradients Generated on Porous Silicon Photonic Crystals Using Diazonium Salts. *Langmuir* **2011,** *27*, 8967–8973.

47. Hook, A. L.; Thissen, H.; Voelcker, N. H., Surface manipulation of biomolecules for cell microarray applications. *Trends Biotechnol*. **2006,** *24*, 471-477.

48. Fodor, S. P.; Read, J. L.; Pirrung, M. C., et al., Light-directed, Spatially Addressable Parallel Chemical Synthesis. *Science* **1991,** *251*, 767-773.

49. Doan, V. V.; Sailor, M. J., Luminescent Color Image Generation on Porous Si. *Science* **1992,** *256*, 1791-1792.

50. Stewart, M. P.; Buriak, J. M., Photopatterned Hydrosilylation on Porous Silicon. *Angew. Chem., Int. Ed.* **1998,** *37*, 3257-3260.

51. Link, J. R.; Sailor, M. J., Smart Dust: Self-Assembling, Self-Orienting Photonic Crystals of Porous Si. *Proc. Natl. Acad. Sci. U. S. A.* **2003,** *100*, 10607-10610.

52. Jani, A. M. M.; Anglin, E. J.; McInnes, S. J. P., et al., Nanoporous Anodic Aluminium Oxide Membranes with Layered Surface Chemistry. *Chemical Communications* **2009**, 3062-3064.

53. Jani, A. M. M.; Kempson, I. M.; Losic, D., et al., Dressing in Layers: Layering Surface Functionalities in Nanoporous Aluminum Oxide Membranes. *Angew. Chem., Int. Ed.* **2010,** *49*, 7933-7937.

54. Guan, B.; Ciampi, S.; Luais, E., et al., Depth-Resolved Chemical Modification of Porous Silicon by Wavelength-Tuned Irradiation. *Langmuir* **2012,** *28*, 15444-15449.

55. Striemer, C. C.; Gaborski, T. R.; McGrath, J. L., et al., Charge- and Size-based Separation of Macromolecules Using Ultrathin Silicon Membranes. *Nature* **2007,** *445*, 749-753.

56. Gartmann, N.; Brühwiler, D., Controlling and Imaging the Functional-Group Distribution on Mesoporous Silica. *Angew. Chem., Int. Ed.* **2009,** *48*, 6354-6356.

57. Kilian, K. A.; Böcking, T.; Gaus, K., et al., Introducing Distinctly Different Chemical Functionalities onto the Internal and External Surfaces of Mesoporous Materials. *Angew. Chem., Int. Ed.* **2008,** *47*, 2697-2699.

58. Vansant, E. F.; Van Der Voort, P.; Vrancken, K. C., *Characterization and Chemical Modification of the Silica Surface*. Elsevier Science: 1995.

59. Kingshott, P.; Andersson, G.; McArthur, S. L., et al., Surface Modification and Chemical Surface Analysis of Biomaterials. *Curr. Opin. Chem. Biol.* **2011,** *15*, 667-676.

60. Voicu, R.; Boukherroub, R.; Bartzoka, V., et al., Formation, Characterization, and Chemistry of Undecanoic Acid-Terminated Silicon Surfaces: Patterning and Immobilization of DNA. *Langmuir* **2004,** *20* (26), 11713-11720.

61. Orosco, M. M.; Pacholski, C.; Miskelly, G. M., et al., Protein-coated Porous Silicon Photonic Crystals for Amplified Optical Detection of Protease Activity. *Adv. Mater.* **2006,** *18*, 1393-1396.

62. Alvarez, S. D.; Schwartz, M. P.; Migliori, B., et al., Using a Porous Silicon Photonic Crystal for Bacterial Cell-based Biosensing. *Phys. Status Solidi A–Appl. Mater.* **2007,** *204*, 1439–1443.

63. Ziauddin, J.; Sabatini, D. M., Microarrays of Cells Expressing Defined cDNAs. *Nature* **2001,** *411*, 107-110.

64. Cheng, L.; Anglin, E.; Cunin, F., et al., Intravitreal properties of porous silicon photonic crystals: a potential self-reporting intraocular drug delivery vehicle. *Br. J. Ophthalmol.* **2008,** *92*, 705–711.

65. Santos, H. A.; Riikonen, J.; Salonen, J., et al., In vitro Cytotoxicity of Porous Silicon Microparticles: Effect of the Particle Concentration, Surface Chemistry and Size. *Acta Biomater.* **2010,** *6*, 2721-2731.

66. Kilpeläinen, M.; Riikonen, J.; Vlasova, M. A., et al., In vivo Delivery of a Peptide, Ghrelin Antagonist, with Mesoporous Silicon Microparticles. *J. Control. Release* **2009,** *137*, 166-170.

67. Slowing, I.; Trewyn, B. G.; Lin, V. S. Y., Effect of Surface Functionalization of MCM-41-Type Mesoporous Silica Nanoparticles on the Endocytosis by Human Cancer Cells. *Journal of the American Chemical Society* **2006,** *128* (46), 14792-14793.

68. Liong, M.; Lu, J.; Kovochich, M., et al., Multifunctional Inorganic Nanoparticles for Imaging, Targeting, and Drug Delivery. *ACS Nano* **2008,** *2* (5), 889-896.

69. Lee, S. B.; Martin, C. R., pH-switchable, Ion-permselective Gold Nanotubule Membrane Based on Chemisorbed Cysteine. *Anal. Chem.* **2001,** *73*, 768-775.

70. Ku, J.-R.; Lai, S.-M.; Ileri, N., et al., pH and Ionic Strength Effects on Amino Acid Transport through Au-Nanotubule Membranes Charged with Self-Assembled Monolayers. *J. Phys. Chem. C* **2007,** *111*, 2965-2973.

71. Kim, E.; Xiong, H.; Striemer, C. C., et al., A Structure-permeability Relationship of Ultrathin Nanoporous Silicon Membrane: A Comparison with the Nuclear Envelope. *J. Am. Chem. Soc.* **2008,** *130*, 4230-4231.

72. Valiullin, R.; Kortunov, P.; Karger, J., et al., Surface self-diffusion of organic molecules adsorbed in porous silicon. *J. Phys. Chem. B* **2005,** *109*, 5746-5752.

73. Velleman, L.; Shearer, C. J.; Ellis, A. V., et al., Fabrication of Self-supporting Porous Silicon Membranes and Tuning Transport Properties by Surface Functionalization. *Nanoscale* **2010,** *2*, 1756-1761.

74. Majumder, M.; Chopra, N.; Hinds, B. J., Mass Transport through Carbon Nanotube Membranes in Three Different Regimes: Ionic Diffusion and Gas and Liquid Flow. *ACS Nano* **2011,** *5*, 3867-3877.

75. Majumder, M.; Chopra, N.; Andrews, R., et al., Nanoscale Hydrodynamics - Enhanced Flow in Carbon Nanotubes. *Nature* **2005,** *438*, 44.

76. Gorris, H. H.; Rissin, D. M.; Walt, D. R., Stochastic Inhibitor Release and Binding from Single-enzyme Molecules. *Proc. Nat. Acad. Sci. U.S.A.* **2007,** *104*, 17680-17685.

77. Konry, T.; Hayman, R. B.; Walt, D. R., Microsphere-Based Rolling Circle Amplification Microarray for the Detection of DNA and Proteins in a Single Assay. *Anal. Chem.* **2009,** *81*, 5777-5782.

78. Steinle, E. D.; Mitchell, D. T.; Wirtz, M., et al., Ion Channel Mimetic Micropore and Nanotube Membrane Sensors. *Anal. Chem.* **2002,** *74*, 2416-2422.

79. Jirage, K. B.; Hulteen, J. C.; Martin, C. R., Effect of Thiol Chemisorption on the Transport Properties of Gold Nanotubule Membranes. *Anal. Chem.* **1999,** *71*, 4913-4918.

80. Chen , W.; Wu, Z.-Q.; Xia, X.-H., et al., Anomalous Diffusion of Electrically Neutral Molecules in Charged Nanochannels. *Angew. Chem., Int. Ed.* **2010,** *49*, 7943-7947.

81. Hutter, T.; Ruschin, S., Non-Imaging Optical Method for Multi-Sensing of Gases Based on Porous Silicon. *Sensor Journal, IEEE* **2010,** *10*, 97-103.

82. Ruminski, A. M.; Barillaro, G.; Chaffin, C., et al., Internally Referenced Remote Sensors for HF and Cl2 Using Reactive Porous Silicon Photonic Crystals. *Advanced Functional Materials* **2011,** *21* (8), 1511-1525.

83. Sweetman, M. J.; Voelcker, N. H., Chemically Patterned Porous Silicon Photonic Crystals towards Internally Referenced Organic Vapour Sensors. *RSC Adv.* **2012,** *2*, 4620-4622.

84. Murguía, J. S.; Vergara, A.; Vargas-Olmos, C., et al., Two-dimensional Wavelet Transform Feature Extraction for Porous Silicon Chemical Sensors. *Anal. Chim. Acta* **2013,** *785*, 1-15.

85. Li, Y. Y.; Kollengode, V. S.; Sailor, M. J., Porous Silicon/polymer Nanocomposite Photonic Crystals by Microdroplet Patterning. *Adv. Mater. (Weinheim, Ger.)* **2005,** *17*, 1249-1251.

86. Kato, Y.; Ito, T.; Hiraki, A., Low temperature oxidation of crystalline porous silicon. *Appl. Surf. Sci.* **1989,** *41/42*, 614-618.

87. Janshoff, A.; Dancil, K.-P. S.; Steinem, C., et al., Macroporous p-Type Silicon Fabry−Perot Layers. Fabrication, Characterization, and Applications in Biosensing. *J. Am. Chem. Soc.* **1998,** *120*, 12108-12116.

88. Yablonovitch, E.; Allara, D. L.; Chang, C. C., et al., Unusually Low Surface-Recombination Velocity on Silicon and Germanium Surfaces. *Phys. Rev. Lett.* **1986,** *57*, 249-252.

89. Ruminski, A. M.; King, B. H.; Salonen, J., et al., Porous silicon-based optical microsensors for volatile organic analytes: effect of surface chemistry on stability and specificity. *Adv. Funct. Mater.* **2010,** *20*, 2874–2883.

90. Hecht, E., *Optics*. 3 ed.; Addison-Wesley: Reading, MA, 1998; p 377-428.

91. Bohren, C. F.; Huffman, D. R., *Adsorption and Scattering of Light by Small Particles*. Wiley: New York, 1983; p 217.

92. Thei, W.; Henkel, S.; Arntzen, M., Connecting Microscopic and Macroscopic Properties of Porous Media: Choosing Appropriate Effective Medium Concepts. *Thin Solid Films* **1995,** *255*, 177-180.

93. Hansch, C.; Leo, A.; Hoekman, D. H., *Exploring QSAR*. American Chemical Society: Washington, DC, 1995; Vol. 1.

94. *ACD/Labs*, version 11.02; Advanced Chemistry Development, Inc.: Toronto, ON, Canada, 2013.

95. Leo, A.; Hansch, C.; Elkins, D., Partition Coefficients and Their Uses. *Chem. Rev. (Washington, DC, U.S.)* **1971,** *71*, 525-616.

96. Israelachvili, J.; Pashley, R., The Hydrophobic Interaction is Long Range, Decaying Exponentially with Distance. *Nature* **1982,** *300*, 341-342.

97. Hato, M., Attractive Forces between Surfaces of Controlled "Hydrophobicity" across Water: A Possible Range of "Hydrophobic Interactions" between Macroscopic Hydrophobic Surfaces across Water. *J. Phys. Chem.* **1996,** *100*, 18530-18538.

98. Unger, K. K.; Kinkel, J. N.; Anspach, B., et al., Evaluation of Advanced Silica Packings for the Separation of Biopolymers by High-Performance Liquid Chromatography : I. Design and Properties of Parent Silicas. *J. Chromatogr., A* **1984,** *296*, 3-14.

99. Mitchell, D. T.; Lee, S. B.; Trofin, L., et al., Smart Nanotubes for Bioseparations and Biocatalysis. *J. Am. Chem. Soc.* **2002,** *124*, 11864-11865.

100. Taguchi, A.; Schüth, F., Ordered Mesoporous Materials in Catalysis. *Microporous Mesoporous Mater.* **2005,** *77*, 1-45.

101. Vallet-Regí, M.; Balas, F.; Arcos, D., Mesoporous Materials for Drug Delivery. *Angew. Chem., Int. Ed.* **2007,** *46*, 7548-7558.

102. Ruminski, A. M.; Moore, M. M.; Sailor, M. J., Humidity-Compensating Sensor for Volatile Organic Compounds Using Stacked Porous Silicon Photonic Crystals. *Adv. Funct. Mater.* **2008,** *18*, 3418-3426.

103. Seo, S.; Lee, J. H.; Cho, Y., et al., Distinctly Different Chemical Functionalities on the Internal and the External Surfaces of Silica Nanotubes, and Their Applications as Multi-Chemosensors. *Chem. – Eur. J.* **2011,** *17*, 7433-7437.

104. Laocharoensuk, R.; Burdick, J.; Wang, J., Carbon-Nanotube-Induced Acceleration of Catalytic Nanomotors. *ACS Nano* **2008,** *2*, 1069-1075.

105. Binks, B. P., Particles as Surfactants-Similarities and Differences. *Curr. Opin. Colloid Interface Sci.* **2002,** *7*, 21-41.

106. Yong, K. T.; Sahoo, Y.; Swihart, M. T., et al., Synthesis and Plasmonic Properties of Silver and Gold Nanoshells on Polystyrene Cores of Different Size and of Gold-Silver Core-Shell Nanostructures. *Colloid Surf. A-Physicochem. Eng. Asp.* **2006,** *290*, 89-105.

107. Shi, W. L.; Sahoo, Y.; Swihart, M. T., et al., Gold Nanoshells on Polystyrene Cores for Control of Surface Plasmon Resonance. *Langmuir* **2005,** *21*, 1610-1617.

108. Hofmeister, H.; Miclea, P.-T.; Morke, W., Metal Nanoparticle Coating of Oxide Nanospheres for Core-Shell Structures. *Part. Part. Syst. Charact.* **2002,** *19*, 359-365.

109. Dabbousi, B. O.; Rodriguez-Viejo, J.; Mikulec, F. V., et al., (CdSe)ZnS Core-Shell Quantum Dots: Synthesis and Characterization of a Size Series of Highly Luminescent Nanocrystallites. *J. Phys. Chem. B* **1997,** *101*, 9463-9475.

110. Cheng, K.; Landry, C. C., Diffusion-Based Deprotection in Mesoporous Materials: A Strategy for Differential Functionalization of Porous Silica Particles. *J. Am. Chem. Soc.* **2007,** *129*, 9674-9685.

111. Buriak, J. M., Organometallic Chemistry on Silicon and Germanium Surfaces. *Chem. Rev. (Washington, DC, U. S.)* **2002,** *102*, 1272-1308.

112. Dorvee, J. R.; Derfus, A. M.; Bhatia, S. N., et al., Manipulation of Liquid Droplets Using Amphiphilic, Magnetic 1-D Photonic Crystal Chaperones. *Nat. Mater.* **2004,** *3*, 896-899.

113. Sailor, M. J.; Wu, E. C., Photoluminescence-Based Sensing with Porous Silicon Films, Microparticles, and Nanoparticles. *Adv. Funct. Mater.* **2009,** *19*, 3195–3208.

114. Gao, P. F.; Jia, H. P.; Yang, J., et al., Three-Dimensional Porous Silicon-MWNT Heterostructure with Superior Lithium Storage Performance. *Phys. Chem. Chem. Phys.* **2011,** *13*, 20108-20111.

115. Xiao, J.; Xu, W.; Wang, D. Y., et al., Stabilization of Silicon Anode for Li-Ion Batteries. *J. Electrochem. Soc.* **2010,** *157*, A1047-A1051.

116. Dorvee, J. R.; Sailor, M. J.; Miskelly, G. M., Digital Microfluidics and Delivery of Molecular Payloads with Magnetic Porous Silicon Chaperones. *Dalton Trans.* **2008**, 721 - 730.

117. Sailor, M. J.; Link, J. R., Smart Dust: nanostructured devices in a grain of sand. *Chem. Commun.* **2005**, 1375-1383.

118. Shriver, D. F.; Drezdzon, M. A., *The Manipulation of Air-Sensitive Compounds*. 2nd ed.; John Wiley and Sons, Inc.: New York, 1986; p 7-44.

119. Segal, E.; Perelman, L. A.; Cunin, F., et al., Confinement of Thermoresponsive Hydrogels in Nanostructured Porous Silicon Dioxide Templates. *Adv. Funct. Mater.* **2007,** *17*, 1153–1162.

120. Lide, D. R., *CRC Handbook of Chemistry and Physics*. 79th ed.; CRC Press: 1998.

121. Simons, J. H., The Solubility of Hydrogen Fluoride in Benzene and in Octane. *J. Am. Chem. Soc.* **1931,** *53*, 83-87.

122. Mischki, T. K.; Donkers, R. L.; Eves, B. J., et al., Reaction of Alkenes with Hydrogen-Terminated and Photooxidized Silicon Surfaces. A Comparison of Thermal and Photochemical Processes. *Langmuir* **2006,** *22*, 8359-8365.

123. Israelachvili, J. N., *Intermolecular and Surface Forces*. 3rd ed.; Academic Press: 2011.

124. Worsfold, O.; Voelcker, N. H.; Nishiya, T., Biosensing Using Lipid Bilayers Suspended on Porous Silicon. *Langmuir* **2006,** *22*, 7078-7083.

125. Weiskopf, D.; Schmitt, E. K.; Kluhr, M. H., et al., Micro-BLMs on Highly Ordered Porous Silicon Substrates: Rupture Process and Lateral Mobility. *Langmuir* **2007,** *23*, 9134-9139.

126. Pace, S.; Gonzalez, P.; Devoisselle, J. M., et al., Grafting of Monoglyceride Molecules for the Design of Hydrophilic and Stable Porous Silicon Surfaces. *New J. Chem.* **2010,** *34*, 29-33.

127. Cunin, F.; Milhiet, P.-E.; Anglin, E., et al., Continuous Planar Phospholipid Bilayer Supported on Porous Silicon Thin Film Reflector. *Ultramicroscopy* **2007,** *107*, 1048-1052.

128. Pace, S.; Seantier, B.; Belamie, E., et al., Characterization of Phospholipid Bilayer Formation on a Thin Film of Porous SiO2 by Reflective Interferometric Fourier Transform Spectroscopy (RIFTS). *Langmuir* **2012,** *28*, 6960-6969.

129. Canham, L. T., Bioactive Silicon Structure Fabrication Through Nanoetching Techniques. *Adv. Mater. (Weinheim, Ger.)* **1995,** *7*, 1033-1037.

130. Tanaka, T.; Mangala, L. S.; Vivas-Mejia, P. E., et al., Sustained Small Interfering RNA Delivery by Mesoporous Silicon Particles. *Cancer Res.* **2010,** *70*, 3687-3696.

131. Küchler, S.; Abdel-Mottaleb, M.; Lamprecht, A., et al., Influence of Nanocarrier Type and Size on Skin Delivery of Hydrophilic Agents. *Int. J. Pharm. (Amsterdam, Neth.)* **2009,** *377*, 169-172.

132. Heinrich, J. L.; Curtis, C. L.; Credo, G. M., et al., Luminescent Colloidal Si Suspensions from Porous Si. *Science (Washington, DC, U. S.)* **1992,** *255*, 66-68.

133. Park, J.-H.; Gu, L.; Maltzahn, G. v., et al., Biodegradable Luminescent Porous Silicon Nanoparticles for in vivo Applications. *Nat. Mater.* **2009,** *8*, 331-336.

134. Tao, Z. M.; Toms, B.; Goodisman, J., et al., Mesoporous Silica Microparticles Enhance the Cytotoxicity of Anticancer Platinum Drugs. *ACS Nano* **2010,** *4*, 789-794.

135. Bimbo, L. M.; Sarparanta, M.; Santos, H. A., et al., Biocompatibility of Thermally Hydrocarbonized Porous Silicon Nanoparticles and their Biodistribution in Rats. *ACS Nano* **2010,** *4*, 3023–3032.

136. Salonen, J.; Laitinen, L.; Kaukonen, A. M., et al., Mesoporous Silicon Microparticles for Oral Drug Delivery: Loading and Release of Five Model Drugs. *J. Control. Release* **2005,** *108*, 362-374.

137. Foraker, A. B.; Walczak, R. J.; Cohen, M. H., et al., Microfabricated Porous Silicon Particles Enhance Paracellular Delivery of Insulin Across Intestinal Caco-2 Cell Monolayers. *Pharm. Res.* **2003,** *20*, 110-116.

138. Serda, R. E.; Mack, A.; Pulikkathara, M., et al., Cellular Association and Assembly of a Multistage Delivery System. *Small* **2010,** *6*, 1329-1340.

139. Wang, H.; Wick, R. L.; Xing, B., Toxicity of Nanoparticles and Bulk ZnO, Al2O3 and TiO2 to the Nematode Caenorhabditis Elegans. *Environ. Pollut. (Oxford, U.K.)* **2009,** *157*, 1171-1177.

140. Mohan, N.; Chen, C.-S.; Hsieh, H.-H., et al., In Vivo Imaging and Toxicity Assessments of Fluorescent Nanodiamonds in Caenorhabditis Elegans. *Nano Lett.* **2010,** *10*, 3692-3699.

141. Pluskota, A.; Horzowski, E.; Bossinger, O., et al., In Caenorhabditis elegans Nanoparticle-Bio-Interactions Become Transparent: Silica-Nanoparticles Induce Reproductive Senescence. *PLoS ONE* **2009,** *4*, e6622.

142. Perelman, L. A.; Pacholski, C.; Li, Y. Y., et al., pH-Triggered Release of Vancomycin from Protein-Capped Porous Silicon Films. *Nanomedicine* **2008,** *3*, 31-43.

143. Wu, E. C.; Park, J.-H.; Park, J., et al., Oxidation-triggered Release of Fluorescent Molecules or Drugs from Mesoporous Si Microparticles. *ACS Nano* **2008,** *2*, 2401-2409.

144. Orosco, M. M.; Pacholski, C.; Sailor, M. J., Real-time monitoring of enzyme activity in a mesoporous silicon double layer. *Nature Nanotech.* **2009,** *4*, 255 - 258.

145. Ruoslahti, E.; Bhatia, S. N.; Sailor, M. J., Targeting of Drugs and Nanoparticles to Tumors. *J. Cell Biol.* **2010,** *188*, 759-768.

146. Canham, L. T., Bioactive Silicon Structure Fabrication Through Nanoetching Techniques. *Adv. Mater.* **1995,** *7*, 1033-1037.

147. Anderson, S. H. C.; Elliott, H.; Wallis, D. J., et al., Dissolution of Different Forms of Partially Porous Silicon Wafers under Simulated Physiological Conditions. *Phys. Status Solidi A-Appl. Res.* **2003,** *197*, 331-335.

148. Low, S. P.; Voelcker, N. H.; Canham, L. T., et al., The Biocompatibility of Porous Silicon in Tissues of the Eye. *Biomaterials* **2009,** *30*, 2873-2880.

149. Canham, L. T.; Stewart, M. P.; Buriak, J. M., et al., Derivatized Porous Silicon Mirrors: Implantable Optical Components with Slow Resorbability. *Phys. Status Solidi A-Appl. Res.* **2000,** *182*, 521-5.

150. Canham, L. T. In *Porous silicon as a therapeutic biomaterial*, Microtechnologies in Medicine and Biology, 1st Annual International, 2000.

151. Salonen, J.; Kaukonen, A. M.; Hirvonen, J., et al., Mesoporous Silicon in Drug Delivery Applications. *J. Pharm. Sci.* **2008,** *97*, 632-653.

152. Bimbo, L. M.; Mäkilä, E.; Laaksonen, T., et al., Drug Permeation Across Intestinal Epithelial Cells using Porous Silicon. *Biomaterials* **2011,** *32*, 2625-2633.

153. Foraker, A.; Walczak, R.; Cohen, M., et al., Microfabricated Porous Silicon Particles Enhance Paracellular Delivery of Insulin Across Intestinal Caco-2 Cell Monolayers. *Pharm Res* **2003,** *20* (1), 110-116.

154. Bimbo, L. M.; Sarparanta, M.; Santos, H. A., et al., Biocompatibility of Thermally Hydrocarbonized Porous Silicon Nanoparticles and their Biodistribution in Rats. *ACS Nano* **2010,** *4*, 3023-3032.

155. Low, S. P.; Williams, K. A.; Canham, L. T., et al., Generation of reactive oxygen species from porous silicon microparticles in cell culture medium. *J. Biomed. Mater. Res., Part A* **2010,** *93A*, 1124-1131.

156. Whalon, M. E.; Wingerd, B. A., Bt: Mode of action and use. *Archives of Insect Biochemistry and Physiology* **2003,** *54* (4), 200-211.

157. Schnepf, E.; Crickmore, N.; Van Rie, J., et al., Bacillus thuringiensis and Its Pesticidal Crystal Proteins. *Microbiol. Mol. Biol. Rev.* **1998,** *62*, 775-806.

158. de Maagd, R. A.; Bravo, A.; Crickmore, N., How Bacillus thuringiensis Has Evolved Specific Toxins to Colonize The Insect World. *Trends Genet.* **2001,** *17*, 193-199.

159. Wei, J.-Z.; Hale, K.; Carta, L., et al., Bacillus thuringiensis Crystal Proteins That Target Nematodes. *Proc. Natl. Acad. Sci. U.S.A.* **2003,** *100*, 2760-2765.

160. Hu, Y.; Georghiou, S. B.; Kelleher, A. J., et al., Bacillus thuringiensis Cry5B Protein Is Highly Efficacious as a Single-Dose Therapy against an Intestinal Roundworm Infection in Mice. *PLoS Neglected Trop. Dis.* **2010,** *4*, e614.

161. Urban, J. F., Jr.; Hu, Y.; Miller, M. M., et al., Bacillus thuringiensis-derived Cry5B Has Potent Anthelmintic Activity against Ascaris suum. *PLoS Neglected Trop. Dis.* **2013,** *7*, e2263.

162. Cappello, M.; Bungiro, R. D.; Harrison, L. M., et al., A Purified Bacillus thuringiensis Crystal Protein with Therapeutic Activity Against the Hookworm Parasite Ancylostoma ceylanicum. *Proc. Natl. Acad. Sci. U.S.A.* **2006,** *103*, 15154-15159.

163. Hu, Y.; Zhan, B.; Keegan, B., et al., Mechanistic and Single-Dose In Vivo Therapeutic Studies of Cry5B Anthelmintic Action against Hookworms. *PLoS Neglected Trop. Dis.* **2012,** *6*, e1900.

164. Donkin, S.; Dusenbery, D., A Soil Toxicity Test using the Nematode Caenorhabditis Elegans and An Effective Method of Recovery. *Arch. Environ. Contam. Toxicol.* **1993,** *25*, 145-151.

165. van Kessel, W. H. M.; Brocades Zaalberg, R. W.; Seinen, W., Testing Environmental Pollutants on Soil Organisms: A Simple Assay to Investigate The Toxicity of Environmental Pollutants on Soil Organisms, using CdCl2 and Nematodes *Ecotoxicol. Environ. Saf.* **1989,** *18*, 181-190.

166. Holden-Dye, L.; Walker, R. J., Anthelmintic Drugs (November 02, 2007). WormBook, Ed. The C. elegans Research Community.

167. Bungiro, R. D.; Greene, J.; Kruglov, E., et al., Mitigation of Hookworm Disease by Immunization with Soluble Extracts of Ancylostoma ceylanicum. *J. Infect. Dis.* **2001,** *183*, 1380-1387.

168. Hu, Y.; Xiao, S.-H.; Aroian, R. V., The New Anthelmintic Tribendimidine is an L-type (Levamisole and Pyrantel) Nicotinic Acetylcholine Receptor Agonist. *PLoS Negl Trop Dis* **2009,** *3*, e499.

169. Meade, S. O.; Chen, M. Y.; Sailor, M. J., et al., Multiplexed DNA Detection Using Spectrally Encoded Porous SiO2 Photonic Crystal Particles. *Anal. Chem. (Washington, DC, U.S.)* **2009,** *81*, 2618-2625.

170. Hu, Y.; Xiao, S.-H.; Aroian, R. V., The New Anthelmintic Tribendimidine is an L-type (Levamisole and Pyrantel) Nicotinic Acetylcholine Receptor Agonist. *PLoS Neglected Trop. Dis.* **2009,** *3*, e499.

171. Hu, Y.; Platzer, E. G.; Bellier, A., et al., Discovery of a Highly Synergistic Anthelmintic Combination That Shows Mutual Hypersusceptibility. *Proc. Natl. Acad. Sci. U.S.A.* **2010,** *107*, 5955-5960.

172. Hu, Y.; Ellis, B. L.; Yiu, Y. Y., et al., An Extensive Comparison of the Effect of Anthelmintic Classes on Diverse Nematodes. *PLoS ONE* **2013,** *8*, e70702.

173. Hu, Y.; Miller, M. M.; Derman, A. I., et al., A Bacillus Subtilis Strain Engineered for Treatment of Soil-transmitted Helminth Diseases. *Appl. Environ. Microbiol.* **2013**.

174. Wu, E. C.; Andrew, J. S.; Buyanin, A., et al., Suitability of Porous Silicon Microparticles for the Long-term Delivery of Redox-active Therapeutics. *Chem. Commun.* **2011,** *47*, 5699-5701.

175. Andrew, J. S.; Anglin, E. J.; Wu, E. C., et al., Sustained Release of a Monoclonal Antibody from Electrochemically Prepared Mesoporous Silicon Oxide. *Adv. Funct. Mater.* **2010,** *20*, 4168-4174.

176. Clokey, G. V.; Jacobson, L. A., The Autofluorescent "Lipofuscin Granules" in the Intestinal Cells of Caenorhabditis elegans are Secondary Lysosomes. *Mech. Ageing Dev.* **1986,** *35*, 79-94.

177. Griffitts, J. S.; Haslam, S. M.; Yang, T., et al., Glycolipids as Receptors for Bacillus thuringiensis Crystal Toxin. *Science* **2005,** *307*, 922-925.

178. Weitschies, W.; Kosch, O.; Mönnikes, H., et al., Magnetic Marker Monitoring: An Application of Biomagnetic Measurement Instrumentation and Principles for the Determination of the Gastrointestinal Behavior of Magnetically Marked Solid Dosage Forms. *Adv. Drug Delivery Rev.* **2005,** *57*, 1210-1222.

179. Ponchel, G.; Irache, J.-M., Specific and Non-specific Bioadhesive Particulate Systems for Oral Delivery to the Gastrointestinal Tract. *Adv. Drug Delivery Rev.* **1998,** *34*, 191-219.

180. Baeumner, A., Biosensors for Environmental Pollutants and Food Contaminants. *Anal. Bioanal. Chem.* **2003,** *377*, 434-445.

181. Song, J. H.; Sailor, M. J., Chemical Modification of Crystalline Porous Silicon. *Comments on Inorganic Chemistry* **1999,** *21*, 69-84.

182. Schwartz, M. P.; Derfus, A. M.; Alvarez, S. D., et al., The Smart Petri Dish: A Nanostructured Photonic Crystal for Real-Time Monitoring of Living Cells. *Langmuir* **2006,** *22*, 7084-7090.

183. An, Y. H.; Stuart, G. W.; McDowell, S. J., et al., Prevention of Bacterial Adherence to Implant Surfaces with a Crosslinked Albumin Coating in Vitro. *J. Orthop. Res.* **1996,** *14*, 846-849.

184. Hermanson, G. T., *Bioconjugate Techniques*. Academic Press, Inc.: San Diego, 1996; p 785.

185. Rang, C.; Galen, J. E.; Kaper, J. B., et al., Fitness Cost of the Green Fluorescent Protein in Gastrointestinal Bacteria. *Can. J. Microbiol.* **2003,** *49*, 531-537.

186. Sperandio, V.; Mellies, J. L.; Nguyen, W., et al., Quorum Sensing Controls Expression of the Type III Secretion Gene Transcription and Protein Secretion in Enterohemorrhagic and Enteropathogenic Escherichia coli. *Proc. Natl. Acad. Sci. U. S. A.* **1999,** *96*, 15196-15201.

187. Levine, M. M.; Kaper, J. B.; Herrington, D., et al., Volunteer Studies of Deletion Mutants of Vibrio cholerae O1 Prepared by Recombinant Techniques. *Infect Immun* **1988,** *56*, 161-167.

188. Harris, L. G.; Richards, R. G., Staphylococci and Implant Surfaces: A Review. *Injury* **2006,** *37* (2, Supplement), S3-S14.

189. Su, T. J.; Lu; Thomas, R. K., et al., The Conformational Structure of Bovine Serum Albumin Layers Adsorbed at the Silica–Water Interface. *J. Phys. Chem. B* **1998,** *102*, 8100-8108.

190. Kaplan, D.; Nir, I.; Shmueli, L., Effects of High Relative Humidity on the Dynamic Adsorption of Dimethyl Methylphosphonate (DMMP) on Activated Carbon. *Carbon* **2006,** *44*, 3247-3254.

191. Krasteva, N.; Guse, B.; Besnard, I., et al., Gold Nanoparticle/PPI-dendrimer Based Chemiresistors: Vapor-sensing Properties as a Function of the Dendrimer Size. *Sens. Actuators, B* **2003,** *92*, 137-143.

192. Wohltjen, H.; Snow, A. W., Colloidal Metal–Insulator–Metal Ensemble Chemiresistor Sensor. *Anal. Chem.* **1998,** *70*, 2856-2859.

193. Byoungho, L., Review of the Present Status of Optical Fiber Sensors. *Opt. Fiber Technol.* **2003,** *9*, 57-79.

194. Barnard, S. M.; Walt, D. R., Fiber-optic Organic Vapor Sensor. *Environ. Sci. Technol.* **1991,** *25*, 1301-1304.

195. King, B. H.; Ruminski, A. M.; Snyder, J. L., et al., Optical-Fiber-Mounted Porous Silicon Photonic Crystals for Sensing Organic Vapor Breakthrough in Activated Carbon. *Adv. Mater.* **2007,** *19*, 4530-4534.

196. Caron, S.; Bernard, P.; Vernon, M., et al., Porous Glass Optical Fiber Sensor As An End-of-service Indicator for Respiratory Cartridges. *Sens. Actuators, B* **2004,** *102*, 198-206.

197. Zangooie, S.; Jansson, R.; Arwin, H., Ellipsometric Characterization of Anisotropic Porous Silicon Fabry-Perot Filters and Investigation of Temperature Effects on Capillary Condensation Efficiency. *J. Appl. Phys.* **1999,** *86*, 850-8.

198. Ruminski, A. M.; King, B. H.; Salonen, J., et al., Porous Silicon-Based Optical Microsensors for Volatile Organic Analytes: Effect of Surface Chemistry on Stability and Specificity. *Adv. Funct. Mater* **2010,** *20*, 2874-2883.

199. Kelly, T. L.; Gao, T.; Sailor, M. J., Carbon and Carbon/Silicon Composites Templated in Rugate Filters for the Adsorption and Detection of Organic Vapors. *Adv. Mater.* **2011,** *23*, 1776-1781.

200. Rudisill, E. N.; Hacskaylo, J. J.; LeVan, M. D., Coadsorption of Hydrocarbons and Water on BPL Activated Carbon. *Ind. Eng. Chem. Res.* **1992,** *31*, 1122-1130.

201. *NIOSH Pocket Guide to Chemical Hazards*. National Institute of Occupational Safety and Health of the United States, Publication #2005-149: 2005.

202. Linders, M. J. G.; van den Broeke, L. J. P.; Kapteijn, F., et al., Binary Adsorption Equilibrium of Organics and Water on Activated Carbon. *AIChE J.* **2001,** *47*, 1885-1892.